# HYDROXYL TAGGING VELOCIMETRY IN A SUPERSONIC FLOW OVER A RAMPED-WALL CAVITY FLAMEHOLDER WITH AN UPSTREAM STRUT

**BY**
**NATHAN RYAN GRADY**

MECHANICAL ENGINEERING

# HYDROXYL TAGGING VELOCIMETRY IN A SUPERSONIC FLOW OVER A RAMPED-WALL CAVITY FLAMEHOLDER WITH AN UPSTREAM STRUT

NATHAN RYAN GRADY

Thesis under the direction of Professor Robert W. Pitz

Supersonic air flow over a wall cavity with a rear ramp both with and without an upstream strut was studied with Hydroxyl Tagging Velocimetry (HTV). HTV is a non-intrusive means of measuring gas velocity by producing a hydroxyl tag from water vapor via a two step process: 1) the "write" phase where water molecules are dissociated into OH+H, 2) the "read" phase where after a fixed time delay the OH field is interrogated with planar laser-induced fluorescence. An 11x11 OH grid was used to obtain velocities at ~120 grid points. Mean and RMS fluctuation velocity profiles both with and without the strut were analyzed and compared to each other and to a rectangular cavity studied by other authors. In the ramped-cavity, increased recirculation and turbulence was observed over the ramp compared to the rectangular cavity, and the shear layer both grew slower and was lower into the cavity. Once the strut was installed, it was observed that cavity recirculation along the centerline increased relative to the no-strut configuration and extended above the step. Furthermore, expansion waves off the top of the strut and weak compression waves off the back of the strut were observed.

To best analyze vorticity, two separate interpolation schemes were interrogated by comparing velocity, and vorticity data. In general, the two methods provided similar results for irrotational flows. However for rotational flows, it was found that a Powell-Sabin

interpolation more accurately determined the location of velocity gradients compared to a cubic interpolation scheme.

# HYDROXYL TAGGING VELOCIMETRY IN A SUPERSONIC FLOW OVER A RAMPED-WALL CAVITY FLAMEHOLDER WITH AN UPSTREAM STRUT

By

Nathan Ryan Grady

Thesis

Submitted to the Faculty of the

Graduate School of Vanderbilt University

in partial fulfillment of the requirements

for the degree of

MASTER OF SCIENCE

in

Mechanical Engineering

December, 2010

Nashville, Tennessee

Approved:

Dr. Robert W. Pitz

Dr. Joseph A Wehrmeyer

Dr. Amrutur V. Anilkumar

## ACKNOWLEDGEMENTS

First, I would like to thank Dr. Pitz of Vanderbilt University and Dr. Campbell Carter of Wright Patterson Air Force Base Research Labs for their guidance and patience during the last two and half years. I would also like to thank Troy Friedlander for his time and effort spent helping me conduct these experiments at Wright Patterson Air Force Base as well as Dr. Mark Hsu and technicians Bill Terry and David Schommer for all of their assistance and camaraderie during this effort. Finally, I would like to thank Marc Ramsey for his development of the reduction software used, and all of his help answering questions regardless of their pertinence to the current task.

Financial support was granted through the summer fellowship research program at Wright-Patterson Air Force Base under the Air Force contractor, Universal Technologies Corporation. Additional financial support was provided by the Air Force Office of Scientific Research, Combustion and Diagnostics Program (Julian Tishkoff, Manager) under contract FA9550-09-1-0205.

A special acknowledgement goes to my family for supporting and encouraging me over the years. Thanks for always believing in me, Mom, Dad, Michael, and Meagan as well as my girlfriend Kelly.

**TABLE OF CONTENTS**

Page

**LIST OF TABLES**

**LIST OF FIGURES**

# Chapter I

# INTRODUCTION

## 1.1 Motivation and Goals

The mechanical compression used in turbine engines provides effective and self-sufficient thrust for vehicles up to and including the supersonic flight regime. However, at higher Mach numbers this mechanical process becomes inefficient. Therefore, the use of a ramjet engine where a shock at the inlet of the engine compresses and decelerates the flow to subsonic conditions for combustion is preferable. If even faster flight speeds (M>5) are desired for either space access or faster response time for hostile targets, then the process of slowing the air to subsonic speeds for combustion results in unacceptable increases in temperature and pressure which may have an adverse effect on engine efficiency and on the structural integrity of the engine. Additionally, there may be an unacceptable loss of stagnation pressure due to the inlet shock. Therefore, the use of supersonic combustion in a ramjet can be used to provide thrust in the hypersonic regime.

The problems with supersonic combustion ramjets (scramjets) are: 1) the relatively low residence time in the engine, and 2) lack of fuel/flame penetration into the freestream of the engine. The former could be solved by simply designing a long engine section; however, this would result in an unacceptably large aircraft. Since the flow through the engine is supersonic, wall injection of fuel creates bow shocks which increase drag and reduce fuel penetration necessary for effective use of combustor volume. In order for scramjets to be a viable vehicle, both of these issues need to be adequately addressed.

The use of a cavity flame holder (to increase residence time) paired with a strut (to provide fuel penetration) was considered in this study in an unreacting Mach 2 flow at

Research Cell 19 of Wright Patterson Air Force Base in Dayton, OH. Hydroxyl Tagging Velocimetry (HTV) was used to acquire velocity profiles at various locations in the scramjet combustor test section. HTV is a non-intrusive means of measuring gas velocity by producing a hydroxyl tag from water vapor via a two step process: 1) the "write" phase where water molecules are dissociated into OH+H by an 193 nm ArF excimer laser, 2) the "read" phase where after a fixed time delay the OH field is interrogated with planar laser-induced fluorescence (LIF). An 11x11 OH grid was used to obtain velocities at ~120 grid points. Mean and RMS fluctuation velocity profiles both with and without the strut were analyzed and compared to each other and to a rectangular cavity studied by other authors. Analysis of the phenomenological effect of the cavity and strut is presented here.

## 1.2 Organization

To assist the reader, the outline of the thesis will be detailed in this section. A background in the development and implementation of cavities and struts in scramjet combustors as well as a brief rationale for the use of HTV is discussed in Chapter II. The experimental set-up and overview of previous HTV experiments are detailed in Chapter III. Chapter IV discusses the data and current analysis of this particular work. Finally, Chapter V will summarize the thesis.

# Chapter II

# BACKGROUND

## 2.1 Development of Devices Used to Promote Effective Scramjet Combustion

The earliest known published paper on the use of wall cavities as a flameholder was by Huellmantel et al. [1] in 1957. To quickly summarize his findings, he found that cavities with a length-to-depth (L/D) ratio between 2 and 4 provided the best flame holding, and in general all such cavities had significantly less static pressure drop as compared to a bluff body flameholder.

Cavity flows are described as being either "open" or "closed" as seen in Figure 2-1. A cavity is considered "open" if the shear layer impinges on the rear wall of the cavity, and "closed" if the shear layer reattaches to the floor of the cavity. Closed cavities result in a negative pressure coefficient on the leading edge and a high pressure coefficient on the trailing edge (See CP curves in Figure 2-1). Both of these pressures result in a large overall pressure drag [2]. Whereas open cavities have a positive pressure coefficient on the edges, creating substantially less pressure drag than a closed cavity; therefore, open cavities are preferred. The transition point from open to closed is around L/D>10.

Various researchers [2, 3] analyzed the length-to-depth ratio (L/D) of cavities and the effect this had on pressure fluctuations. Rossiter [3] characterized these fluctuations parametrically, and found that there were both random and periodic pressure fluctuations, with random pressure fluctuations being dominant at an L/D>6 and periodic pressure fluctuations becoming dominant at L/D<4. Since random fluctuations are undesirable from a controls stand point, L/D<4 cavities are preferable. Furthermore, these pressure fluctuations oscillate transversely for an L/D<2 which result in less flame stability,

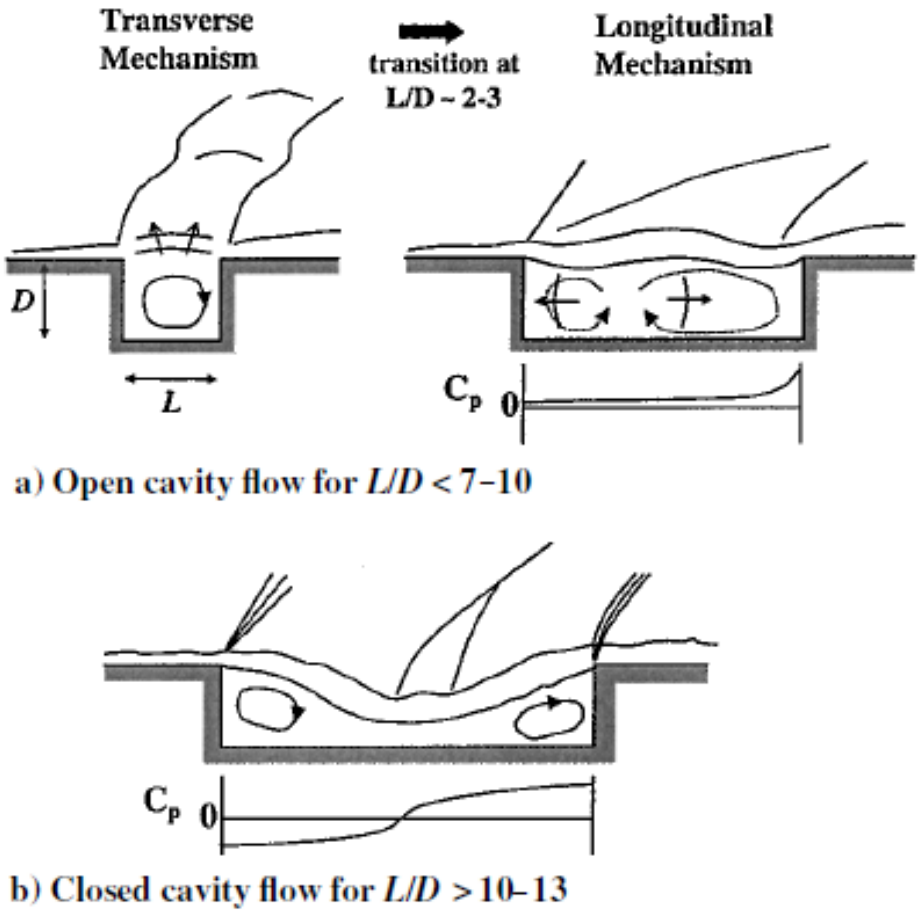


**Figure 2-1: Diagram of cavity flows demonstrating the differences between open and closed cavities from Ben Yakar and Hanson [2]. For b), the shear layer reattaches where the $C_p$ value goes from negative to positive.**

and create bow shocks [2]. As a result of these factors, design of cavity flameholders is best restricted to an L/D greater than 2 and less than 4 as seen by Huellmantel et al. [1].

In order to promote steady combustion, suppression of the periodic pressure fluctuations described above is also desirable. As proposed by Ben-Yakar and Hanson [2], these pressure fluctuations are caused when the shear layer impinges on the rear wall which results in mass entrainment into the cavity. This then creates an acoustic wave which is reflected back and forth across the cavity. It was found that angling the back wall of the cavity removes the means by which the aforementioned acoustic wave reflects back into the cavity and instead deflects it into the main flow. This angling results in a steady shear layer impingent, and in turn more mass entrainment. Schlieren images comparing the flow over rectangular and a ramped cavity taken by Ben-Yakar and Hanson [2] are shown in Figure 2-2. It can be noted from Figure 2-2, that shear layer over the rectangular cavity grows into the main flow of the cavity acting like a compression corner, but the shear layer over the ramped-cavity curls into the cavity acting like an expansion corner. This results in a shock wave over the step in the rectangular cavity, and an expansion wave in the ramped cavity.

This ability to vastly improve flame stability without a corresponding increase in drag is a great asset in obtaining viable scramjet flight. However, cavities do not adequately address the issue of fuel/flame penetration into the freestream. In fact, the products of the cavity flameholder tend to remain towards the floor of the combustor, and not penetrate into the freestream as desired to effectively utilize the entire volume of the scramjet engine [4].The following section will describe how the addition of a strut can increase fuel penetration.

Struts have been studied as a method of increasing fuel/flame penetration into the main air flow, and to help stabilize and augment the effect of a cavity flameholder[5-7], and have also been useful in aiding mixing due to the counter-rotating vortices they produce [4].

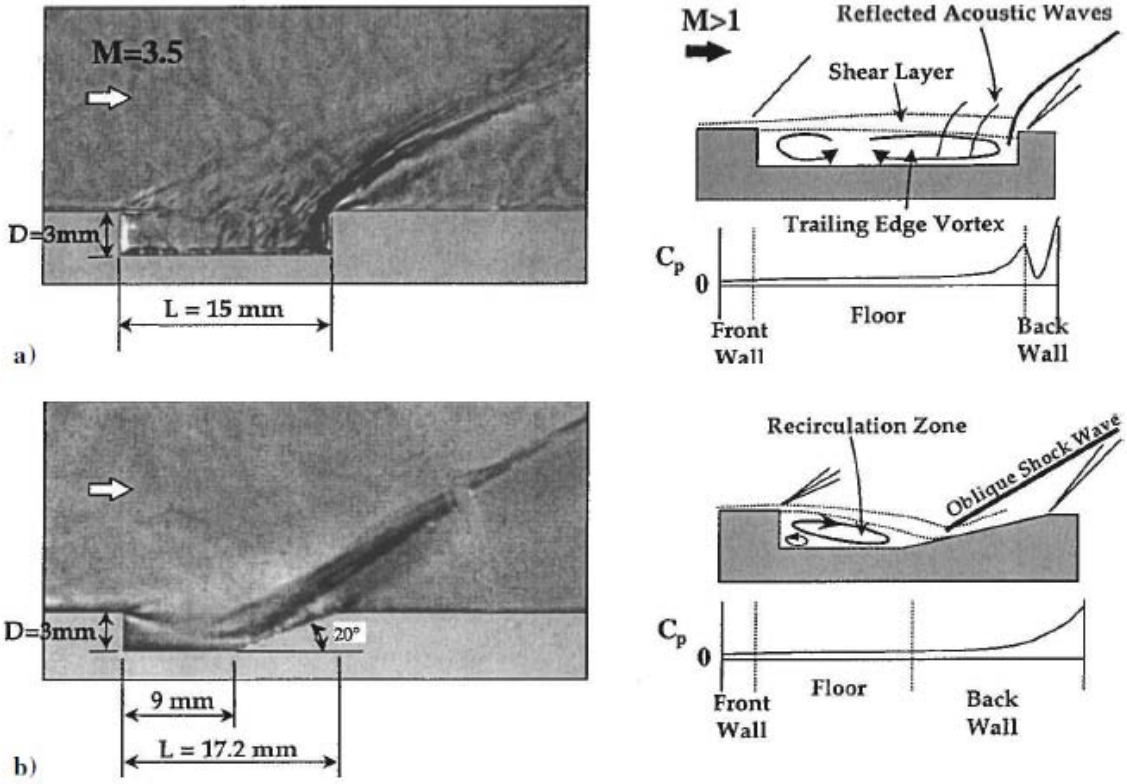


**Figure 2-2: Schlieren image taken by Ben-Yakar and Hanson [2] comparing the flow patterns of a rectangular and a ramped cavity.**

Since struts are exposed to the main flow of the scramjet, they are subjected to high temperatures and pressures and greatly increase the drag of the engine. Furthermore, they are permanent features which cannot be adjusted as flight conditions change. However, alternative means of providing fuel penetration have proved either ineffective or unreliable across a wide range of flight speeds/conditions. Therefore, interest in struts reappeared in the literature during the 1990's.

There are two common uses of strut-aided-combustion in the literature: 1) a strut upstream of a fuel injector, and 2) direct strut injection. Direct strut injection provides fuel penetration into the freestream by virtue of the fact that it is injected into the freestream. Struts upstream of a wall injector also supply fuel penetration, but in a slightly different manner. Expansion waves form along the back face of the strut thus creating a low pressure region while the combustion near the wall injector creates a high pressure region. Therefore, the low pressure region behind the strut entrains the reacting region upwards from the cavity into the main air flow. The latter effect is especially useful when it is combined with a cavity flameholder, since it provides a reliable conveyance of the hot cavity gas into the freestream. This work was primarily concerned with the direct coupling of struts with cavities.

Direct coupling of a strut and a cavity, seen in Figure 2-3, is a recent innovation in the literature [4, 8]. Both of these studies found that the addition of a strut to a cavity enhanced flameholding and mass exchange between the cavity and the main flow. Furthermore, Freeborn et al. [4] also concluded via his CFD predictions that a strut increased mixing and mass exchange by 300%. These increases can be explained via the following: increased recirculation and turbulence along the ramp, increased surface area between the cavity-wake flow and the main flow, and streamwise vortices shed behind the strut.

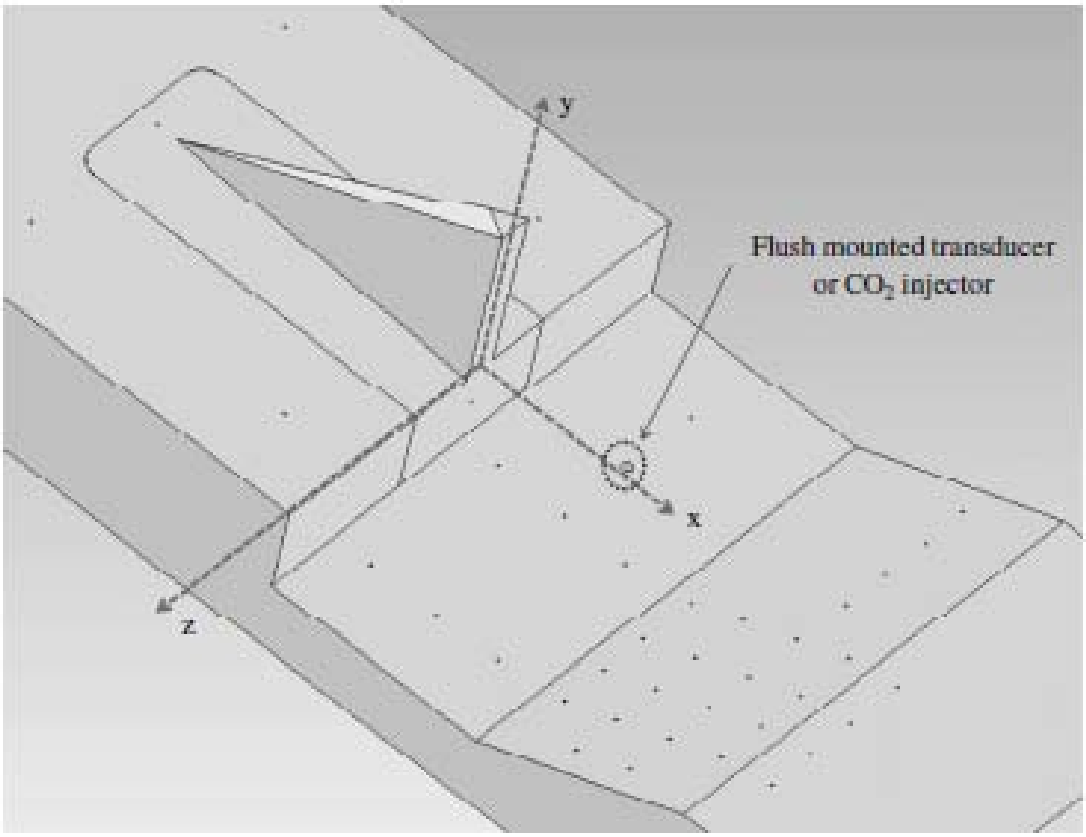


**Figure 2-3: Example of a coupled cavity flameholder and an upstream strut from Freeborn et al. [4].**

While there are plenty of qualitative analyses on the flow patterns in a scramjet coupled with CFD predictions, there are no known quantitative, non-intrusive experimental velocity data obtained in these environments

## 2.2 Velocimetry Techniques

Due to the supersonic nature of a scramjet combustor, the use of physical probes to determine the flowfield is problematic due to the large disturbances they cause. Therefore, a non-intrusive method which can adequately characterize the flow is necessary. Such methods normally consist of laser scattering measurements off of particles which frequently are added to the flow. However, since these particles tend to be significantly larger than the fluid medium they're suspended in, they fail to follow streamlines through large velocity gradients such as shocks thereby causing inconsistencies with their corresponding particle-based techniques [9, 10].

By reducing the size of the particle to the molecular scale the response time of the particle is equivalent to the flow of interest and can therefore follow streamlines. Various molecular techniques have been implemented; however, most are not conducive for accurate measurements in the current work. Doppler-shift measurements typically involve an expensive and/or toxic seed particle making them unfavorable for larger facilities such as Cell 19 [9], or involve Rayleigh scattering which is inherently weak compared to laser scattering off of sidewalls making near-boundary measurements problematic.

Molecular Tagging Velocimetry (MTV) operates by tagging a specified molecule with a laser and making a time-of-flight measurement. The exact method to image the tag movement varies according to the original molecule/tag (in the case of HTV, laser-induced fluorescence (LIF) is used). Many MTV methods need to be seeded with expensive and/or

toxic tags, making them undesirable to use. Other methods use molecules already present in the flow to produce the required tags such as $N_2^+$ ions[11], ozone[12], nitric oxide[13-15], and vibrationally excited oxygen[16]; however, these are non-linear processes and only yield tags close to the laser focus. In order to expand the region which can be scanned with a single laser pulse, a linear method is preferable.

Hydroxyl Tagging Velocimetry (HTV) is used in this study since it is a linear method. An ArF laser at 193 nm photodissociates water in a single-photon process to make an OH tag; all such tags can be imaged via LIF to provide a time-of-flight measurement.

### 2.3 HTV

The $H_2O$ of moist flows such as room air or post combustion region in hydrogen or hydrocarbon flames can be tagged through a single photon photodissociation by creating OH molecules. These OH tags can then by imaged via LIF after a certain known time delay to provide a time-of-flight measurement. This measurement is known as Hydroxyl Tagging Velocimetry (HTV).

A schematic of the HTV process can be found in Figure 2-4. In the first phase, an ArF ~193 nm excimer laser beam is focused into a humid region of interest to photodissociate the water molecules by exciting them into a repulsive $\tilde{A}^1B_1$ state[17] as shown by equation 2-1. This process then "writes" a grid of OH tag lines:

$$H_2O(\tilde{X}A_1)+h\nu_{\lambda=193\ nm} \rightarrow H_2O(\tilde{A}^1B_1) \rightarrow OH(X^2\Pi)+H(^2S) \quad (2\text{-}1)$$

In the "read" phase, a second laser is formed into a sheet at 282 nm from a frequency doubled Nd:YAG-pumped dye laser tuned to the $Q_1(1)$ transition of the $A^2\Sigma^+(v'=1)\leftarrow X^2\Pi$ ($v''=0$) band:

$$OH(X^2\Pi)+h\nu_{\lambda=282\ nm} \rightarrow OH(A^2\Sigma^+) \quad (2\text{-}2)$$

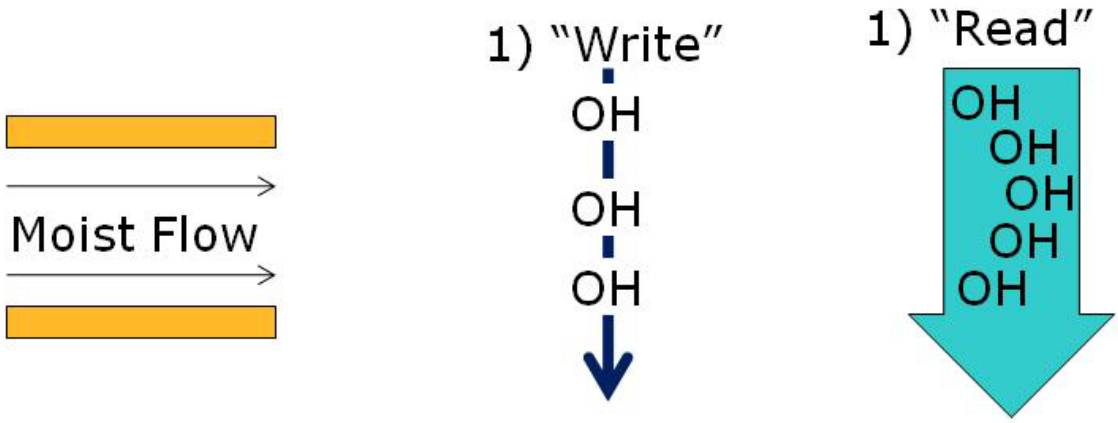


**Figure 2-4. Schematic of Hydroxyl Tagging Velocimetry**

This creates a fluorescence which can then be imaged by a camera. This image can then be compared to the undelayed (i.e. write) image to determine displacement and the time-of-flight velocity.

# Chapter III

# PAST WORK AND FACILITIES

## 3.1 Research Cell 19

The experiment was conducted in the scramjet combustor test section of Research Cell 19 at Wright Patterson Air Force Base in Dayton, OH (schematic shown in Figure 3-1). Cell 19 is a direct-connect facility with an experimental focus on optical diagnostics, and therefore mechanical vibrations of the facility are small and are assumed negligible. The wind tunnel is highly modular with the ability to test multiple test configurations, Mach numbers, inlet total temperature and pressure values, and exit pressure values. The test section (51x152 mm at the inlet) has 3 optical access areas to the sides and on top of the tunnel allowing for flow visualization of all orthogonal planes. A Mach 2 nozzle was used to provide a 2-D uniform flow symmetric along the transverse and span wise centerlines. Air was supplied through a series of compressors and a gas-fired heat exchanger. To provide the aforementioned variations in inlet total temperature and pressure, a hot line (maximum capacity: 8 kg/s of 53 atm air at 922 K) and cold line (maximum capacity: 8 kg/s of 53 atm air at ambient temperature) merged at a mixing station. An insulated expansion loop transports the mixed air to a five-branched supply manifold (two of which exited through the roof) [18]. Flexible steel hoses connected the left and right supply manifolds seen in the left hand side of Figure 3-1 to allow for thermal expansion of the wind tunnel.

The combustion section of the wind tunnel of Cell 19 has five major sections: 1) inlet, 2) settling chamber, 3) nozzle , 4) test section, and 5) diffuser and exit. The inlet conveys the air supply into the settling chamber. To insure an even distribution of air into the settling chamber, a rearward-facing perforated cone was installed in the inlet. The settling chamber

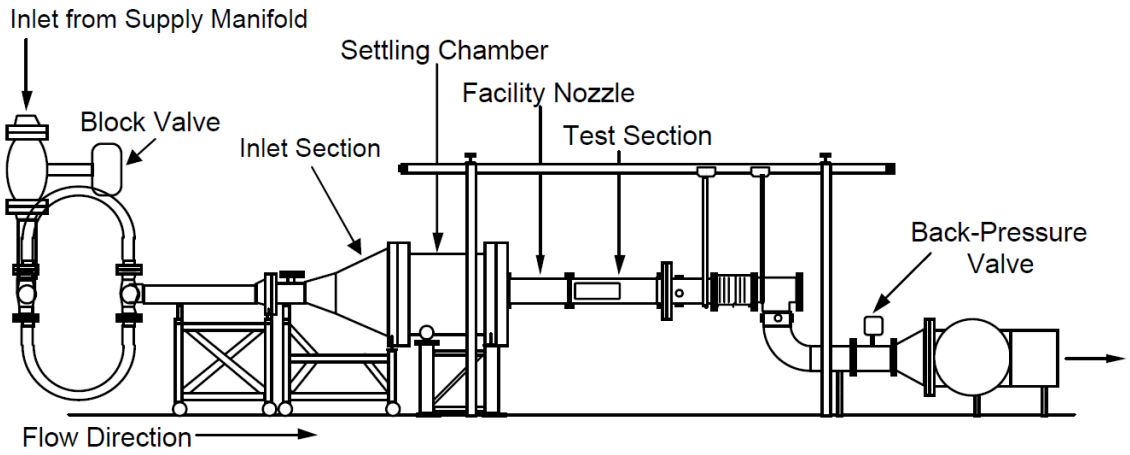


**Figure 3-1: Schematic of Research Cell 19 at Wright Patterson Air Force Base in Dayton, OH [18].**

provides 15 m/s of air (maximum capacity of 25 atm at 900 K at 8 kg/s) and has a mesh of screens and a honeycomb section to condition the flow and increase repeatability from test to test. The settling chamber then flows into the nozzle (Mach 2 for the present experiments), before leading into the test section. Finally, the air exits through a spray-cooled diffuser before being directed out of the building.

The test section used for both the present work and that of Lahr et al. [9] consisted of a constant area 51x153 mm isolator followed by a 2.5°divergence along the bottom wall with a constant width of 153 mm. In the divergent region, a various wall cavities were installed which will be discussed below.

### 3.2 Past HTV Work in a Scramjet Test Section

HTV has been previously applied to a scramjet combustor test section at Wright Patterson Air Force Base by Lahr et al. [9, 10]. Their work will be summarized here to elucidate the advancements of the present work. The laser and optical system used by Lahr [10] was very similar to the present work, and will therefore be described in detail here.

The laser system used is shown schematically in Figure 3-2. A Lambda Physik Compex 150 ArF excimer laser produced the 193 nm “write” beam used to create the hydroxyl tags. The ArF laser beam (20 mm high × 10 mm wide, 100 mJ/pulse, broadband, 1 nm bandwidth) was split by a 50/50 beam splitter with one section being sent under the wind tunnel. This was done to provide optical access from both sides to prevent beam clipping when probing near a wall. Before entering the test section through the windows, each beam path passed through “grid optics”, comprised of a 300 mm focal length (fl) cylindrical lens (25 mm × 40 mm) and a stack of eleven 300 mm fl cylindrical lenslets ( 20 mm wide × 2 mm high)

.

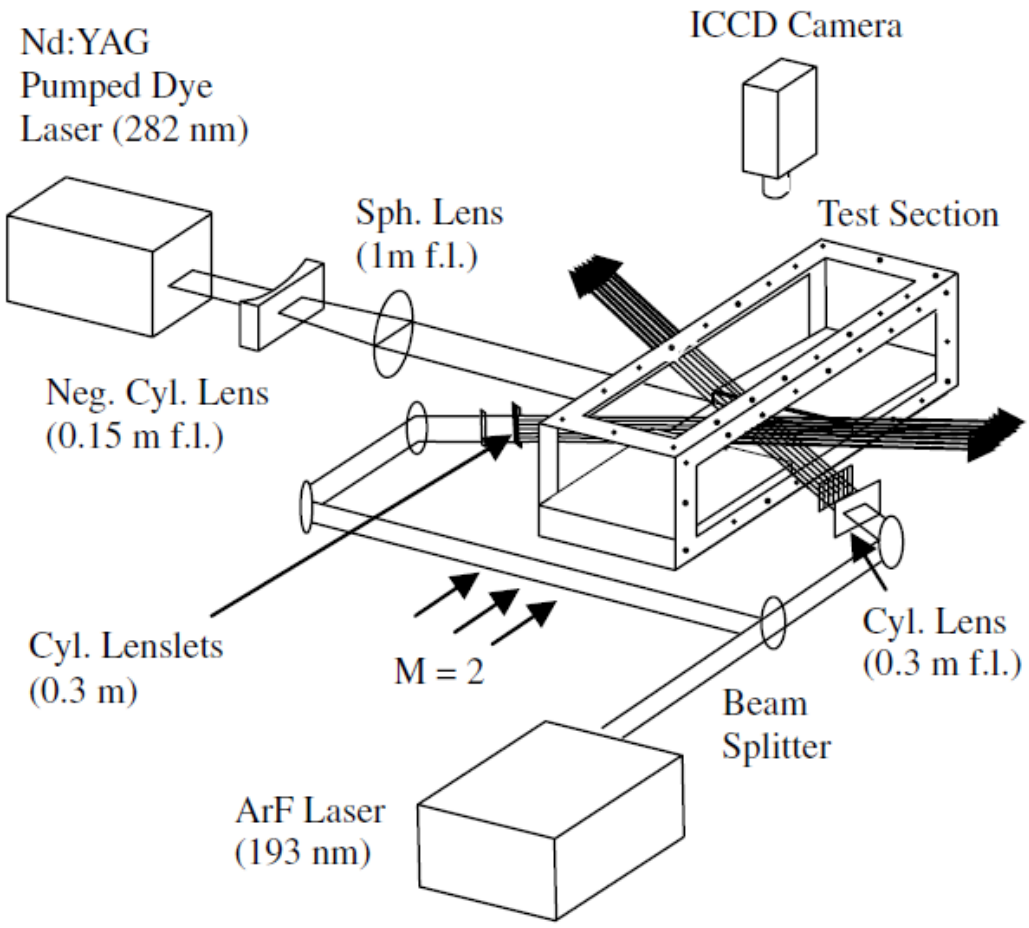


**Figure 3-2: Schematic of HTV laser system used by Lahr [10].**

oriented 90° from each other [10]. A photograph of the grid optics is provided in Figure 3-3. These grid optics formed 11 grid lines each (beam diameter ~0.5mm at measurement zone) for a total of 121 grid intersections. Laser energy for each beam path was 9.4 mJ and 7.4 mJ for the left and right beam paths respectively. The discrepancies between the energy out of the laser and what actually reaches the tunnel is due to absorption of the broadband ArF 193 nm laser by $O_2$. The Lambda Physik Compex 150 ArF can also produce narrowband radiation and be tuned between $O_2$ transitions, to mitigate absorption; however, difficulties with the laser prevented narrowband operation [10].

The position of the 11x11 OH gridlines created by the "write" beam was determined by a "read" process that includes an OH planar laser-induced fluorescence (PLIF) measurement with a 282 nm laser as described in Section 3-1. The "read" beam was created by a Spectra Physics GCR-170 Nd:YAG pumping a Lumonics HD300 Hyperdye dye laser. The dye laser output was then frequency doubled within an Inrad Autotracker III; the 282 nm beam was separated from the dye beam within an Inrad Prism Harmonic Separator. To ensure that the 282 nm beam remained tuned to the aforementioned transition, a small portion of the beam was split off and directed over a small methane-air flame; OH laser-induced fluorescence was detected with a photomultiplier tube (PMT) attached to a 0.1-m monochromator. The 282-nm beam was then directed to a photodiode (PD), so that the 282-nm beam energy could be monitored. Both PMT and PD signals were then displayed on an oscilloscope to be monitored. A Quantum Composer (model 9318E) pulse generator was used to control the timing between the lasers and the cameras. The timing errors were about 20 ns, or about 1% of the 2 μs delay used in the study [10].

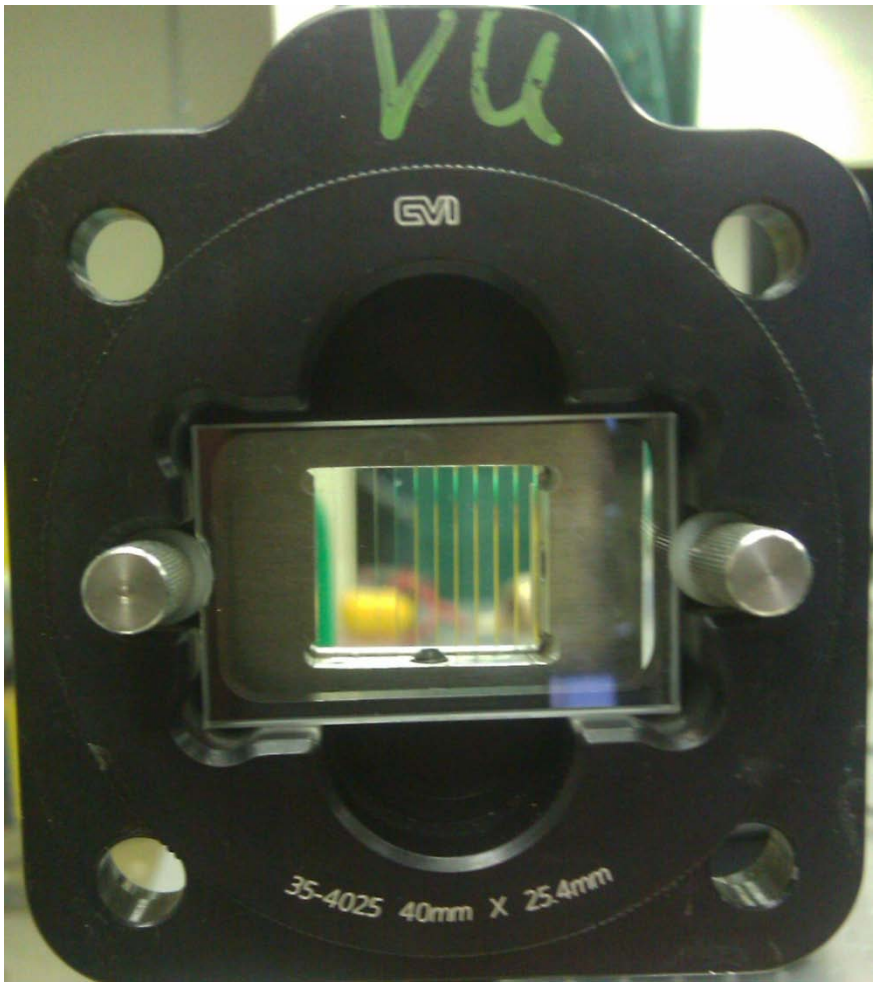


**Figure 3-3: Photograph of grid optics of eleven micro-lenses used to make OH "write" grid.**

The “read” sheet was created by diverging the output 282 nm beam with a -150 mm focal length (fl) cylindrical lens and then focusing it with a 1 m fl spherical lens. This sheet was also retro-reflected back into the tunnel with a delay of 5 ns with the intention of increasing the signal. Both the 282 nm “read” sheet and the 193 nm “write” grid were rotated 2.5° (i.e. the divergence of the test section) to be parallel with the cavity floor.

The “write” and “read” tag locations were imaged by a PIMAX “SuperBlue” intensified CCD camera fitted with a 45-mm f/1.8 UV lens (Cerco). To block the background scattering from tunnel surfaces, Schott glass filters (WG-305 and UG-5) were placed in front of the lens. The CCD consisted of a 512x512 pixel array which was binned 2x2 to increase the maximum repetition rate of the camera to 10 Hz and to increase signal strength. The size of the 2x2 binned pixels was 156 µm x 156 µm. The overall field of view was a 40 mm square with the camera being pointed directly down into the tunnel to view the grids through a Suprasil window [10].

The camera and focusing optics were arranged on a 3-D traversing table. However, since neither of the lasers were on the table, the optics were arranged in such a way that the table could move vertically to probe into and above the cavity (but not in the other two orthogonal directions).

Lahr et al. used an MTV software developed at Michigan State University by Gendrich and Koochesfahani [19] to determine the displacement of the tags. Since this code was not used in the current study, it will not be discussed further.

The cavity used by Lahr was a 17x66 mm rectangular cavity and can be seen in Figure 3-4. Because the tunnel air was dry, water had to be added into the settling chamber to provide a moist flow necessary for HTV. Since the current study did measure the effect of

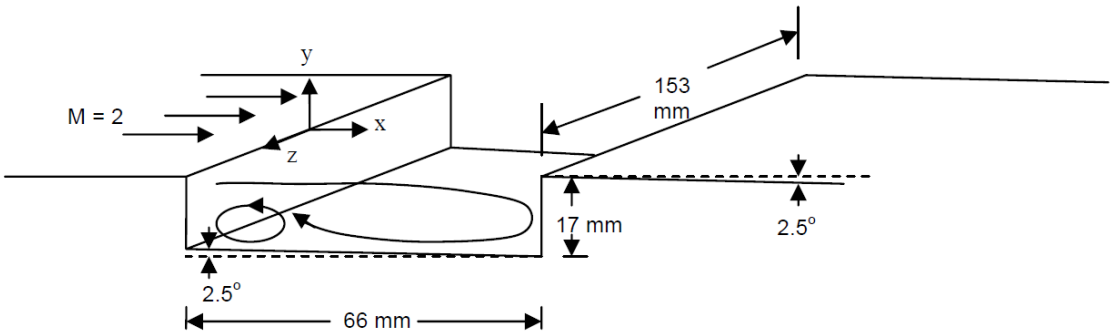


**Figure 3-4: Mach 2 cavity pilot flow used by Lahr et al. [9, 10].**

closing the back pressure valve, data from Lahr's "low-backpressure" case (i.e. backpressure valve fully open) will be presented here. For convenience, the run conditions for the "low backpressure" condition are given in Table 4-1 along with the run conditions for the current study. The higher pressures used in the current study were used to help promote ignition.

The grid locations for the low backpressure condition are given in Figure 3-5 with mean velocity and RMS Fluctuation values shown in Figures 3-6, and 3-7 respectively. A few key features of these figures will be discussed here for further comparison to the current work in later sections. Freestream velocities are around 700 m/s, and cavity velocities are around -50 m/s to -100 m/s. This strong recirculation indicates that the cavity is providing the intended flame holding capability. As indicated by the rapid velocity change in Figure 3-6, the shear layer for this configuration is centered at y=0 mm (or in line with the step). The RMS Fluctuations, primarily a function of turbulence, are strongest in the shear layer and are higher in the cavity than in the freestream. This increased turbulence in the cavity should assist in fuel air mixing.

With this baseline established, this thesis will now focus on the current work and assess the effect of an angled, rear cavity wall both with and without a strut.

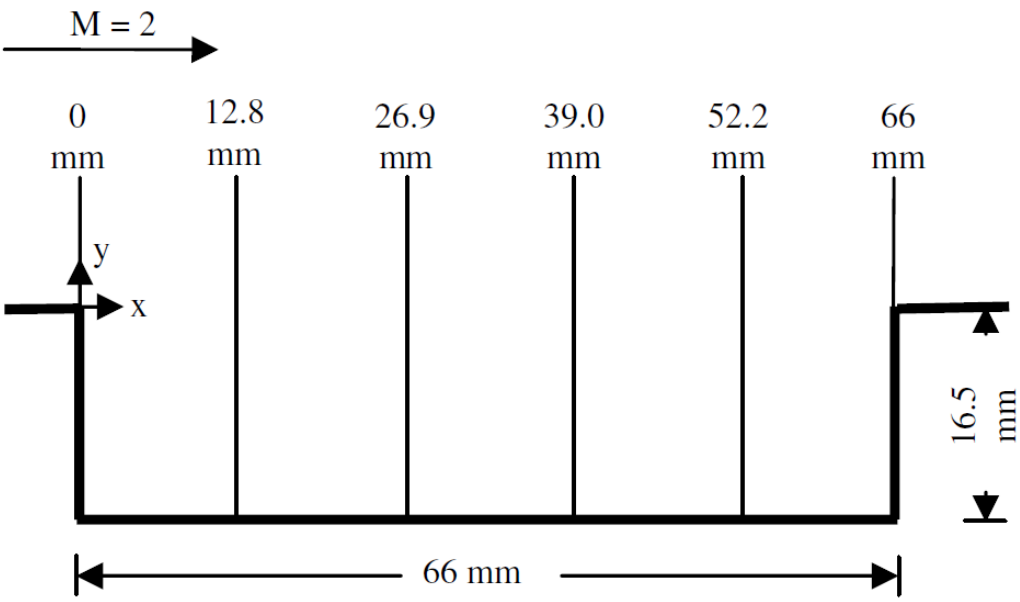


**Figure 3-5: Cavity schematic showing grid profile locations used by Lahr et al. [10].**

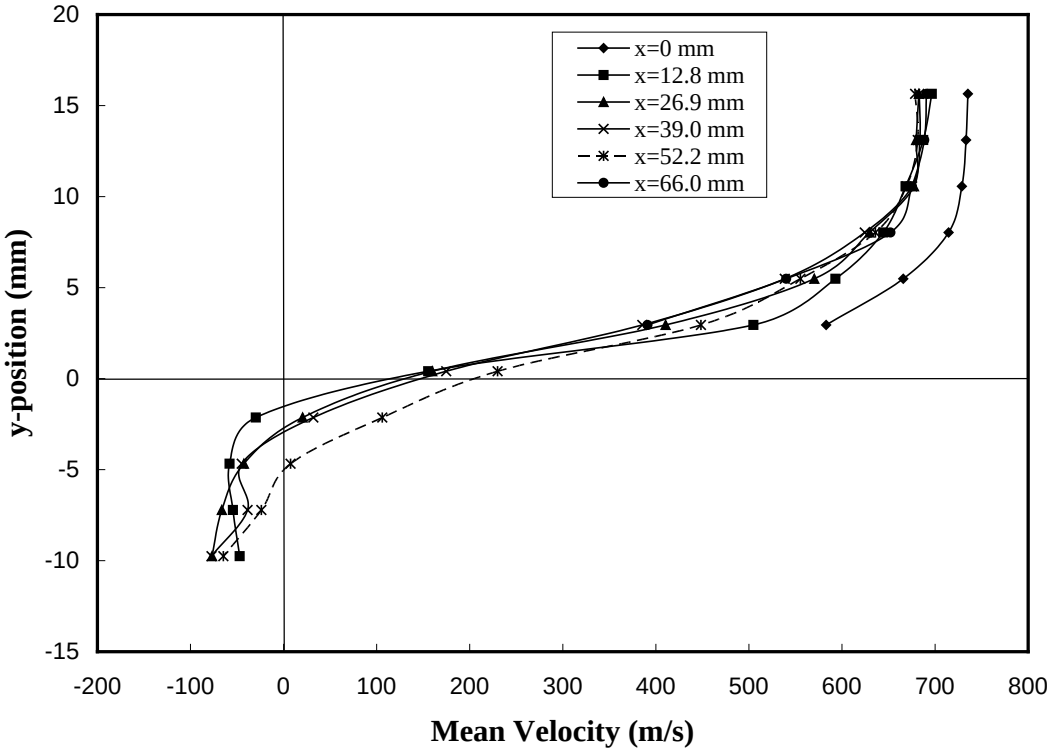


**Figure 3-6: Mean velocity profiles at different streamwise locations (x) where x = 0 and y=0 are at the step. Profiles shown at z = 0 mm on the centerline of the cavity from Lahr et al. [10].**

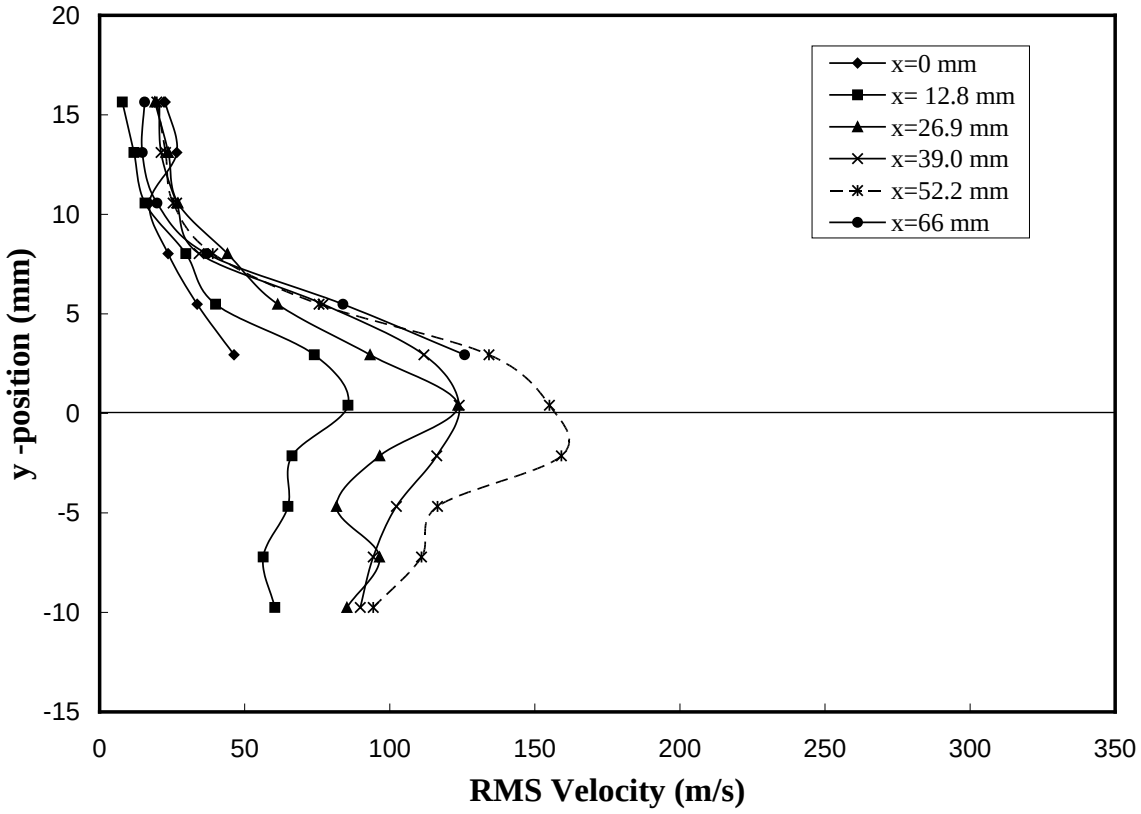


**Figure 3-7: RMS fluctuation profiles at different streamwise locations (x) where x = 0 and y=0 are at the step. Profiles shown at z = 0 mm on the centerline of the cavity from Lahr et al. [10].**

# Chapter IV

## HTV OVER A RECTANGULAR CAVITY WITH ANGLED REAR WALL WITH AND WITHOUT A STRUT

### 4.1 Laser and Optical Set-Up

The current laser set-up is very similar to the one used by Lahr and described in section 3.3 but with six notable exceptions: 1) due to alignment concerns the 193 nm grid and the 282 nm sheet were not rotated 2.5° to be parallel with the cavity floor, 2) the 282 nm read sheet was not retro-reflected back into the tunnel, 3) the lens used was a 100 mm fl f/2.8 (Cerco), 4) the filters to block background scattering were LC-300-325-50 UV-B manufactured by Laser Components GmbH, 5) a UV enhanced aluminum mirror directed the 308 nm OH fluorescence into the camera, and 6) the optics were arranged in such a way that data for two streamwise locations could be taken without having to realign the optics. All other components remained unchanged as can be seen in Figure 4-1. The estimated 282 nm sheet thickness at the grid is ~150 µm. The ArF laser energy at 193 nm was 7.5 mJ and 6.5 mJ for the no-strut configuration, and 4 mJ and 6mJ for the strut configuration. The two 193 nm laser energies given for both configurations represent the energy for each beam path before the grid optics.

### 4.2 Post-Processing Method

The post-processing method used in this study was developed by Marc Ramsey of Vanderbilt University [20], and is capable of finding intersection with sub-pixel accuracy. The code uses a template matching method with several linear and rotational degrees of

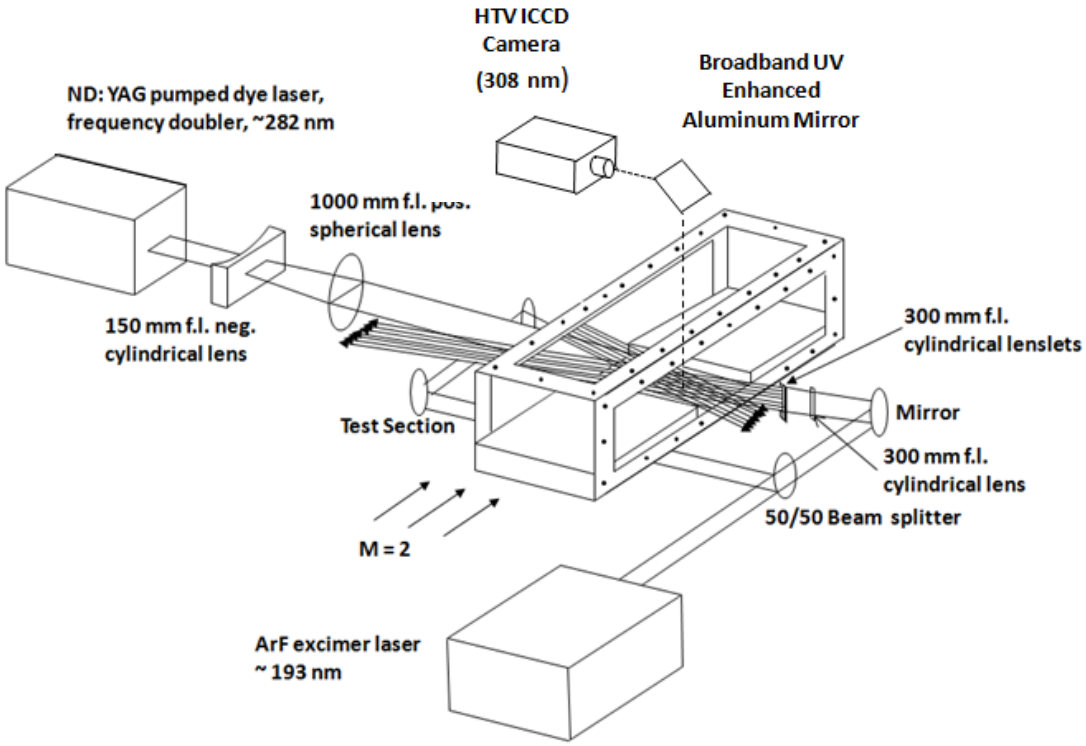


**Figure 4-1: Schematic of HTV system used in current work.**

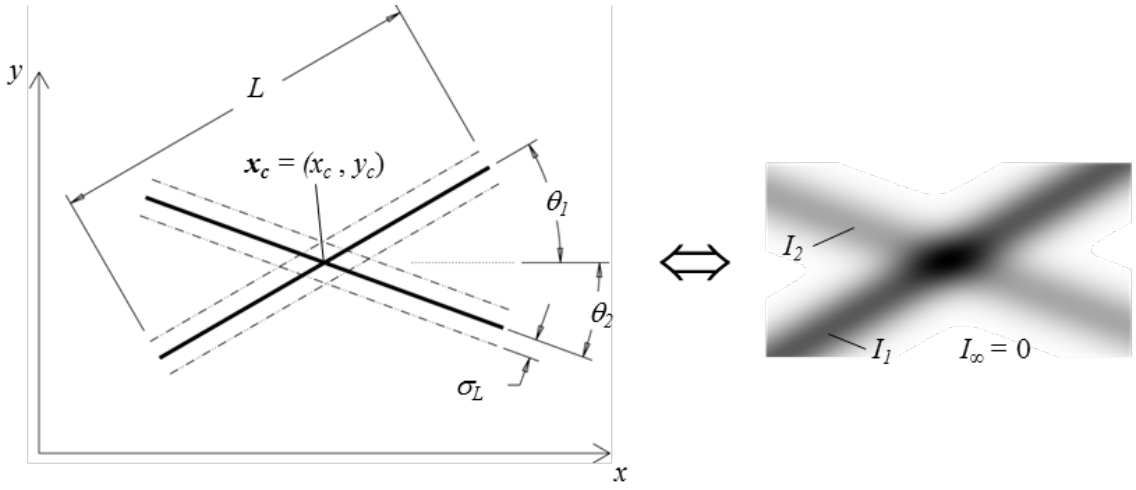


**Figure 4-2: Gaussian intersection template $\mathbf{G(x_c, \theta_1, \theta_2, \sigma_L, r_I, L)}$. The ratio of the amplitudes of the two Gaussian profiles $\mathbf{I_2/I_1}$ is $\mathbf{r_I}$. This template maps to image $\mathbf{I_T(G, x)}$ shown at right within window $\mathbf{W(G)}$ bounded by the smallest rectangle which contains both lines (from Ramsey et al. [20]).**

freedom to best match each of the intersections in a given image as seen in Figure 4-2. The advantage of using template matching versus a direct cross correlation, is that intersection uncertainty is minimized as shown in Figure 4-3. Ideally, these methods would be matching the signal of one image, S, to the signal of another image, S' (i.e. undelayed to delayed). However, in practice cross correlations also match the noise, N, of one picture to the noise of another picture, N'. Therefore, most of the uncertainty in the intersection location is due to the product of these two noise sources as shown in Equation 4-1.

$$(S+N)(S'+N')=SS'+SN'+NS'+NN' \tag{4-1}$$

However in template matching, the signal of one smooth template, $S_T$, is compared to another smooth template thereby eliminating the noise-noise term from the intersection uncertainty shown in Equations 4-2 (a) and (b) where prime indicates the delayed image:

$$S_T(S+N)=S_TS+S_TN \tag{4-2a}$$

$$S'(S'+N')=S'_TS'+S'_T\mathrm{N}' \tag{4-2b}$$

The precision of this method is highly dependent on the signal to noise (SNR) of the original images as shown in Figure 4-4. For low SNR, template matching and cross correlation are comparable in accuracy; however, for high signal to noise ratios the template matching technique has significantly greater accuracy. Typical SNR for the images in this study are 4 to 6 yielding a measurement precision of <1-2%. As will be discussed later, the SNR of some intersections were around 1-2 due to beam clipping or window deposits. The RMS fluctuation for these intersections is considerably higher than other intersections in the same grid.

The Gaussian templates, G, from the undelayed image are then compared with the templates from the delayed image, G', as shown in Figure 4-5 to determine two linear (x, y) and two rotation (θ1, θ2) Lagrangian displacements in the two template coordinate

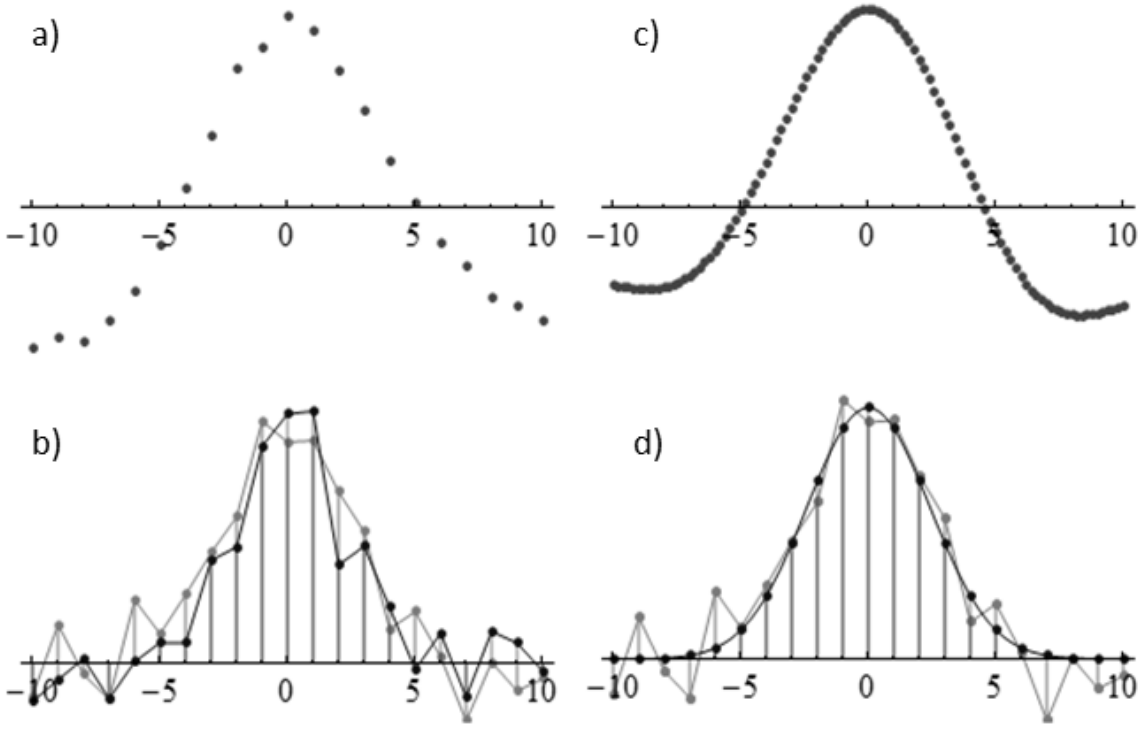


**Figure 4-3: Comparison of correlation methods on simulated 1D Gaussian signals with normally distributed additive noise at SNR = 2. a) shows the direct cross correlation for the two noisy signals in b) and is only calculated at integer displacements. c) is the template correlation for one of the same signals and a Gaussian template as shown in d). The template correlation is cleaner and can be interrogated at sub-pixel resolution, shown here at intervals of 0.2 pixel (from Ramsey et al. [20]).**

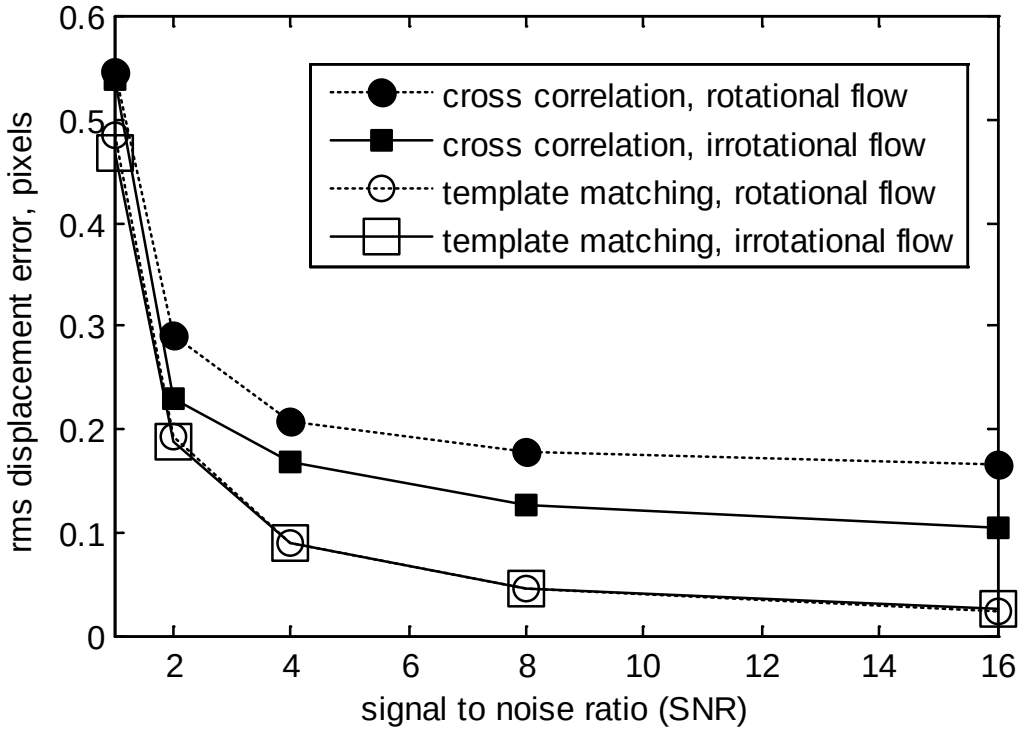


**Figure 4-4: Linear displacement error for the two methods as a function of SNR. Each data point represents a statistical sample of ~1300 tracked intersections (from Ramsey et al. [20]).**

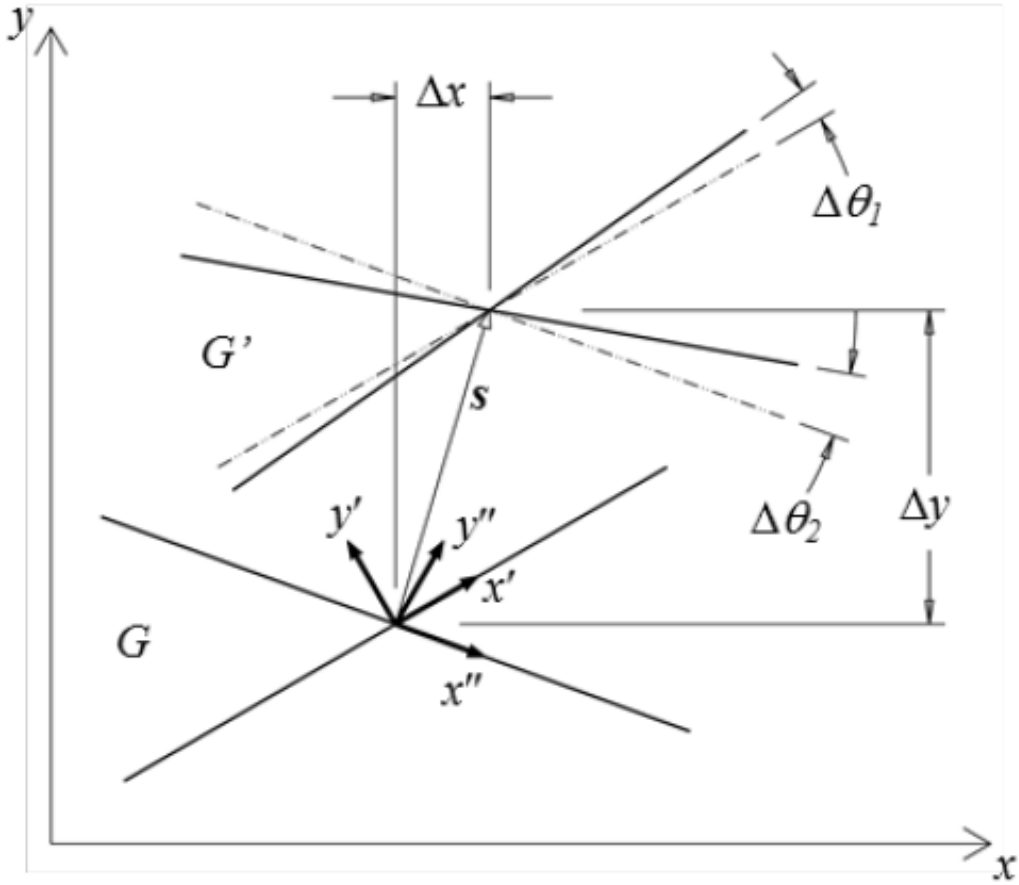


**Figure 4-5: Determination of Lagrangian displacement vectors from the undelayed (G) and delayed (G') templates from Ramsey et al. [20].**

systems. The rotational displacements are then used to determine the spatial velocity derivates. Having obtained all of these values in the template coordinate systems, they are then transformed into the global coordinate system. An interpolation method (linear, cubic, or Powell-Sabin) is used to obtain velocity profiles with sub-intersection resolution. Both the cubic and Powell-Sabin methods use multivariate bicubic splines between each intersection for interpolation; however, the Powell-Sabin uses measured derivatives (i.e. the rotational displacements) for interpolation whereas the cubic interpolation estimates these values. In irrotational flows, these two methods yield similar results, but in rotational flows the interpolated values can differ significantly. With these interpolated velocity profiles, y-axis (vertical) vorticity can be derived.

### 4.3 Ramped Cavity with No Strut Measurement and Velocity Analysis

The current study used the same wind tunnel as Lahr, but with a different cavity shown in Figure 4-6 where the primary difference between the two is the presence of an angled rear wall (or ramp). The origin of the xyz coordinate system both with and without the strut is set along the centerline at the corner of the leading edge step; the direction of each axis is labeled in Figure 4-6. As previously mentioned, the supply air was dry so water was added into the settling chamber to provide the moist flow needed for HTV. Run conditions and relative humidity for each run are presented in Table 4-1 along with those used by Lahr et al [10]. Once again, a higher pressure was used in the current study to promote ignition.

Sample images taken in this configuration can be seen in Figures 4-7, 4-8, 4-9, and 4-10 with a time delay of 2 μs between the two images. Figure 4-7 is a 300 shot averaged example of the undelayed “write” step of the HTV process used to locate the origin of the OH tags, while Figures 4-8, 4-9, 4-10 are single-shot images showing the delayed location of

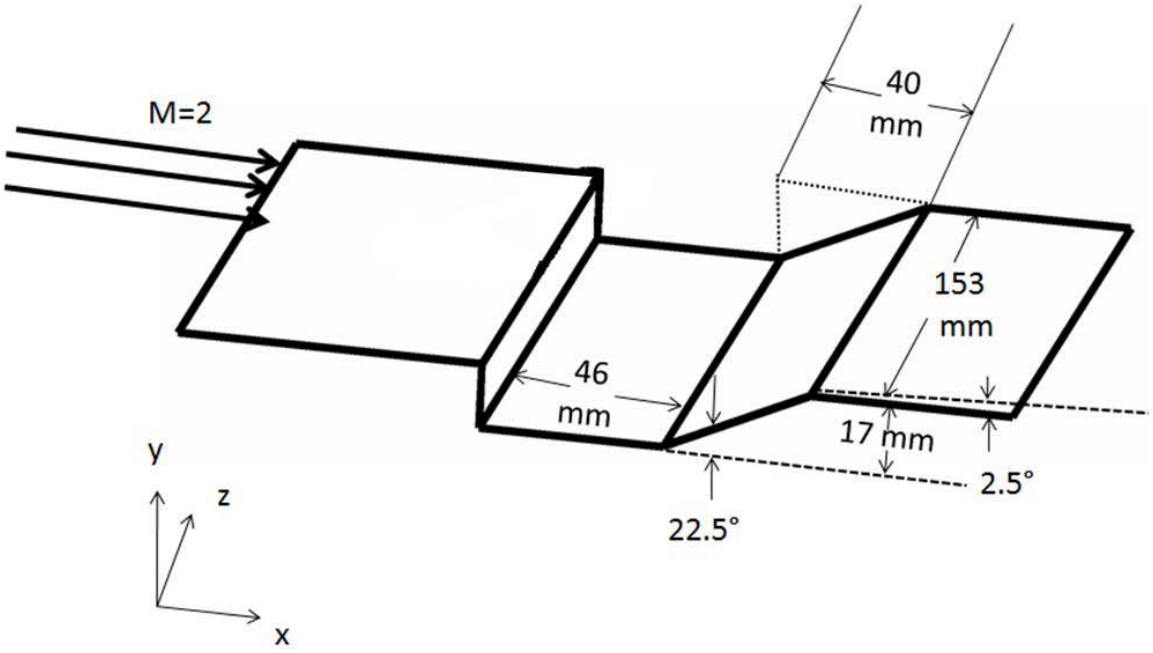


**Figure 4-6: Schematic of scramjet combustor test section with angled rear wall (i.e. ramp).**

**Table 4-1: Mach 2 Flow Conditions.**

| Test Configuration | Stagnation Conditions | | Isentropic Conditions | | | | |
|---|---|---|---|---|---|---|---|
| | $P_0$ (kPa) | $T_0$ (K) | P (kPa) | T (K) | Air mass flow rate (kg/s) | Water Mass Flow Rate (g/s) | Relative Humidity (%) |
| No-Strut | 410 | 590 | 53 | 330 | 3.2 | 25 | 4 |
| Strut | 210 | 560 | 26 | 310 | 1.6 | 25 | 9 |
| Strut Reacting | 450 | 600 | 58 | 330 | 3.5 | 25 | 3 |
| Lahr [10] | 170 | 520 | 22 | 290 | 1.4 | 25 | 26 |

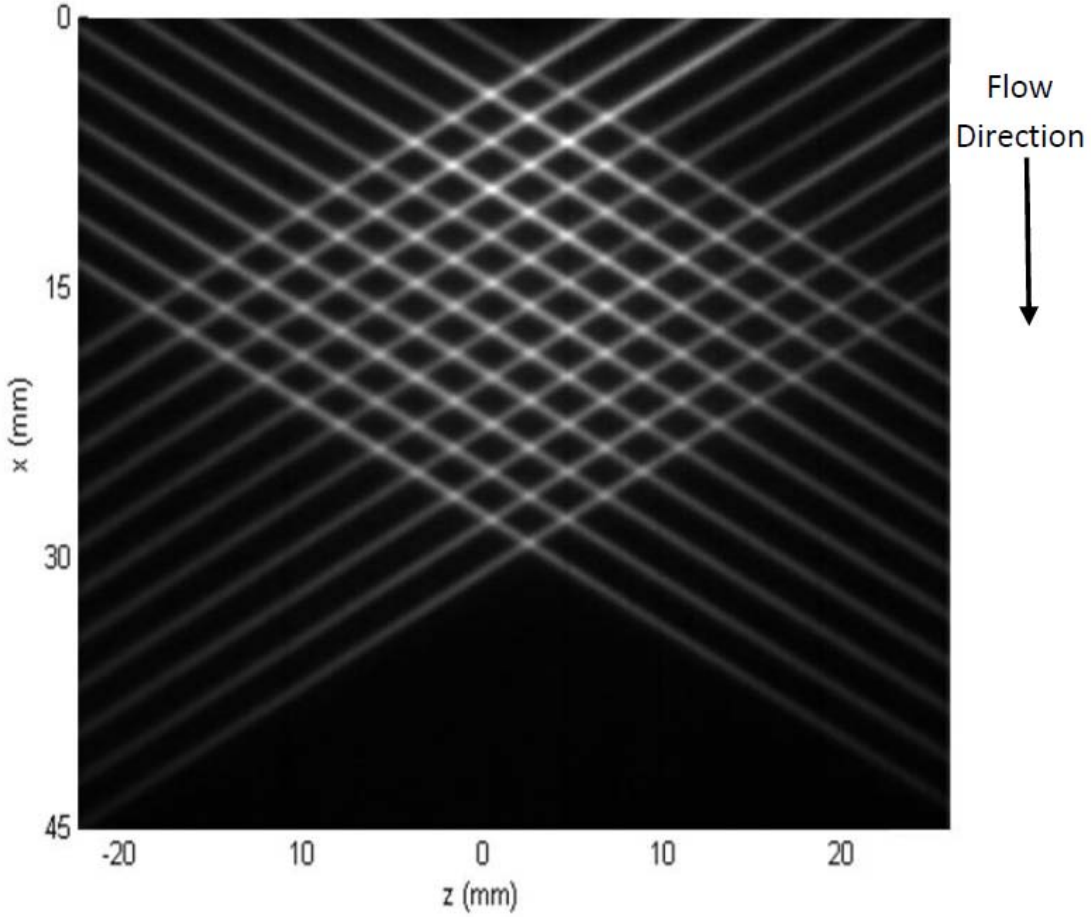


**Figure 4-7: 300 shot averaged undelayed image with no strut in the freestream at y = 7.62 mm.**

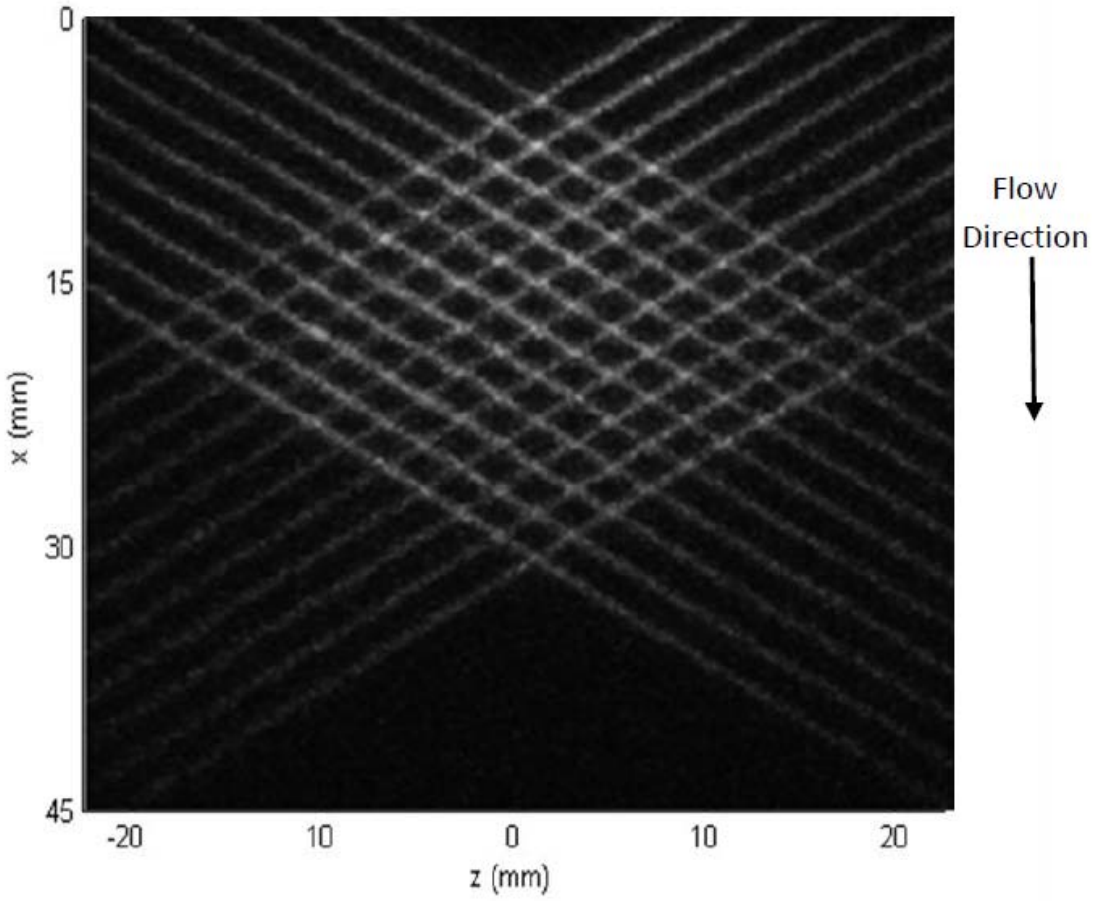


**Figure 4-8: Single-shot HTV image with no strut in the freestream; delay=2 µs; y = 7.62 mm.**

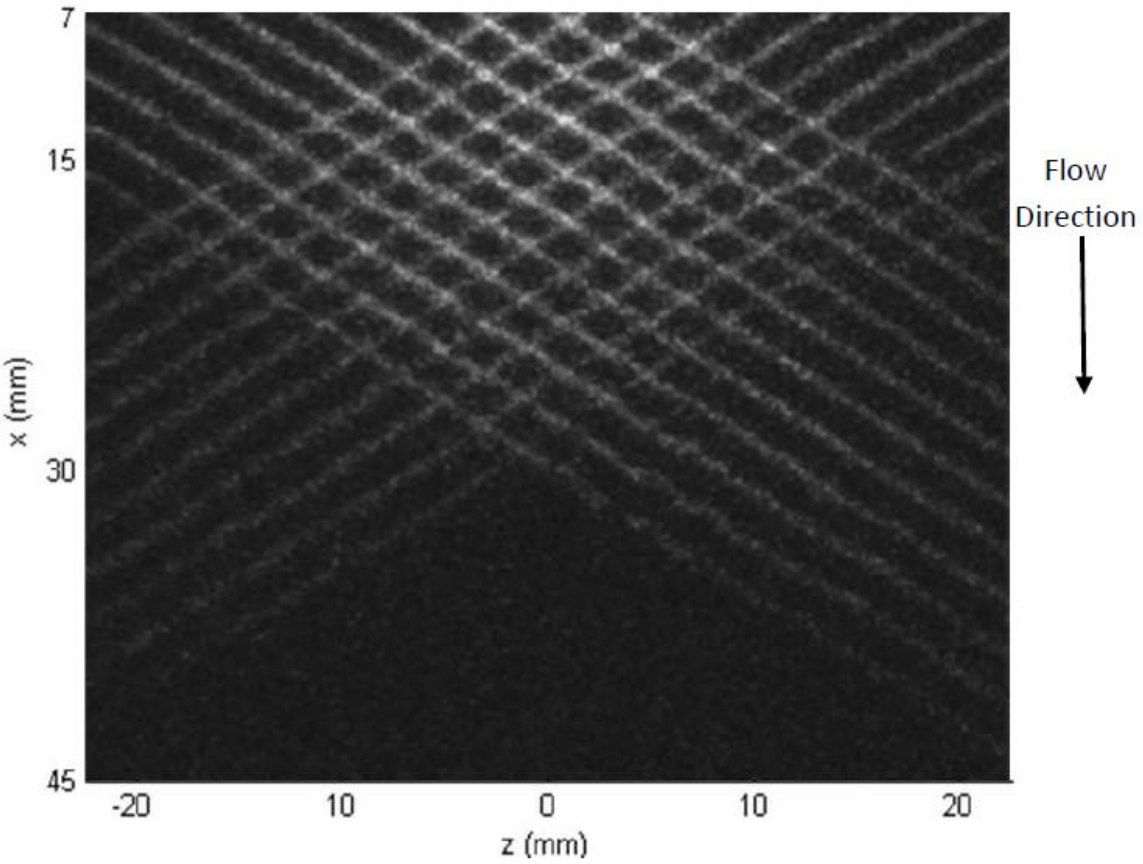


**Figure 4-9: Single-shot HTV image with no strut in the shear layer; delay = 2 μs; y = 0 mm.**

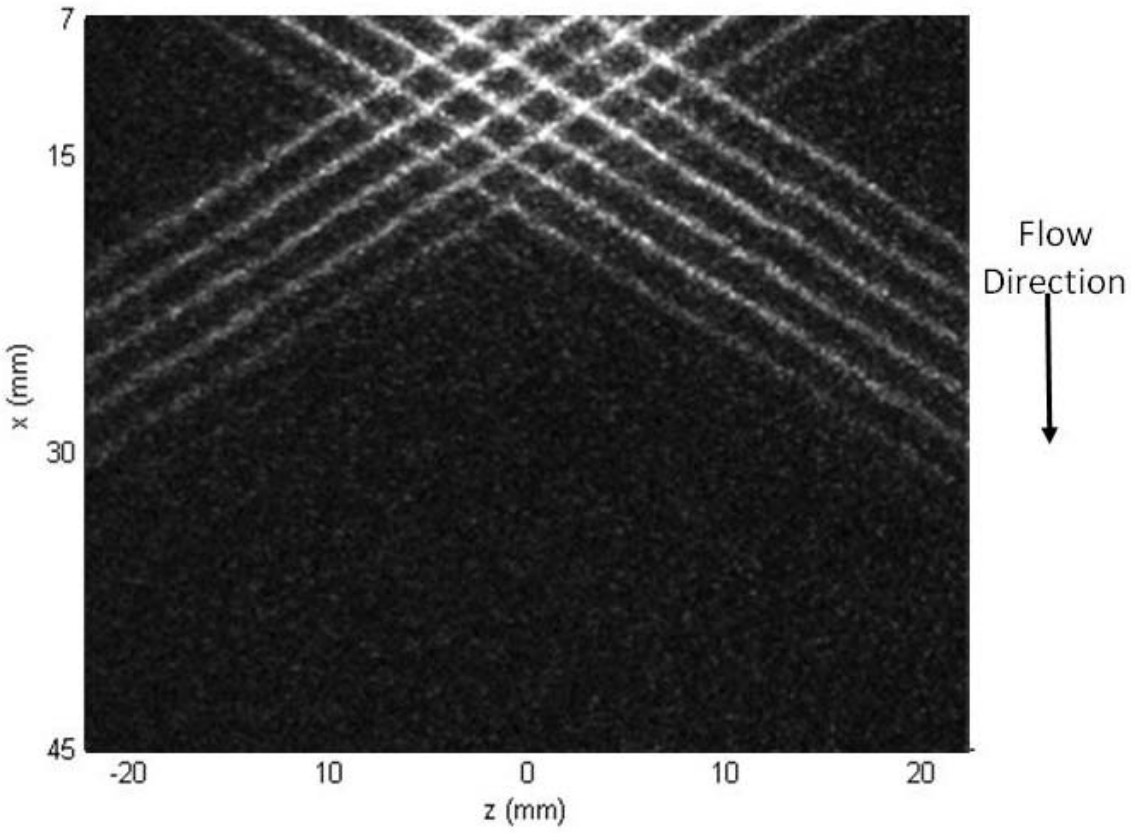


**Figure 4-10: Single-shot HTV image with no-strut in the cavity; delay = 2 μs; y = -12.7 mm.**

the tags. Due to laser scattering off the cavity step, the top portion of Figure 4-9 and 4-10 was truncated. Furthermore, one can notice some of the 193 nm grid lines in Figure 4-9 have been clipped by the rear ramp; this beam clipping is common for all cavity grids.

Velocity profiles were taken behind the cavity step and over the cavity ramp for the no-strut configuration as shown in Figures 4-11 and 4-12. Vertical sweeps were taken at the locations indicated in Figure 4-11 from 15 mm above the cavity step to 13 mm below the cavity step shown in Figure 4-12. 300 raw undelayed images were averaged together, and then fits were made for each of the averaged intersections to create an average velocity at each intersection. These average velocities at the grid points were then interpolated using a Powell-Sabin method for y = 12.7 mm, y = -2.54 mm, and y= -12.7 mm are shown in Figures 4-13, 4-14, and 4-15 respectively. For single shot profiles, fits are made for an individual frame then interpolated using a Powel-Sabin method as shown in Figure 4-16.The arrows in all figures (including those with color contours displaying RMS fluctuation or vorticity) represent the velocity magnitude at each grid point. The scale of each arrow was kept constant in all figures for consistency. The locations shown in Figures 4-13, 4-14, and 4-15 represent the freestream, shear layer, and recirculation cavity region respectively. An increase in velocity along the streamwise direction can be observed above the cavity (Figures 4-13) due in part to the expansion of the test section at 2.5°. Another possible cause for this increase in velocity, which will be discussed in more detail later, is the presence of an expansion wave which forms at the leading edge of a ramped-cavity [2, 4]. Figure 4-14 captures flow both in the cavity and in shear layer with the shear layer velocities having a greater positive velocity component. The fact that both regions can be seen at this location also indicates that the shear layer is being deflected down into the cavity.

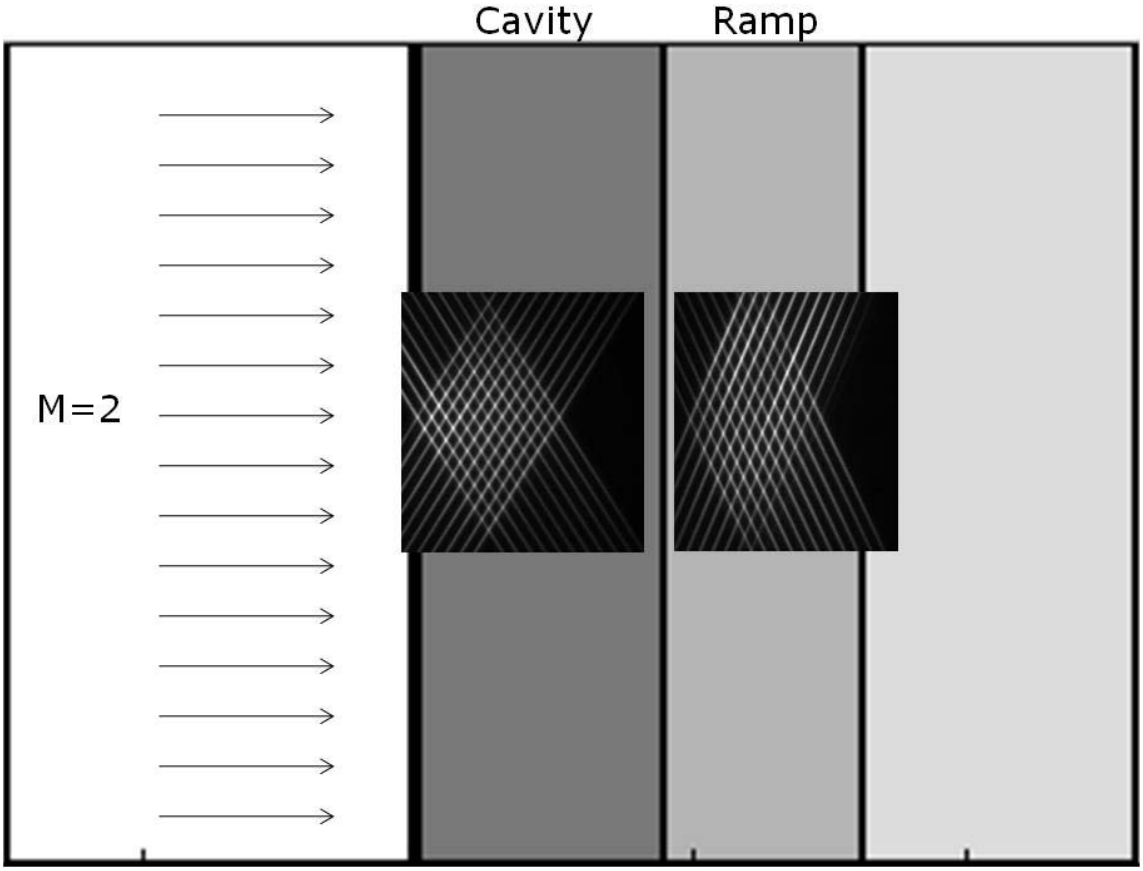


**Figure 4-11: Measurement locations for the no-strut configuration.**

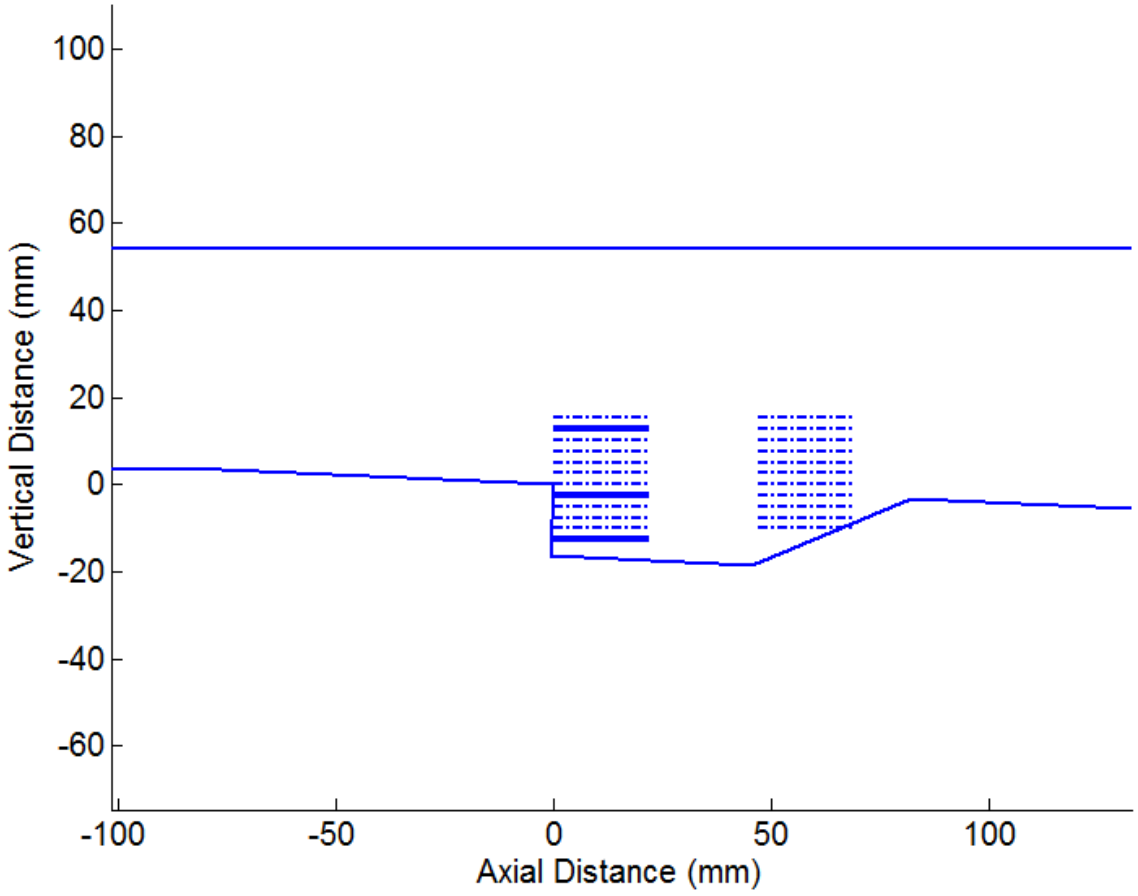


**Figure 4-12: Vertical locations of HTV grids for the no-strut configuration. The bold, solid lines represent the vertical locations of interest in this paper.**

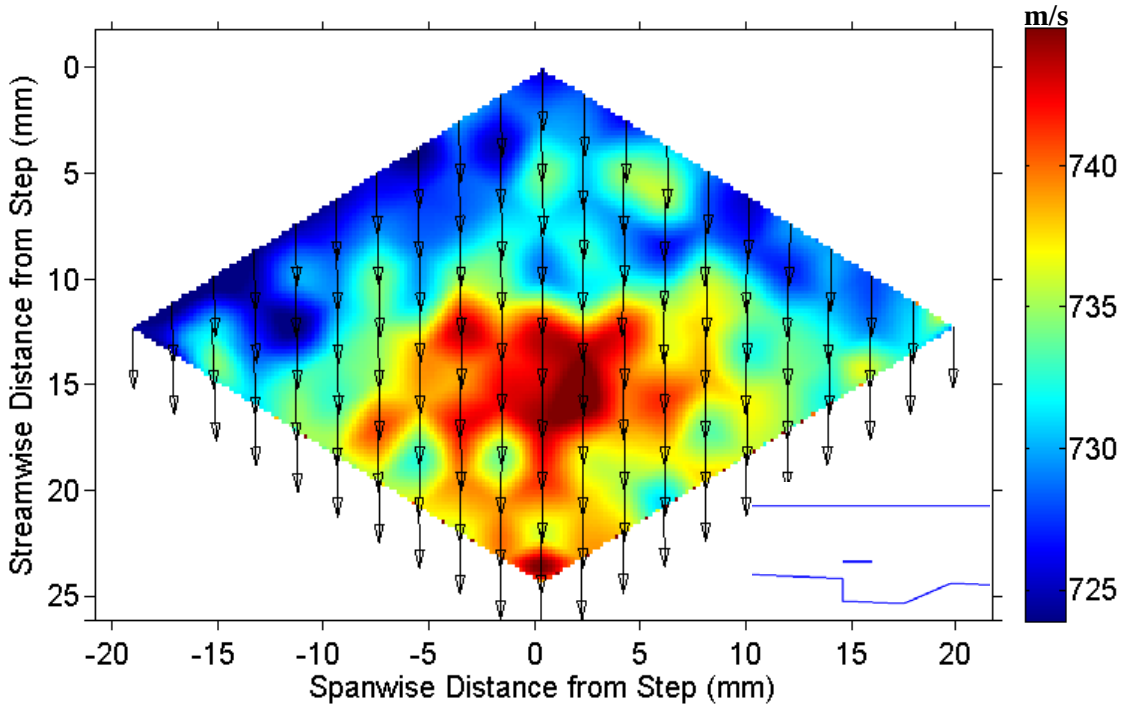


**Figure 4-13: Powell-Sabine interpolated 300 shot average streamwise velocity profile in the freestream at y= 12.7 mm in the no-strut configuration. Location shown in insert for clarity.**

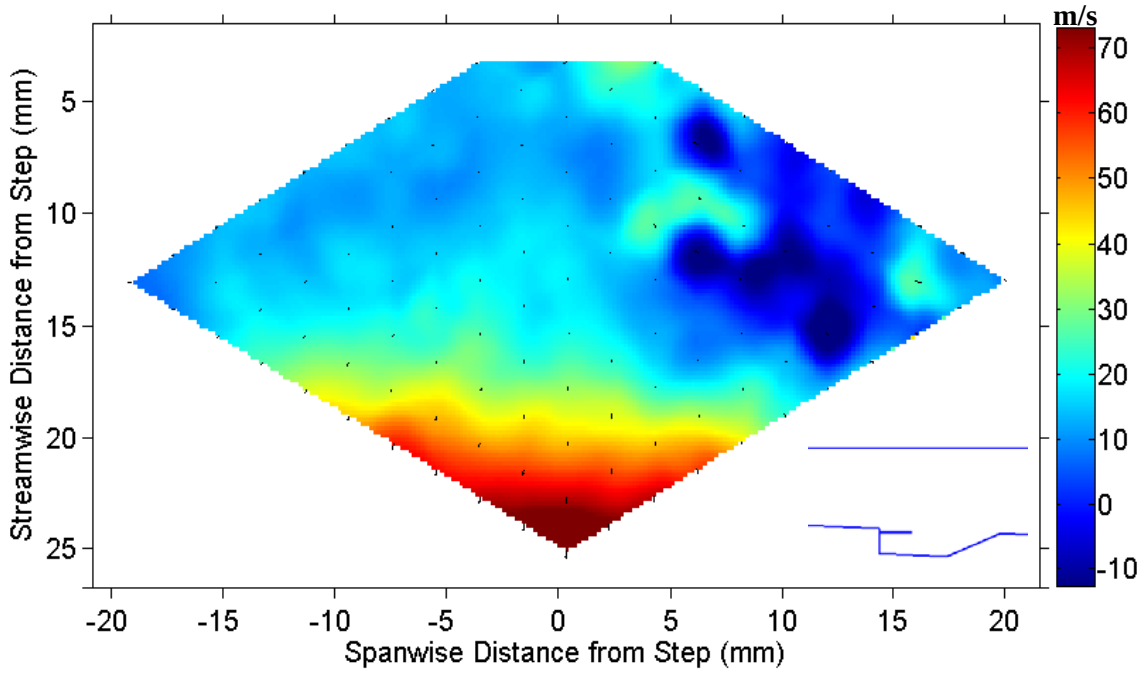


**Figure 4-14: Powell-Sabine interpolated 300 shot average streamwise velocity profile in the shear layer at y= -2.54 mm in the no-strut configuration. Location shown in insert for clarity.**

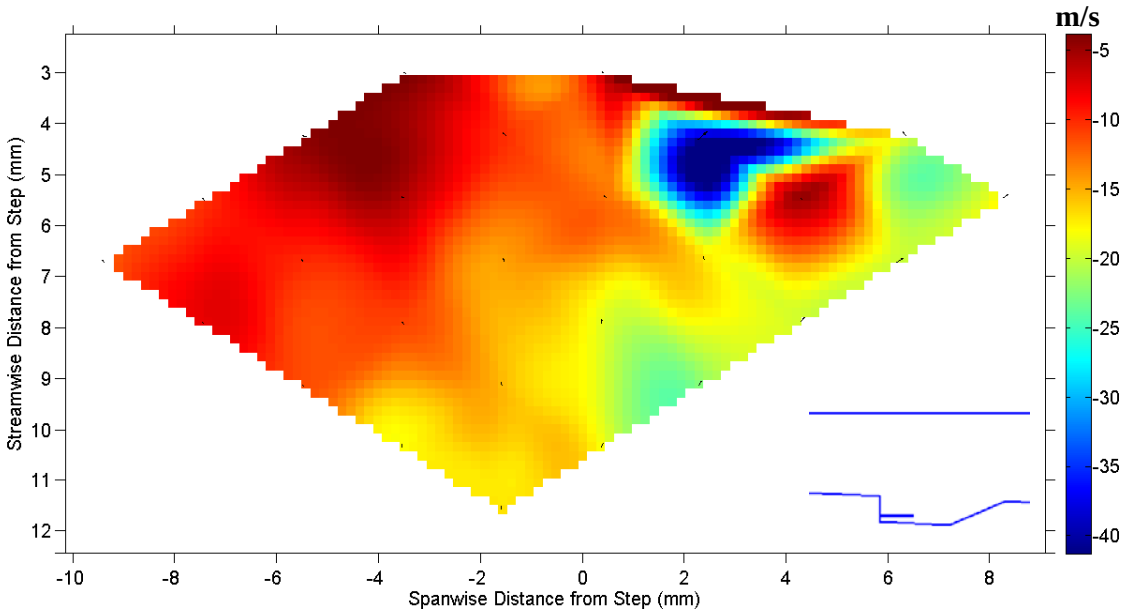


**Figure 4-15: Powell-Sabine interpolated 300 shot average streamwise velocity profile in the cavity at y= -12.7 mm in the no-strut configuration. Location shown in insert for clarity.**

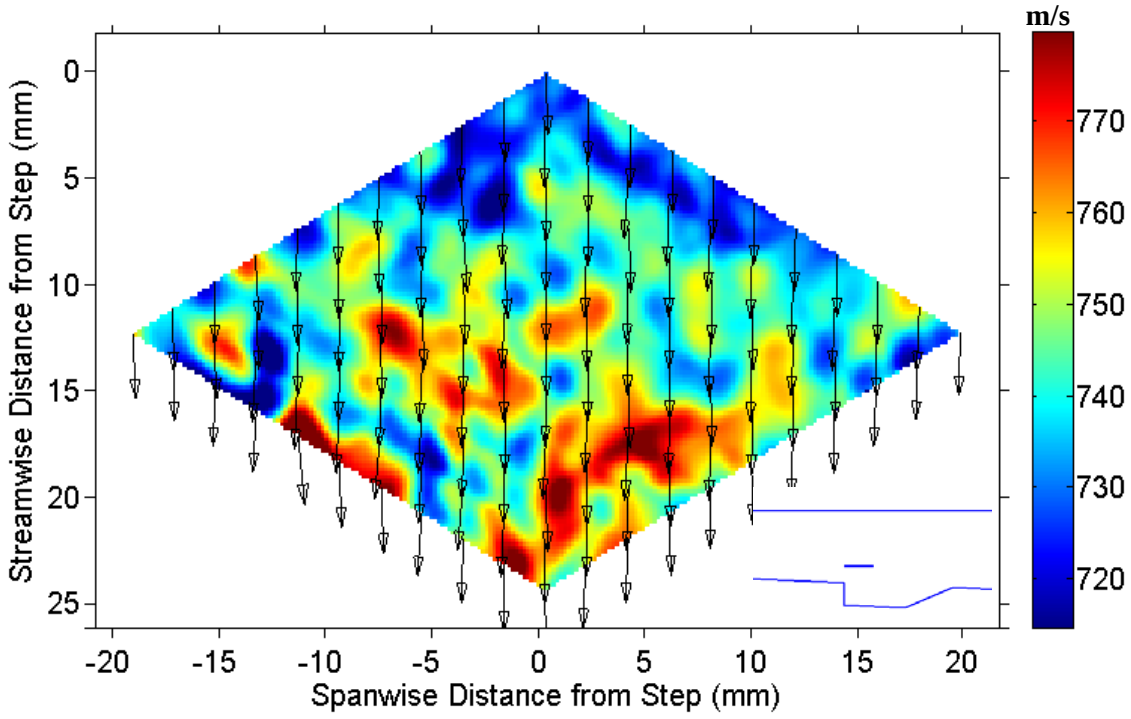


**Figure 4-16 Single-shot, Powell-Sabin interpolated image in the freestream at y =12.7 mm in the no strut configuration. Location shown in insert for clarity.**

RMS fluctuation values were determined by finding the RMS fluctuation for each grid intersection then interpolating between each grid intersection. RMS fluctuation values for these three vertical locations are shown in Figures 4-17, 4-18, and 4-19 using a cubic interpolation method. Since the RMS fluctuation of the angular displacements (used to determine the spatial derivatives) is not equivalent to the gradient of velocity RMS fluctuation, no spatial derivatives could be measured for RMS velocity fluctuations. Due to the lack of measured spatial derivatives of an RMS fluctuation, the Powell-Sabin interpolation method could not be used to interpolate RMS values. One would expect that the RMS fluctuation figures would be symmetric about the centerline of the cavity. However, there are various "hot spots" and incongruities in the figures relative to the expectations. The SNR of the images at these incongruities is substantially lower than the rest of the grid, and as mentioned before, measurement precision is highly dependent on the SNR of a given intersection. Most of these discrepancies are either along the edges of the grid where grid lines are generally weaker (as in Figure 4-17 and 4-19), to one side of the grid where there might be window deposits attenuating certain grid lines (as in Figure 4-18), or occasionally a sole intersection in the center of the grid where two particularly weak grid lines intersect (i.e. "hot spots" as in Figure 4-17 and 4-19). In either the template matching or cross-correlation methods, the correlation for a weak intersection will be pulled toward the brightest neighboring intersection which may fluctuate from one frame to the next. Therefore, "hot spots" tend to give errant velocity data and have very large RMS fluctuation values. Figure 4-10 taken in the cavity has examples of all three causes of low SNR intersections, and in particular a sole intersection in the middle of grid which is substantially weaker than its neighbors. As previously mentioned, correlation techniques will be pulled toward neighboring intersections and create artificially high RMS fluctuation values as seen

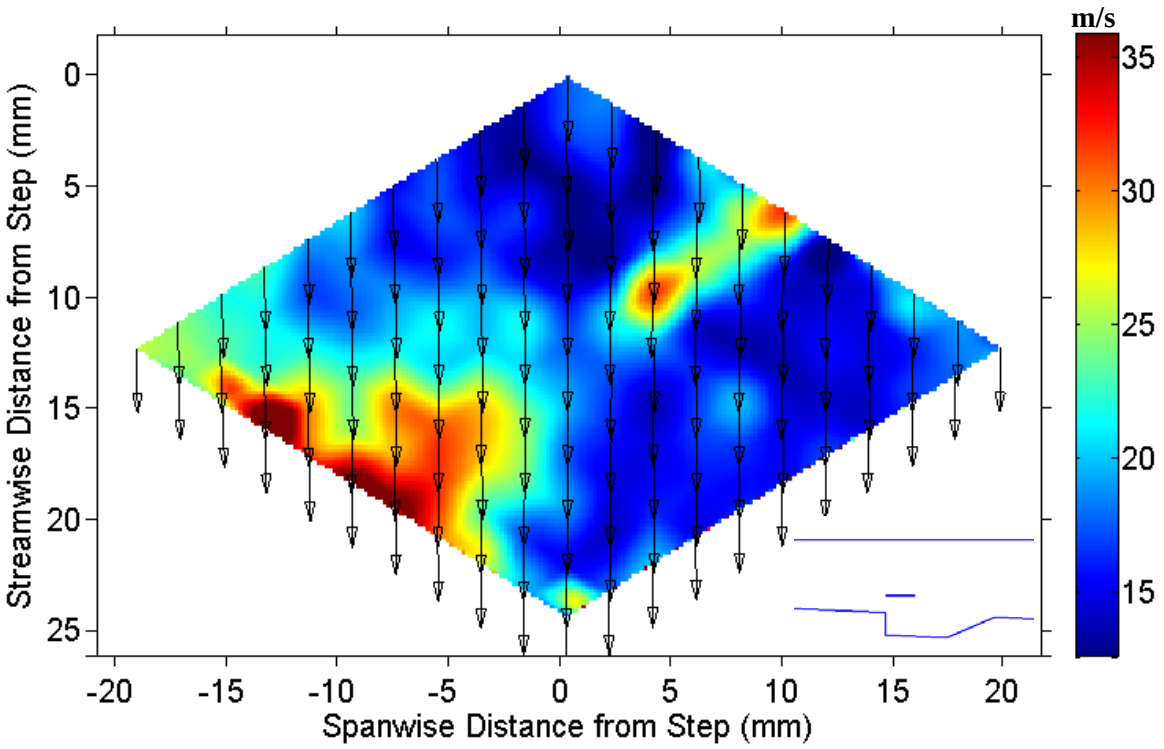


**Figure 4-17: Cubic interpolated Streamwise 300 shot RMS fluctuation profile in the freestream at y= 12.7 mm in the no-strut configuration with arrows showing mean velocity magnitude at the grid intersections. Location shown in insert for clarity.**

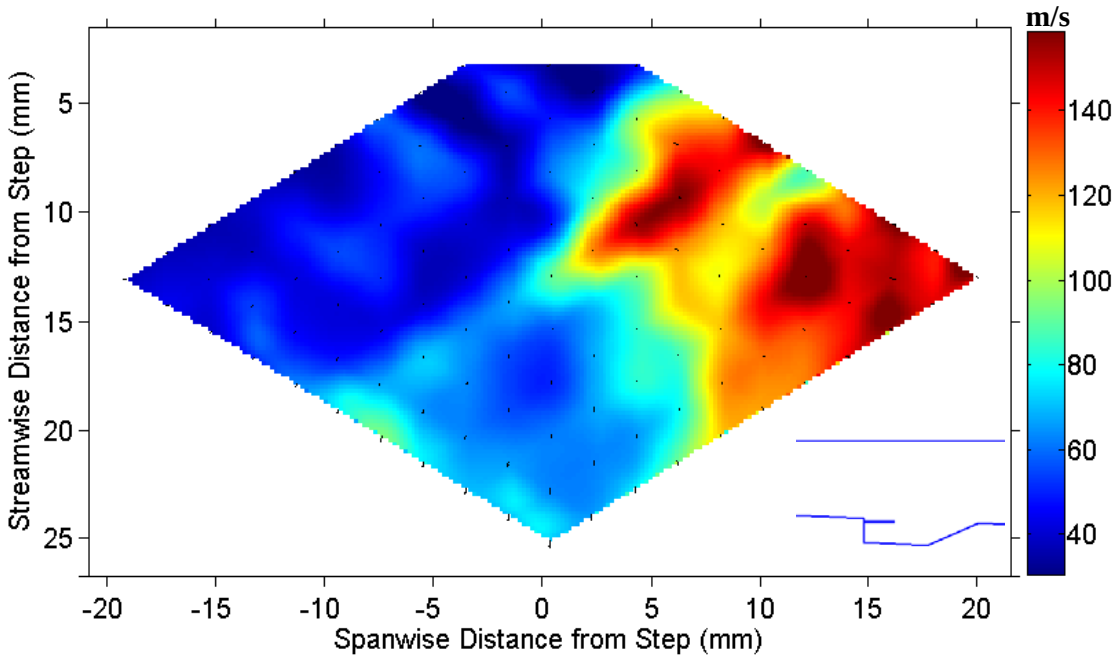


**Figure 4-18: Cubic interpolated streamwise 300 shot RMS fluctuation profile in the shear layer at y= -2.54 mm in the no-strut configuration with arrows showing mean velocity magnitude at the grid intersections. Location shown in insert for clarity.**

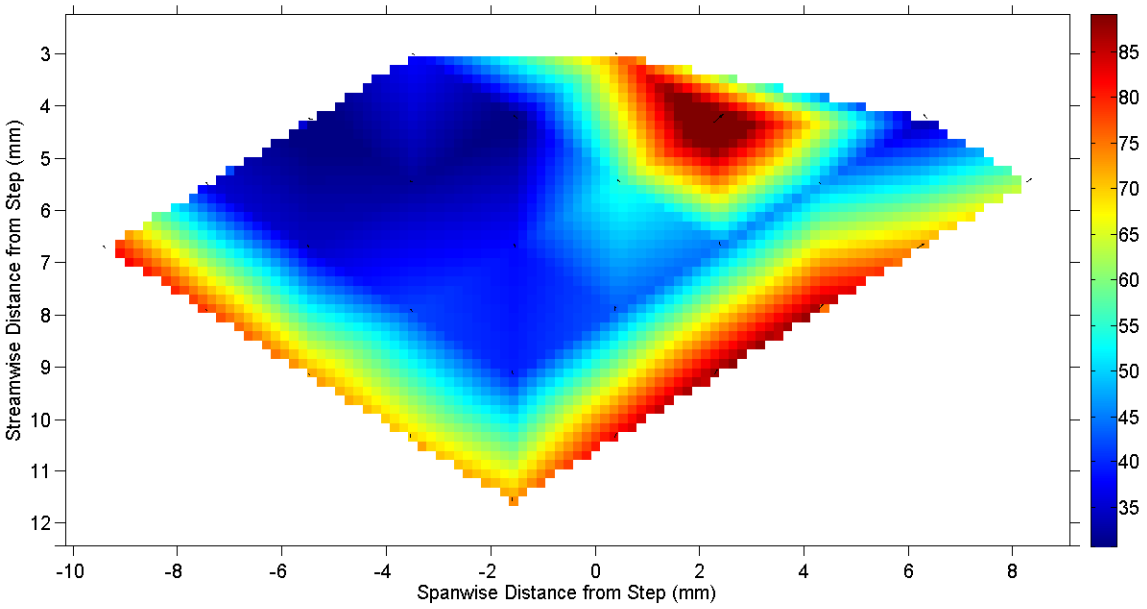


**Figure 4-19: Cubic interpolated streamwise 300 shot RMS fluctuation profile in the cavity at y= -12.7 mm in the no-strut configuration with arrows showing mean velocity magnitude at the grid intersections. Location shown in insert for clarity.**

in Figure 4-19. The end result of these low SNR intersections is lower measurement precision as indicated by Figure 4-4 and higher RMS fluctuations.

Figure 4-20 shows a side-by-side comparison of a velocity profile at y = -2.54 mm interpolated with Powell-Sabin (Figure 4-20 (a), identical to Figure 4-14) and with a cubic method (Figure 4-20 (b)). As can be seen in Figure 4-20, there are very few differences between the two interpolation methods in this scramjet configuration. RMS fluctuation peaks in the shear layer (Figure 4-18) and is the lowest in the freestream (Figure 4-17). Freestream RMS fluctuations range from 15 to 20 m/s, or 2 to 2.5% of the freestream value. These fluctuations in velocity result from a combination of timing uncertainty (0.4%), measurement precision (<2%), and flowfield turbulence. RMS fluctuation values derived from the template matching method were not significantly different than those derived from the cross-correlation technique as expected form Figure 4-4. This could be due to the cross correlation technique finding poor correlations and therefore misleading results, or because the primary source of fluctuation is from turbulence.

Figure 4-21 shows velocity profiles in the vertical direction along the centerline at several streamwise locations, and Figure 4-22 shows RMS Fluctuations at these same locations. The effect of the reduced SNR at certain grid intersections can be seen in these figures particularly in the intersection in the upstream portion of the cavity. At y = -5 mm there is a sudden increase in RMS fluctuation as seen in Figure 4-22 probably caused by a window deposit. Nevertheless, differences between the ramped-cavity figures and the rectangular cavity figures (Figures 3-5 and 3-6) can be seen. First, a wider spread in velocity values above the shear layer can be seen in the ramped-cavity than in the rectangular cavity. In the ramped-cavity, there was a noticeable increase in velocity as the flow moves downstream with the highest velocity being furthest downstream.

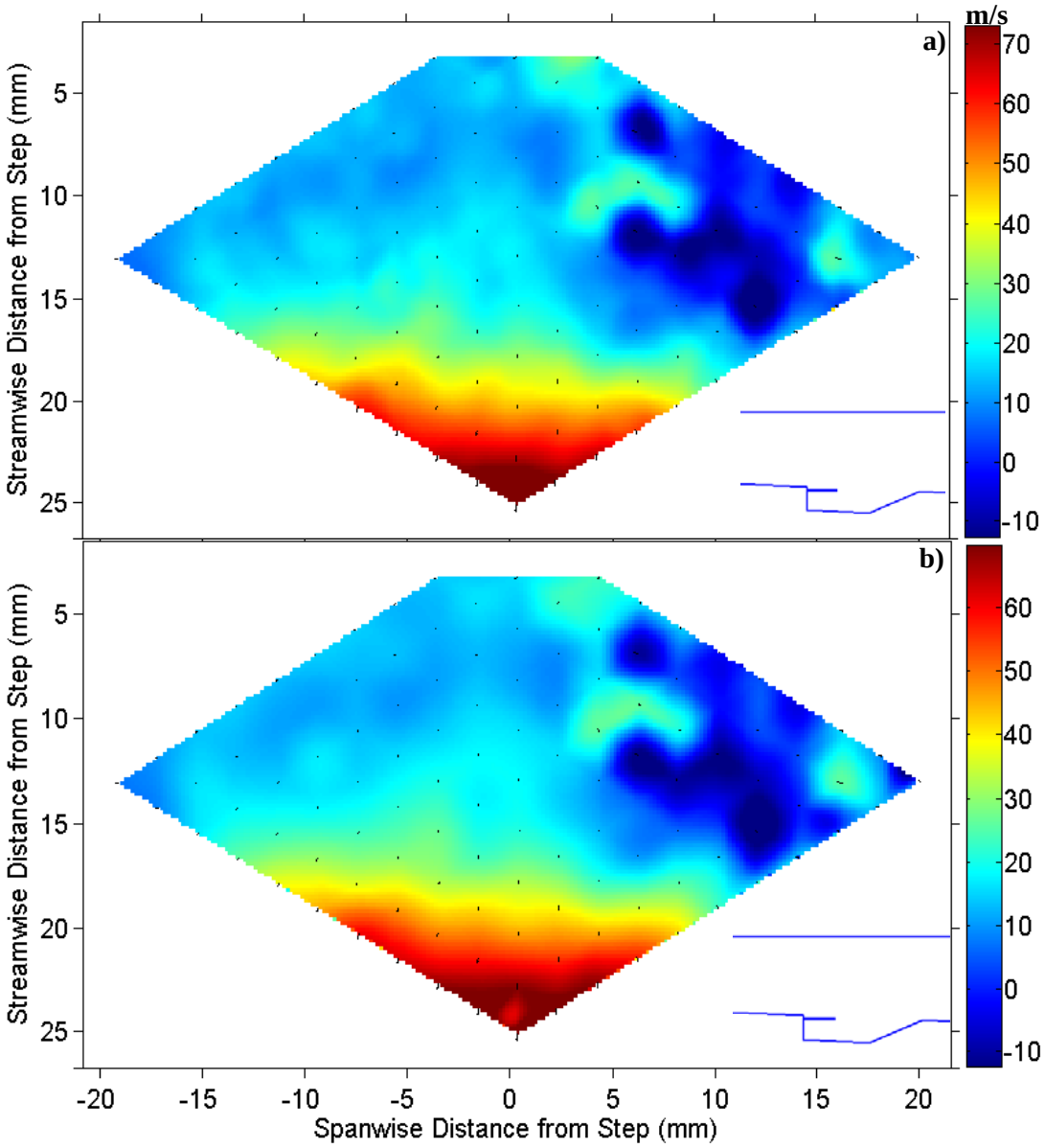


**Figure 4-20: Side-by-side streamwise 300 shot average velocity profile comparison of Powell-Sabin (a) and cubic interpolation (b) in the shear layer at y = -2.54 mm. Location shown in inserts for clarity.**

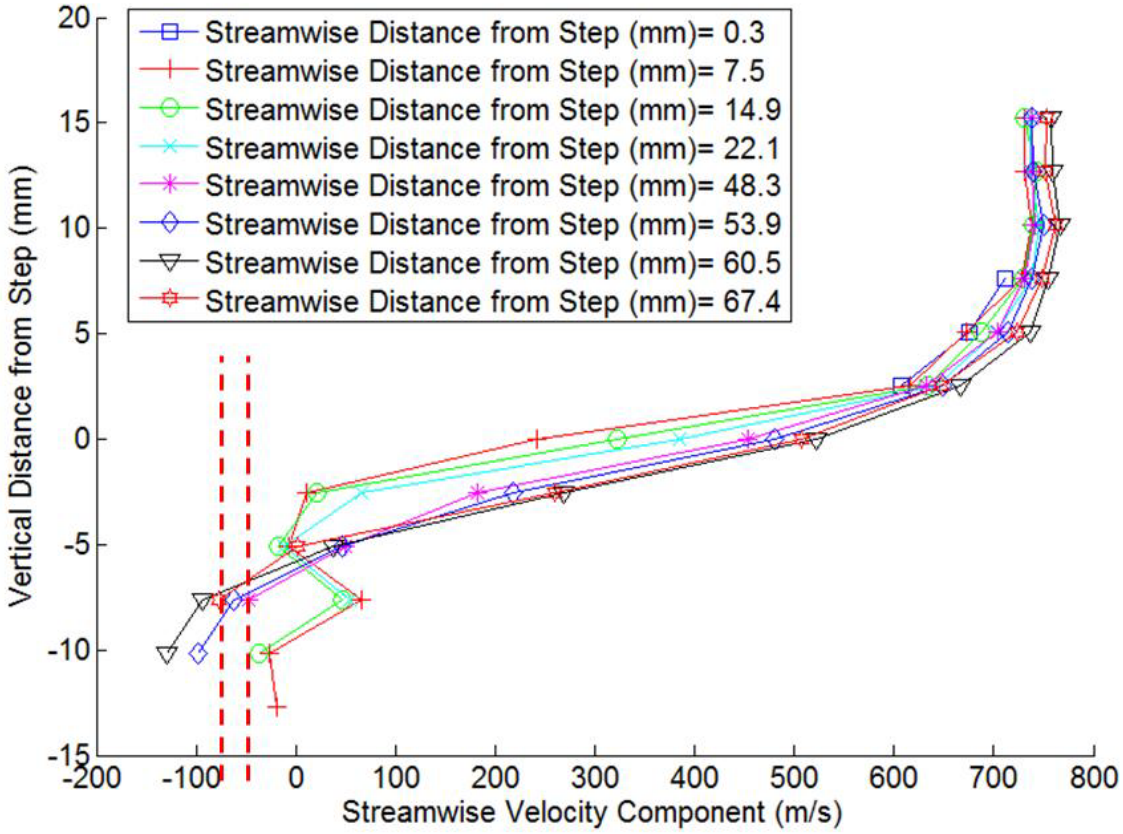


**Figure 4-21: 300 shot mean velocity profile along the centerline in the vertical (y) direction for the no-strut configuration at various streamwise (x) locations. Ramp is located 46 mm from the step. The dashed vertical lines represent the maximum and minimum observed recirculation velocities in the rectangular cavity by Lahr et al. [10].**

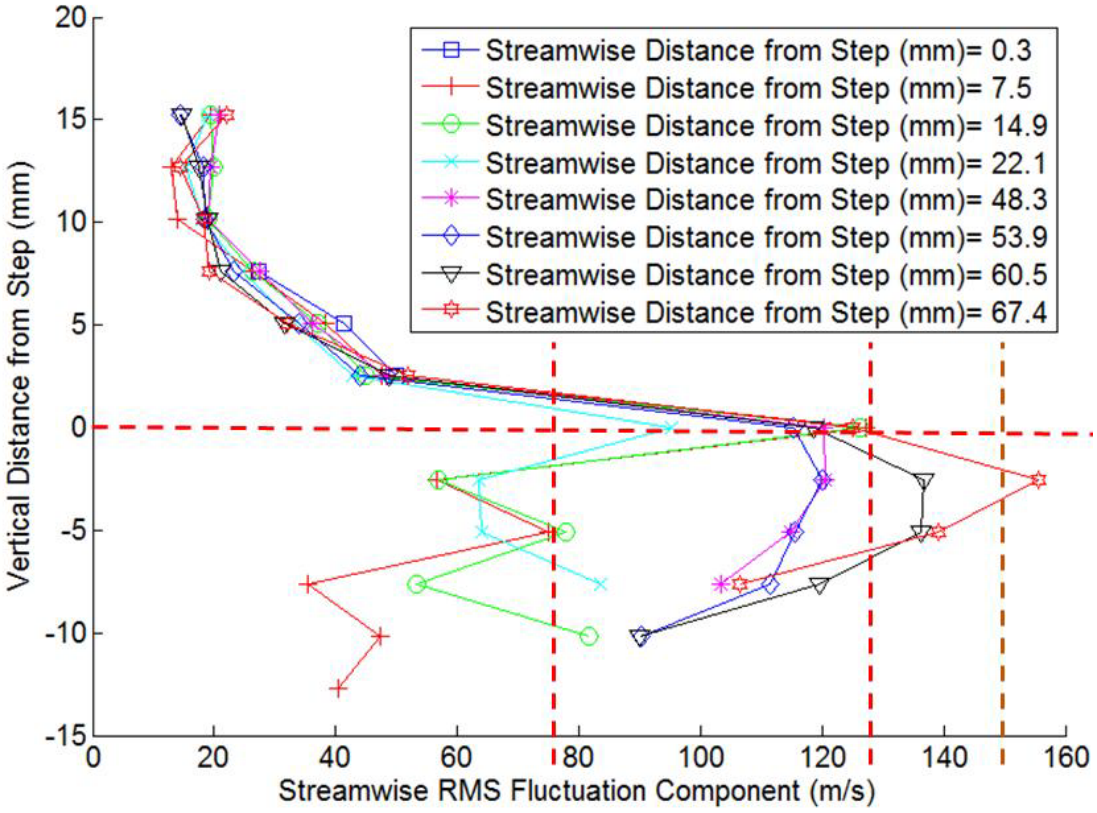


**Figure 4-22: 300 shot RMS fluctuation profile along the centerline in the vertical (y) direction for the no-strut configuration at various streamwise (x) locations. Ramp is located 46 mm from the step. The two leftmost dashed vertical lines represent the maximum and minimum observed recirculation RMS fluctuation in the rectangular cavity, and the rightmost dashed vertical line represent the RMs fluctuation over the rear cavity step. The dashed horizontal line represents the location of the shear layer observed by Lahr et al. [10].**

Whereas in the rectangular cavity, there was a slight increase in velocity as the flow moved downstream, but the highest velocity was at x = 0 mm (i.e. directly above the step). This is caused by the expansion wave which forms over the leading edge of ramped-cavity, x = 0 mm, as opposed to the shock wave which forms over a rectangular cavity [2]. The sudden decrease in the freestream velocity over the step seen in Figure 3-6, but absent in Figure 4-21, is caused by this shock. Second, the location of the shear layer is lower into the cavity confirming the literature [2]. Furthermore, the recirculation and turbulence over the ramp is higher compared to the rear of the rectangular cavity. In general, turbulence and recirculation remain similar throughout the whole cavity for both cavity configurations. If fuel was piloted into the cavity through this angled back wall, the aforementioned increase in turbulence and recirculation should aid in fuel-air mixing augmenting the cavities ability of flameholding. Figure 4-23 compares the data shown in Figure 4-21 (obtained using a different correlation scheme [19] as described by Grady et al [21]) with large eddy simulation CFD predictions made by Menon [22]. In general, there is very good agreement with the experimental and numerical data.

Figure 4-24 shows the estimated shear layer thickness versus the non-dimensional length x/D. Shear layer thickness is approximated by the vorticity thickness, $\delta_\omega$, seen in Equation 4-3.

$$\delta_\omega = \Delta U / \frac{\partial u}{\partial y}|_{max} \tag{4-3}$$

The rate of growth, $\delta'_\omega$, is roughly linear across the cavity as seen in Figure 4-24 with $\delta'_\omega \approx 0.05$. This value is roughly a third of that found in a supersonic flow over a rectangular cavity [9], and a sixth of that found in a supersonic flow over a rearward facing step [23].

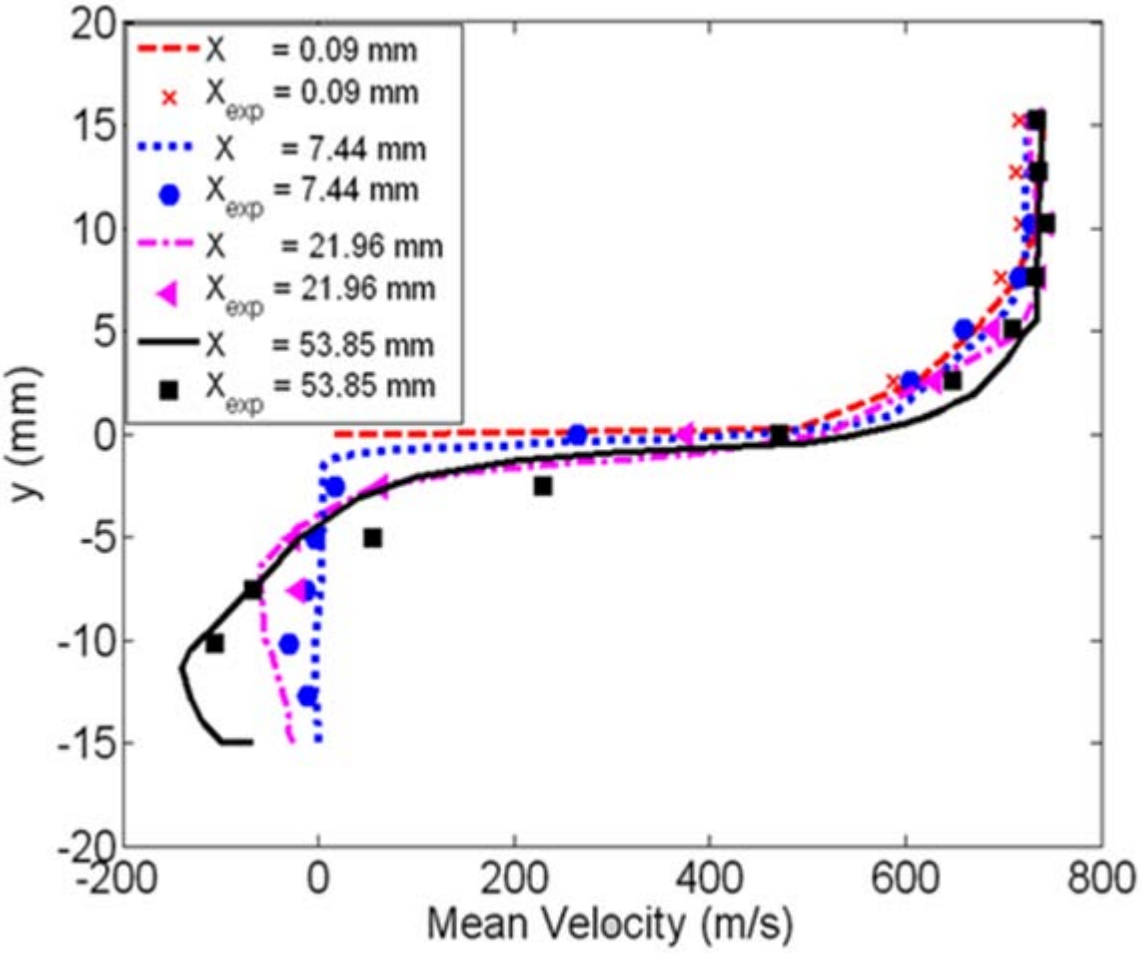


**Figure 4-23: Mean velocity profile along the centerline in the vertical (y) direction for the no-strut configuration at various streamwise (x) locations. Ramp is located 46 mm from the step. Lines represent LES CFD predictions made by Menon [22] and the points represent data from the current study using a different correlation method [19, 21].**

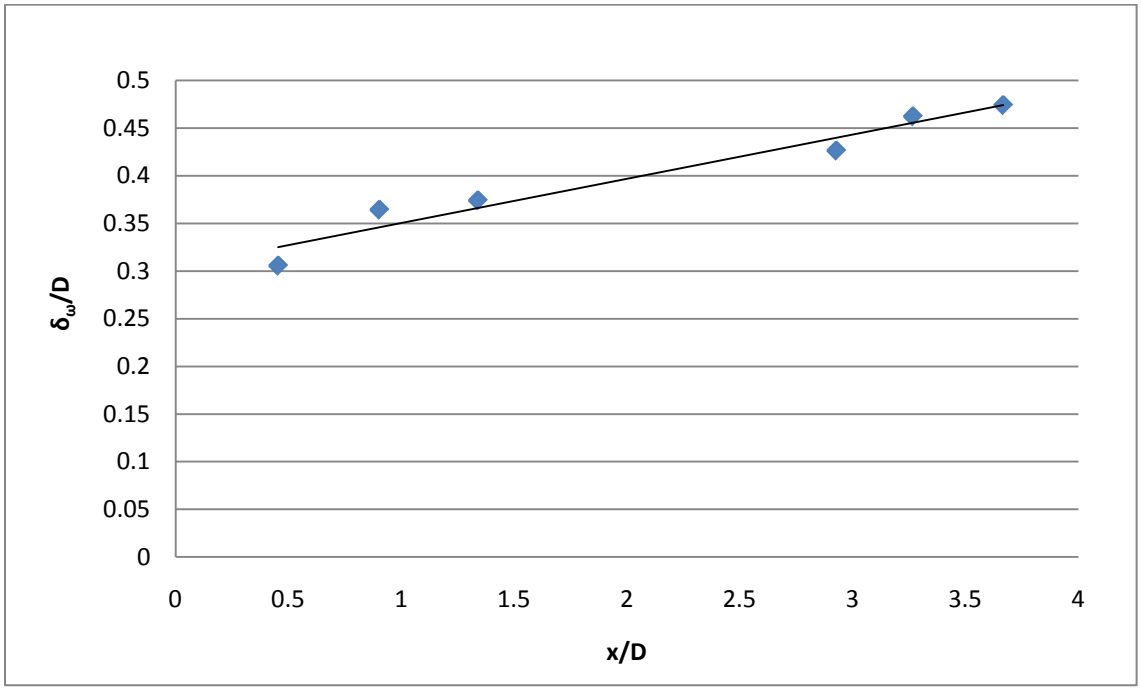


**Figure 4-24: Vorticity thickness of the shear layer where the initial growth rate is $\delta'_\omega$ = 0.05.**

While this reduction in shear layer growth is due in part to the higher pressure used in the current work, it stands to reason that the shear layer grows faster in the rectangular cavity than in the ramped-cavity. Considering this reduction and how the shear layer curled into the cavity, flame penetration into the main flow of the combustor is significantly lower in the ramped-cavity than in the rectangular cavity. Therefore, a means of increasing flame penetration is needed.

## 4.4 Ramped Cavity with Strut Measurement and Velocity Analysis

To augment the flame penetration into the main flow, a swept-leading-edge strut was placed on the cavity centerline so that it would be flush with the upstream edge of the cavity as shown in Figure 4-25. The strut was 25.4 mm in height, the leading edge had an 18.5° wedge and was swept by 30°, and the trailing edge was swept by 45° with a constant thickness of 6.4 mm. Due to these sweep angles, the strut was tapered towards the top and protruded 25.4 mm over the cavity. This strut geometry was chosen since "strut 2", of similar geometry, used by Hsu et al [24] created an optimal balance of mixing and flame penetration. The strut used in the current work has a smaller compression angle and is both narrower and shorter than "strut 2" used by Hsu et al. to reduce flow losses [24].

One vertical sweep was conducted in the wake region of the strut from 8 mm above the strut tip to 38 mm below the strut tip (or 33 mm above to 12.7 mm below cavity step) as shown in Figure 4-26 and 4-27. Figure 4-28 shows an LES CFD simulated profile of $\partial\rho/\partial x$ created by Menon [22] using the current experimental data to illustrate the compression/expansion patterns in this experiment. As can be seen in this figure, one would expect to find an expansion wave from the top trailing edge of the strut. It should be

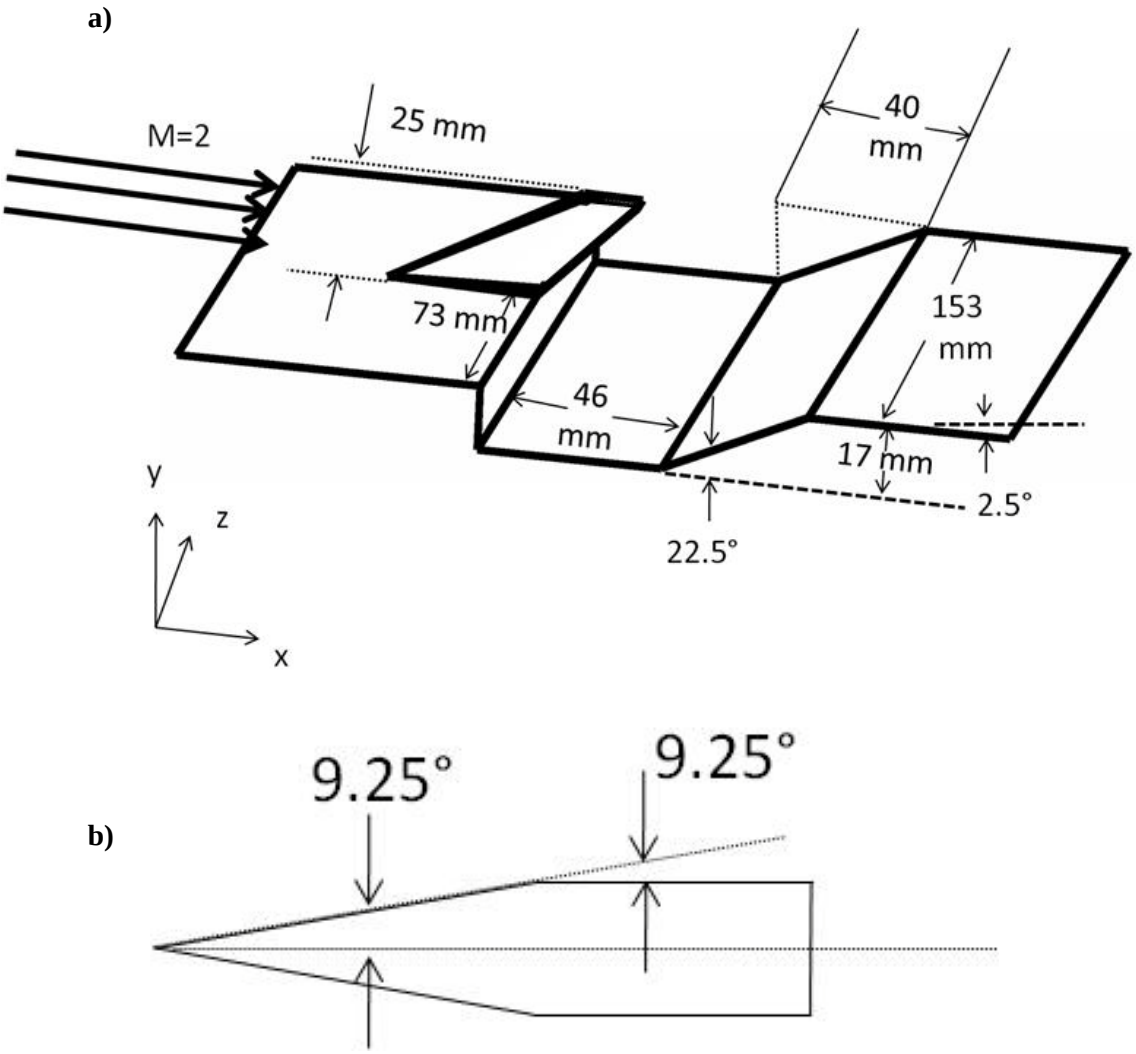


**Figure 4-25: a) Schematic of the scramjet combustor test section with ramped cavity and strut, and b) cross-section of strut.**

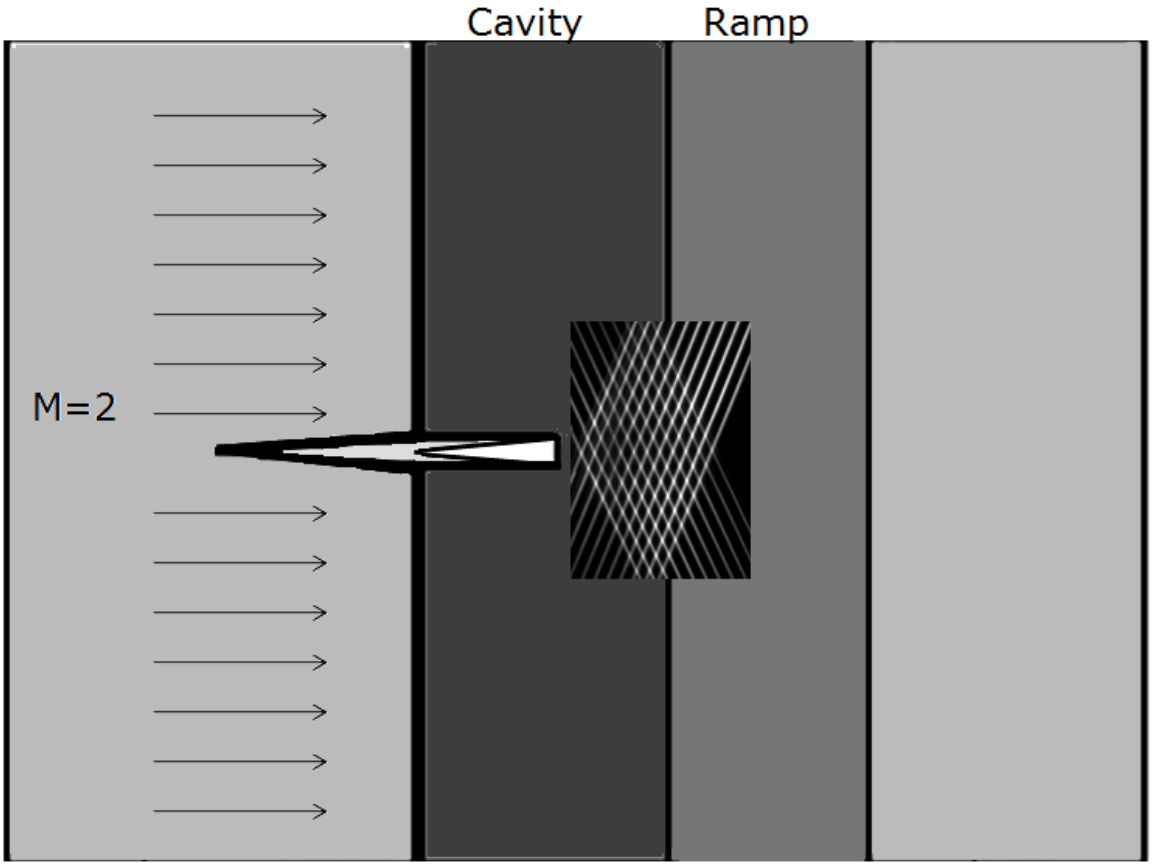


**Figure 4-26: Measurement location for the strut configuration.**

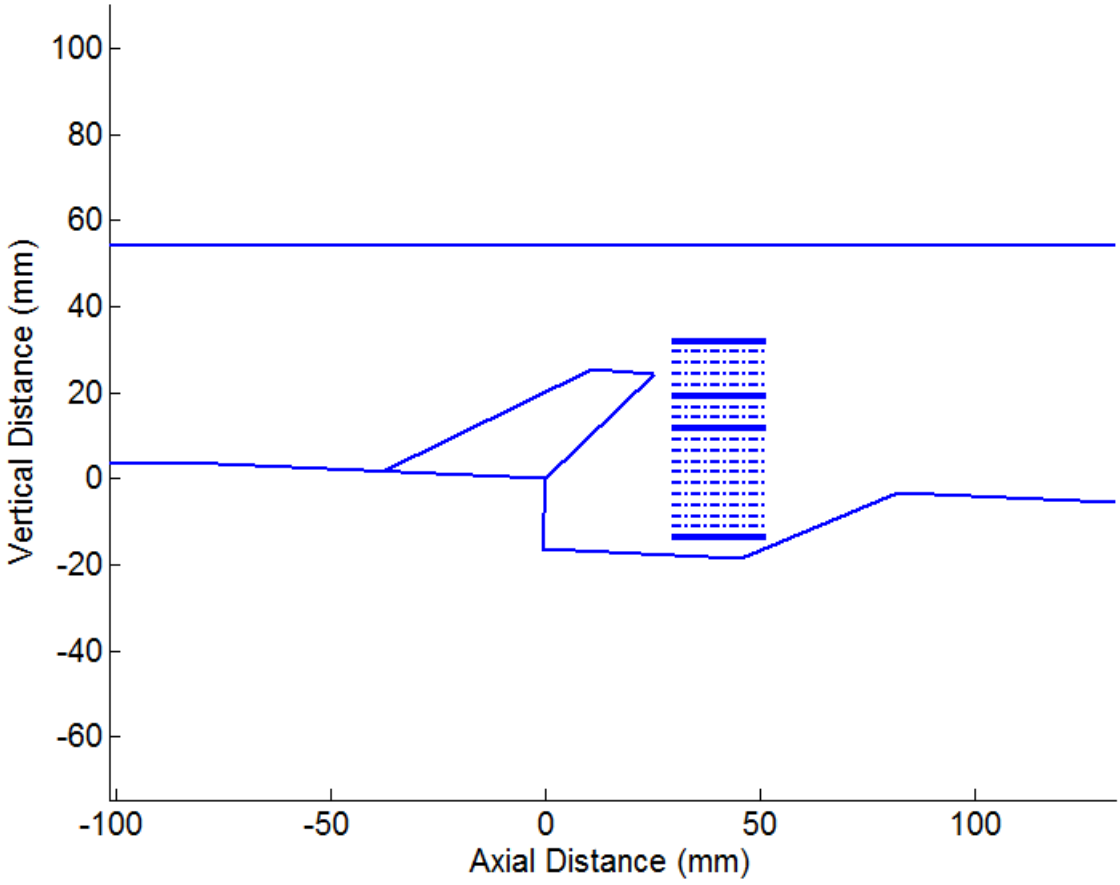


**Figure 4-27: Vertical locations of HTV grids for the strut configuration. The bold, solid lines represent the vertical locations of interest in this paper.**

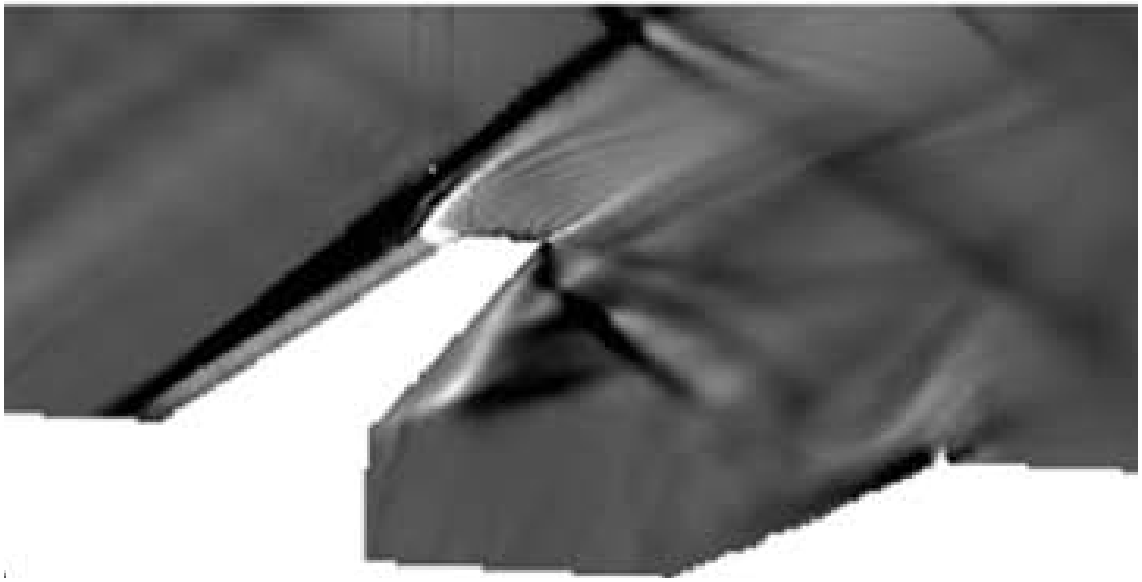

**Figure 4-28: CFD simulated image of ∂ρ/∂x with lighter regions representing reductions in density, and darker regions representing increases in density created by Menon [22].**

noted that this figure only shows the change in density relative to the streamwise, x, direction. The expected changes in the spanwise direction will be shown in a later figure.

Due to the strong out-of-plane velocity component present in the wake region of the strut, three adaptations to the no-strut configuration were implemented. First, the thickness of the 282 nm read sheet was increased to ~260 μm by moving the 1 m fl spherical lens back about ~0.25 m. Second, typical delay times for grids taken in the wake region were reduced to 1 μs. Finally, the stagnation pressure was decreased to increase the relative humidity and signal strength. Example grid patterns for both 282 nm sheet thicknesses are shown in Figure 4-29. Figure 4-29 (a) and (b) are both taken at the lower stagnation pressure with a time delay of 1 μs.

Example Powell-Sabin interpolated 300 shot average velocity profiles are shown for y = 33 mm, y = 12.7 mm, and y = -12.7 mm in Figures 4-30, 4-31 and 4-32 respectively with single shot images at these locations shown in Figures 4-33, 4-34, 4-35. Cubic interpolated RMS Fluctuation profiles are shown in Figures 4-36, 4-37, and 4-38 for the same locations. "Hot spots" as seen before are also present in these images. These locations correspond to the "freestream", wake region, and cavity respectively. Figure 4-30 captures freestream flow at top of the figure, and what appears to be a post-expansion wave region at the bottom of the figure. Since the velocities increase after the gradient in the figure, it is believed by the author that this is an expansion wave from the top of the strut agreeing with the numerical simulations by Freeborn et al. [4] and Menon [22] using the current experimental data for validation. Freestream velocities in the strut and no-strut configurations are very similar with both being ~700 m/s and both having RMS Fluctuations values around 2%.

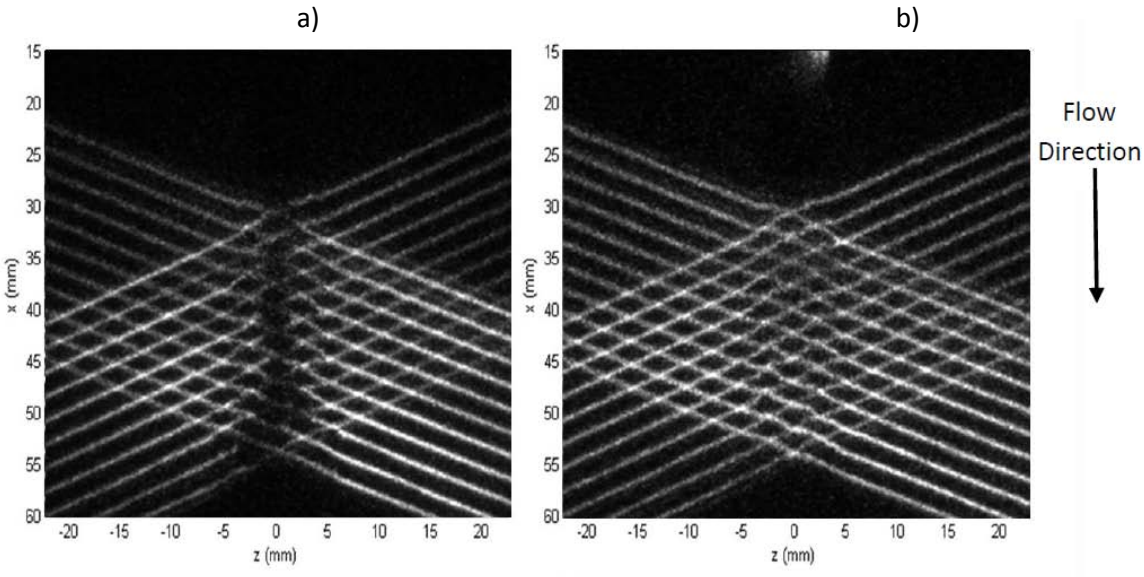


**Figure 4-29: Example grid patterns for the strut configuration with a) original ~150 µm thickness, and b) increased ~260 µm thickness; delay = 1 µs; y = 20 mm.**

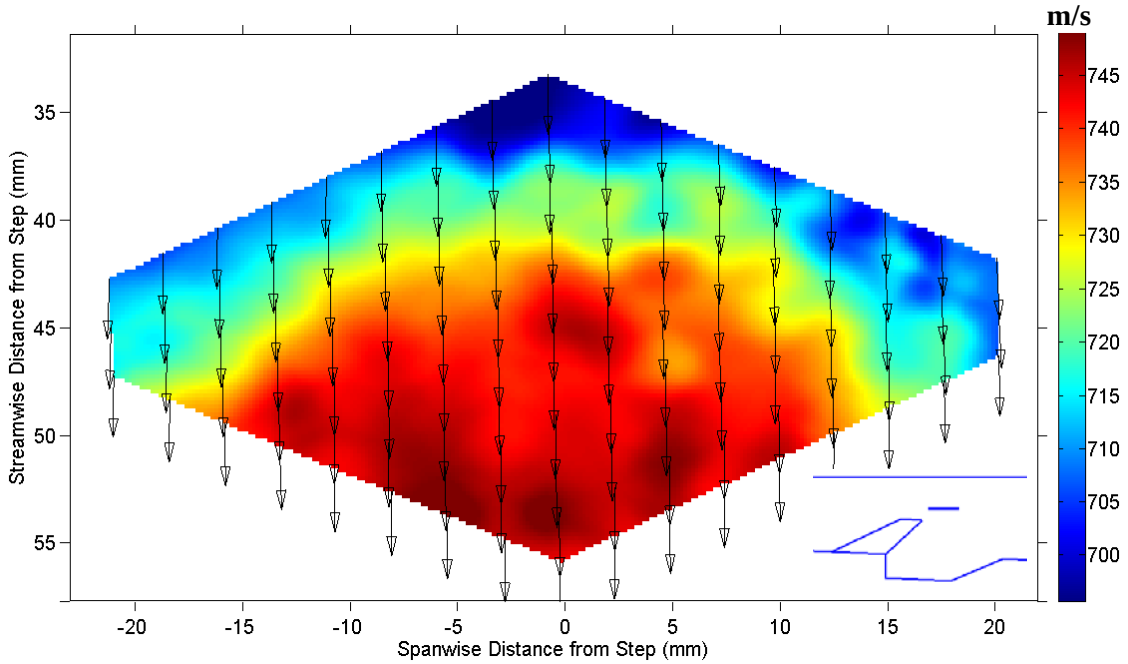


**Figure 4-30: Powell-Sabine interpolated 300 shot average streamwise velocity profile in the freestream at y= 33 mm in the strut configuration. Location shown in insert for clarity.**

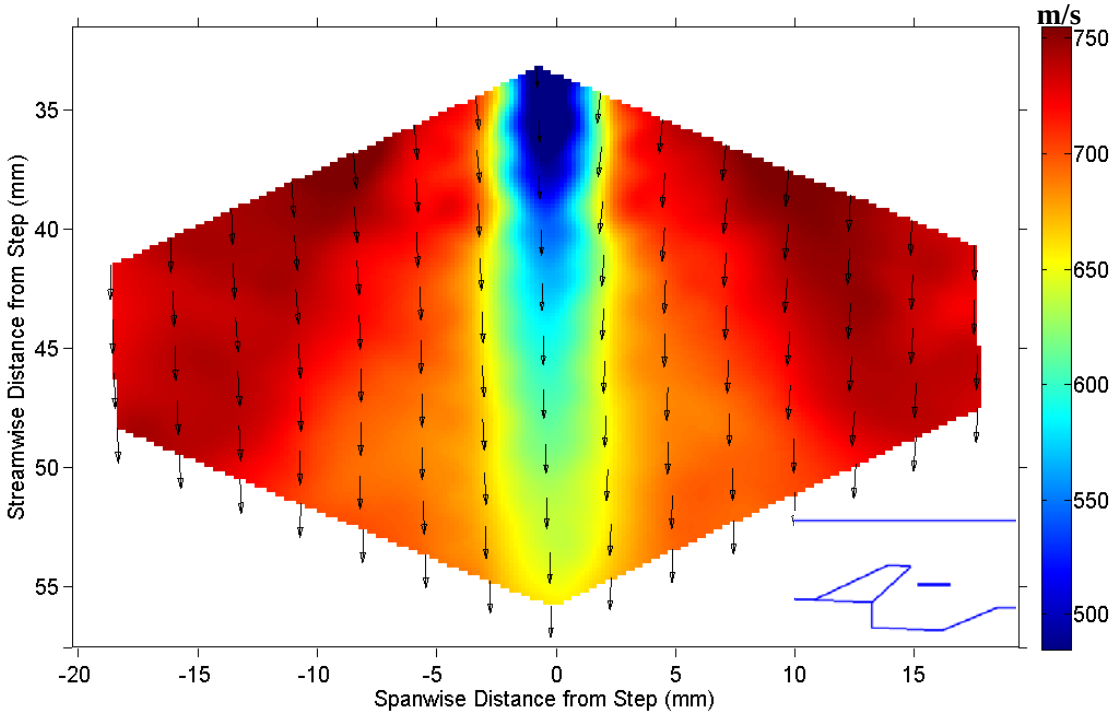


**Figure 4-31: Powell-Sabine interpolated 300 shot average streamwise velocity profile in the wake region at y= 12.7 mm in the strut configuration. Location shown in insert for clarity.**

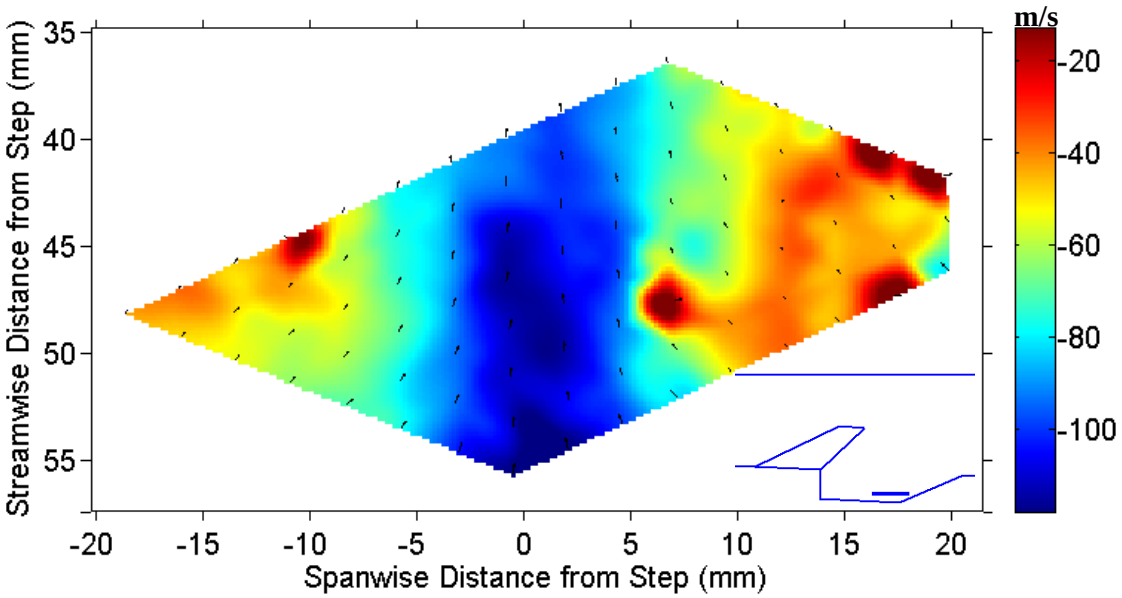


**Figure 4-32: Powell-Sabine interpolated 300 shot average streamwise velocity profile in the cavity at y= -12.7 mm in the strut configuration. Location shown in insert for clarity.**

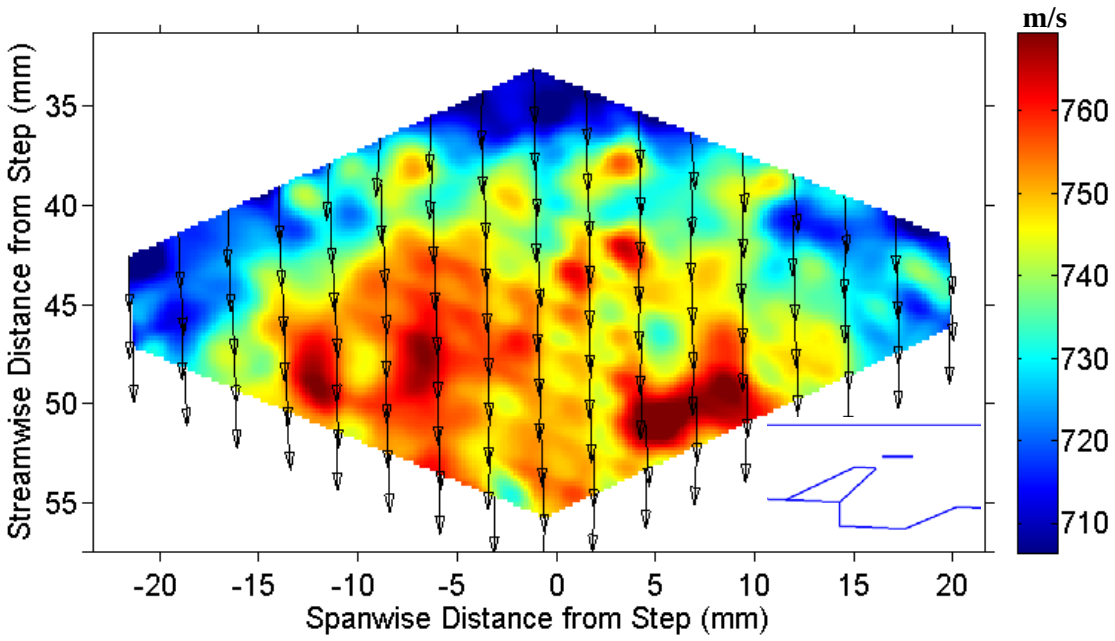


**Figure 4-33: Powell-Sabine interpolated single-shot streamwise velocity profile in the freestream at y = 33 mm in the strut configuration. Location shown in insert for clarity.**

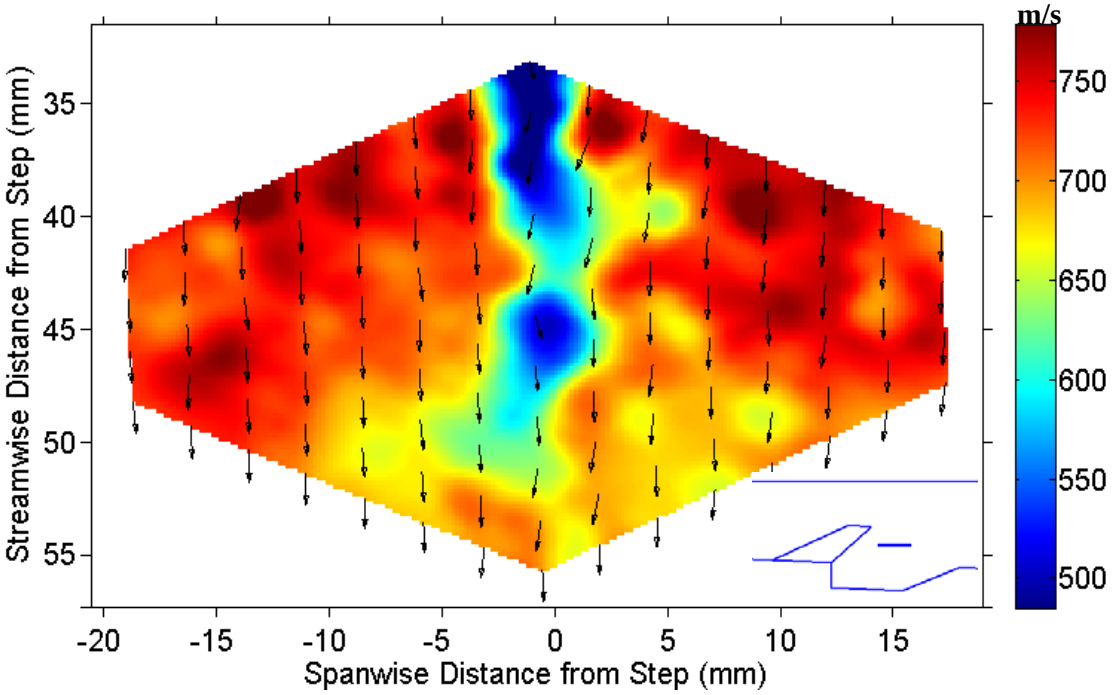


**Figure 4-34: Powell-Sabine interpolated single-shot streamwise velocity profile in the wake region at y = 12.7 mm in the strut configuration. Location shown in insert for clarity.**

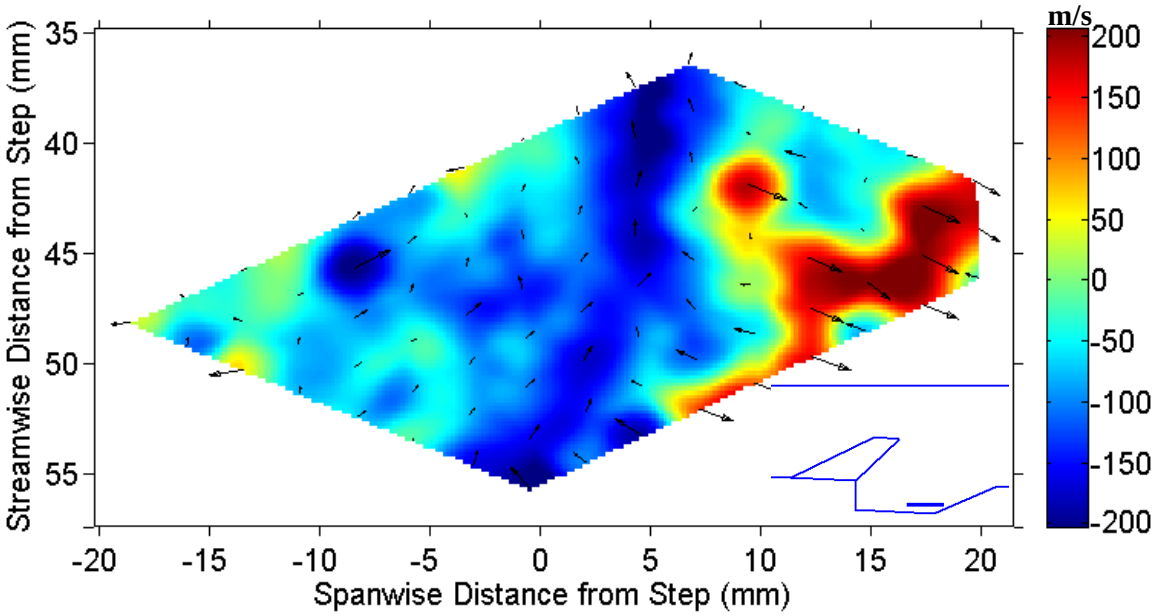


**Figure 4-35: Powell-Sabine interpolated single-shot streamwise velocity profile in the cavity at y = -12.7 mm in the strut configuration. Location shown in insert for clarity.**

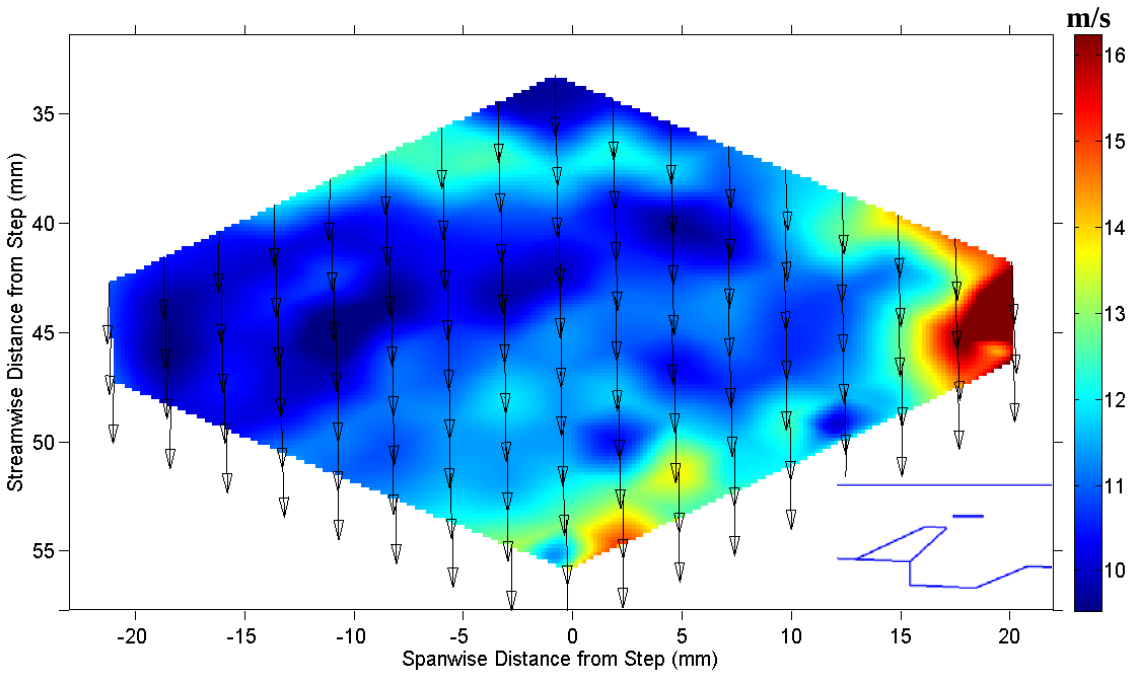


**Figure 4-36: Cubic interpolated streamwise 300 shot RMS fluctuation profile at y= 33 mm in the strut configuration with arrows showing mean velocity magnitude at the grid intersections. Location shown in insert for clarity.**

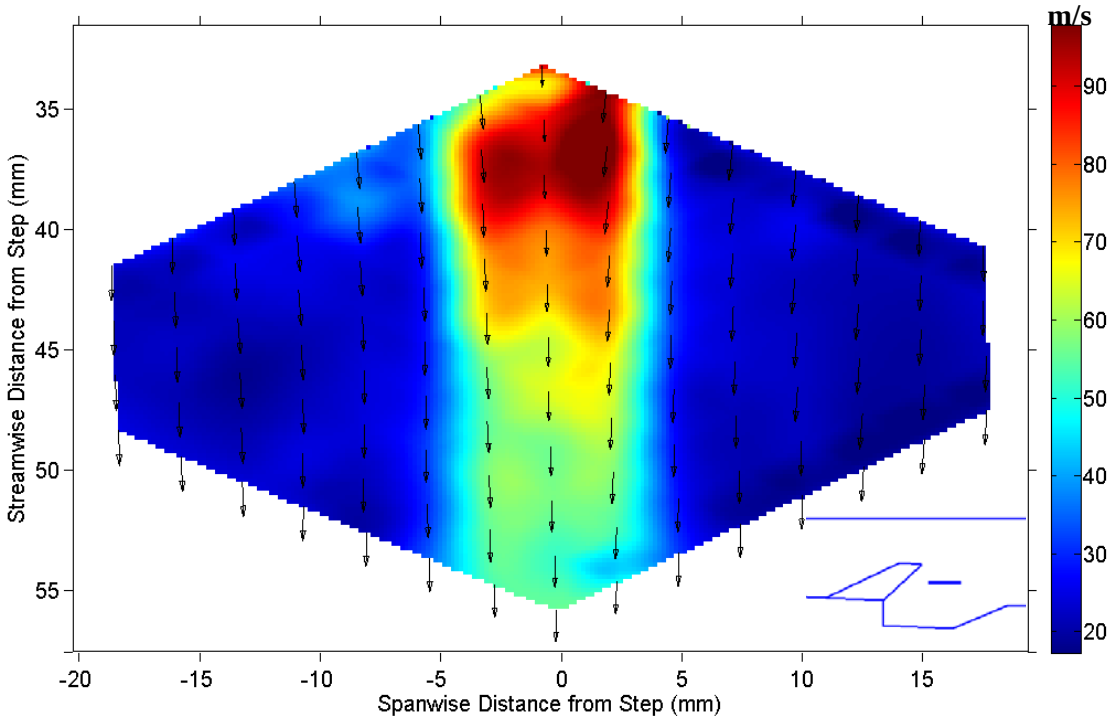


**Figure 4-37: Cubic interpolated streamwise 300 shot RMS fluctuation profile at y= 12.7 mm in the strut configuration with arrows showing mean velocity magnitude at the grid intersections. Location shown in insert for clarity.**

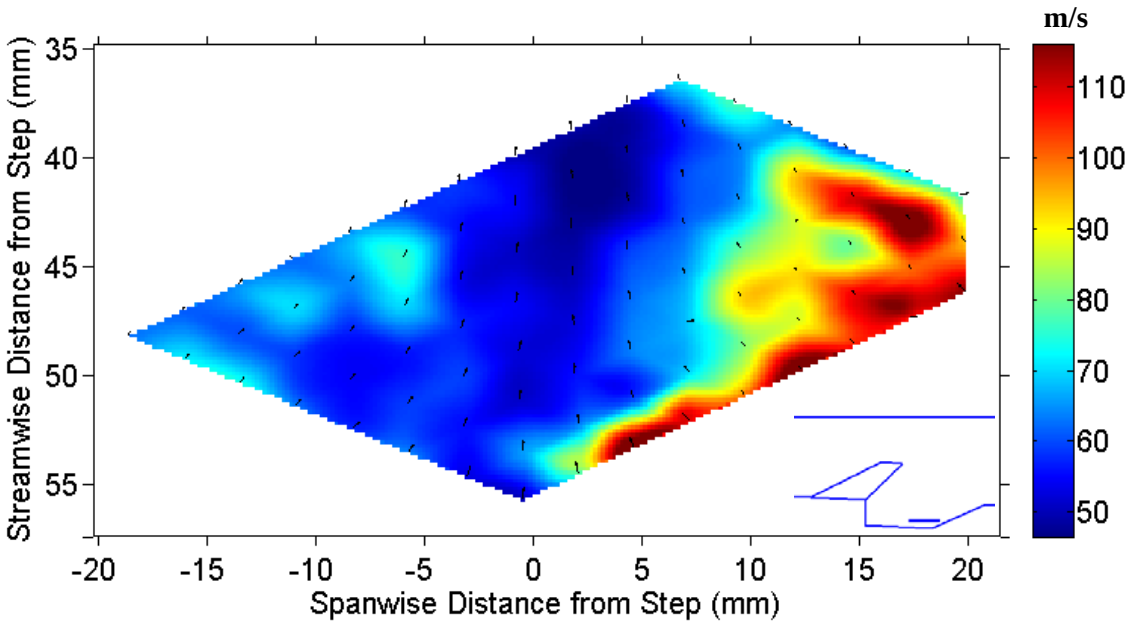


**Figure 4-38: Cubic interpolated streamwise 300 shot RMS fluctuation profile at y= -12.7 mm in the strut configuration with arrows showing mean velocity magnitude at the grid intersections. Location shown in insert for clarity.**

A diagram showing this shock/expansion wave pattern is given in Figure 4-39 (a) with comparison from Freeborn et al. [4] in Figure 4-39 (b) which indicates that both the shock and expansion waves are beyond the field of view of the camera. The two regions visible in Figure 4-31 are the post expansion wave region behind the strut, and the strut wake region. Given the Mach 2 ($\theta_{crit}$= 23°) supersonic flow upstream of the strut, one would expect with a wedge angle of 18.5° that an oblique shock would form, followed by an expansion wave at the 9.25° corner. Due to this symmetry, inviscid gas dynamics equations predict that the flow velocity after this expansion wave would be similar to those found in the freestream ahead of the strut. As can be seen in Figure 4-31, some of the velocities outside of the wake region are in fact quite similar to the freestream values. A decrease in velocity can be seen in Figure 4-31 due to the presence of a weak compression wave originating at the trailing edge of the strut which was also seen by Freeborn et al. [4]. This would indicate that the pressure in the cavity which is being entrained behind the strut is higher than the post-expansion region as expected. Furthermore, the RMS fluctuation values in the post-shock-expansion region are about twice those found in the freestream indicating that the strut has increased turbulence.

Velocity profiles in the cavity for the strut and no-strut case have a few similarities which can be seen in Figures 4-15 and 4-32. Both have predominately negative (i.e. recirculating) velocities with RMS fluctuations higher than the freestream as seen in Figures 4-19 and 4-38. However, the centerline velocities over the ramp differ between these two configurations as can be seen in Figure 4-40. In fact, at y = -7.62 mm a twofold increase in recirculation along the cavity centerline can be seen in the strut configuration. T he recirculation in the strut configuration remains roughly constant at ~100 m/s from

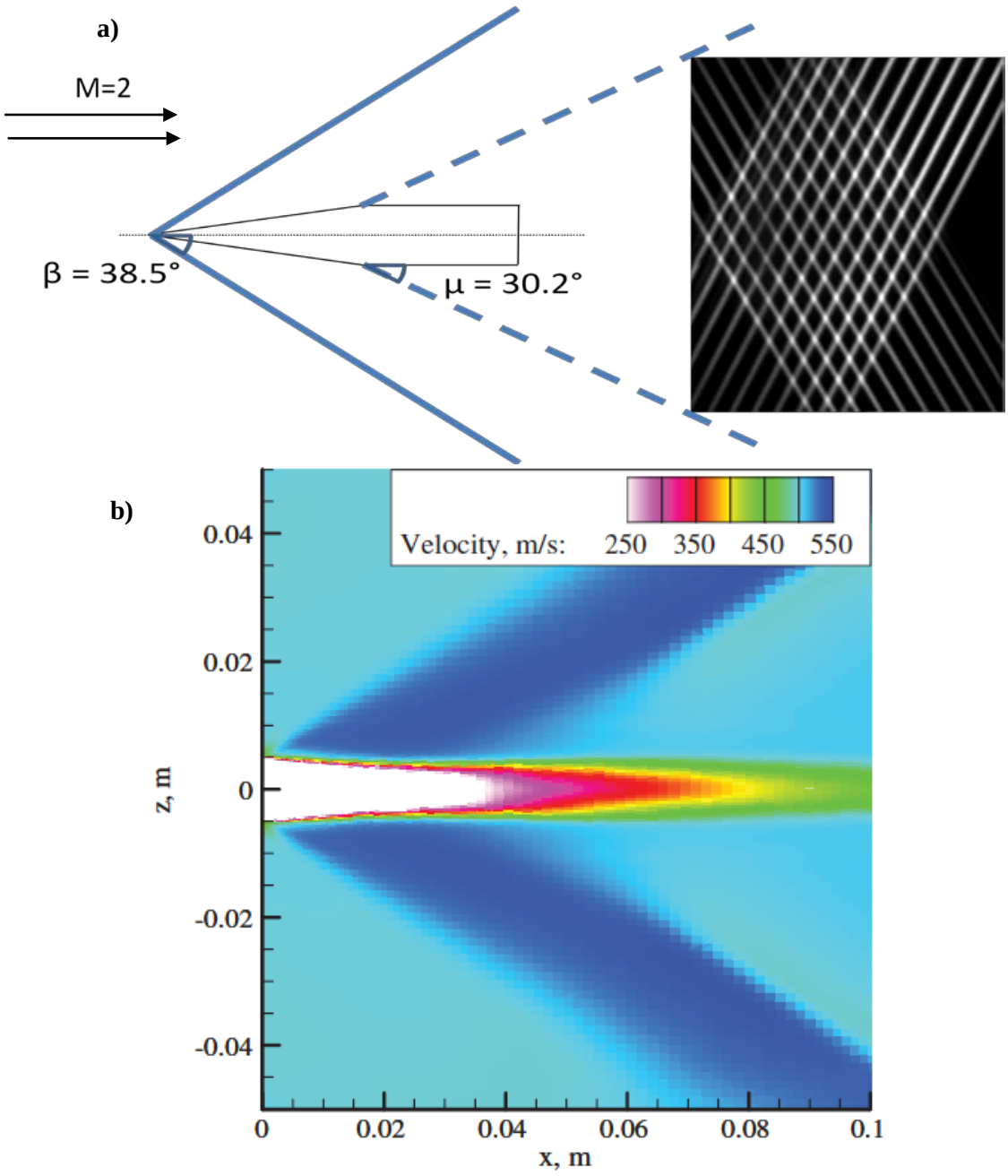


**Figure 4-39: Wave diagram for the wake region of the strut with grid shown for reference at y = 12.7 mm. The solid lines represent an oblique shockwave at the leading edge of the strut with angle β shown in the picture, and the dotted lines represent the rearward Mach line of the expansion wave at the corner with angle noted (a), with comparison to Freeborn et al. [4] (b).**

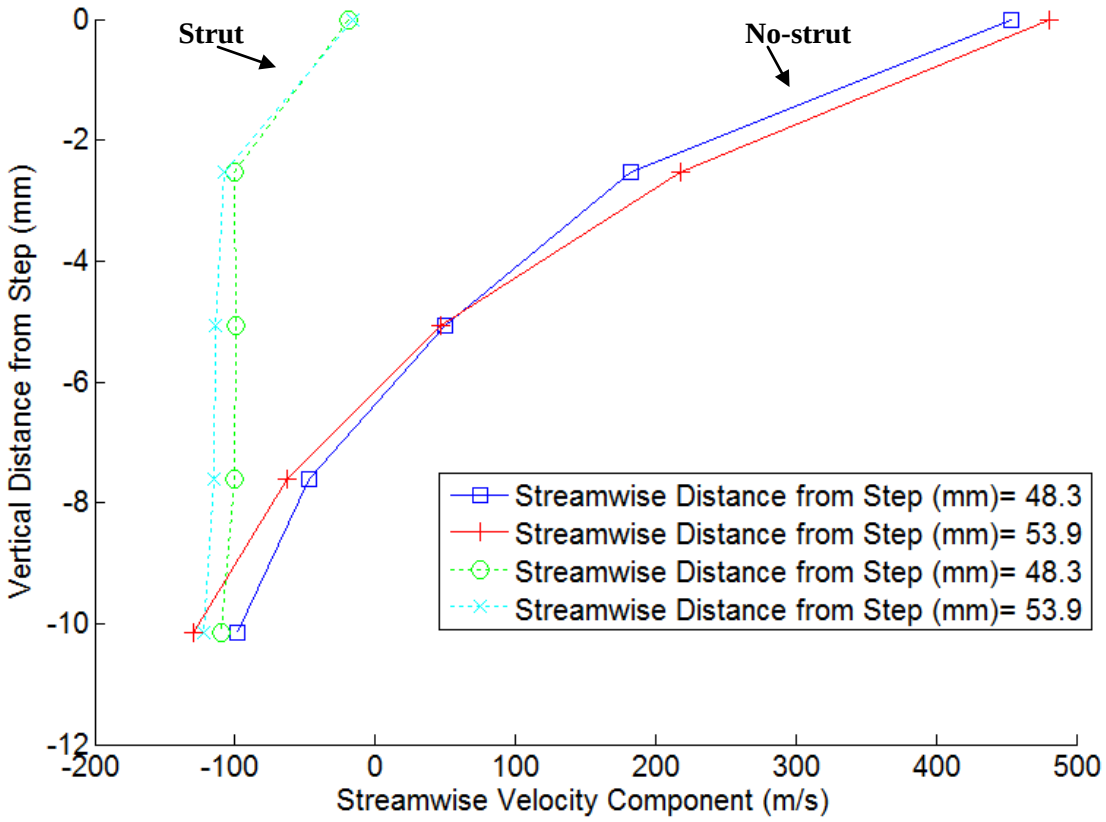


**Figure 4-40: 300 shot mean velocity profile along the centerline in the vertical (y) direction for the no-strut (solid lines) and strut (dotted lines) at various streamwise locations. Ramp is located 46 mm from the step.**

y = -10.2 mm until about y = -2.54 mm, whereas the recirculation region ends at about y = -6.75 mm in the no-strut configuration at these distances from the step. These trends are similar to those predicted by Freeborn et al. in their CFD results [4].

These flow patterns induced by the strut would direct the mass entrained over the ramp through the cavity while being mixed, and then up the strut into main flow of the scramjet test section. Therefore, if fuel was inserted at the rear of the cavity, the increased turbulence present over the ramp would provide mixing, and the flow patterns induced by the strut would carry this mixed fuel-air into the main flow as intended.

As mixing and mass exchange between the main flow and the cavity-strut flow increases, residence time in the cavity-strut flow decreases and would ultimately lead to blow-out [4]. Therefore, it is necessary to ensure that the strut does not over augment this mass exchange. HTV, as shown here, can provide the accurate, quantative velocity profiles needed to make a mass exchange calculation for a given scramjet combustor.

### 4.5 Ramped Cavity with Strut Vorticity Analysis

A side-by-side comparison of a Powell-Sabin interpolation and a cubic interpolation for y = 20.3 mm is shown in Figure 4-41 with a similar side-by-side comparison of single-shot images shown in Figure 4-42. As seen before in the no-strut configuration, these two interpolation methods are very similar in the velocity profiles they produce. However, the Powell-Sabin interpolation shows more detail in the velocity gradients near the strut wake. Furthermore, it was known that the grid was 3 pixels (~0.5 mm) off cavity centerline. This offset was correctly predicted by the Powell-Sabin method but not by the cubic method. It would appear that Figure 4-41 and 4-42 are resolving vortices in the shear layer and wake

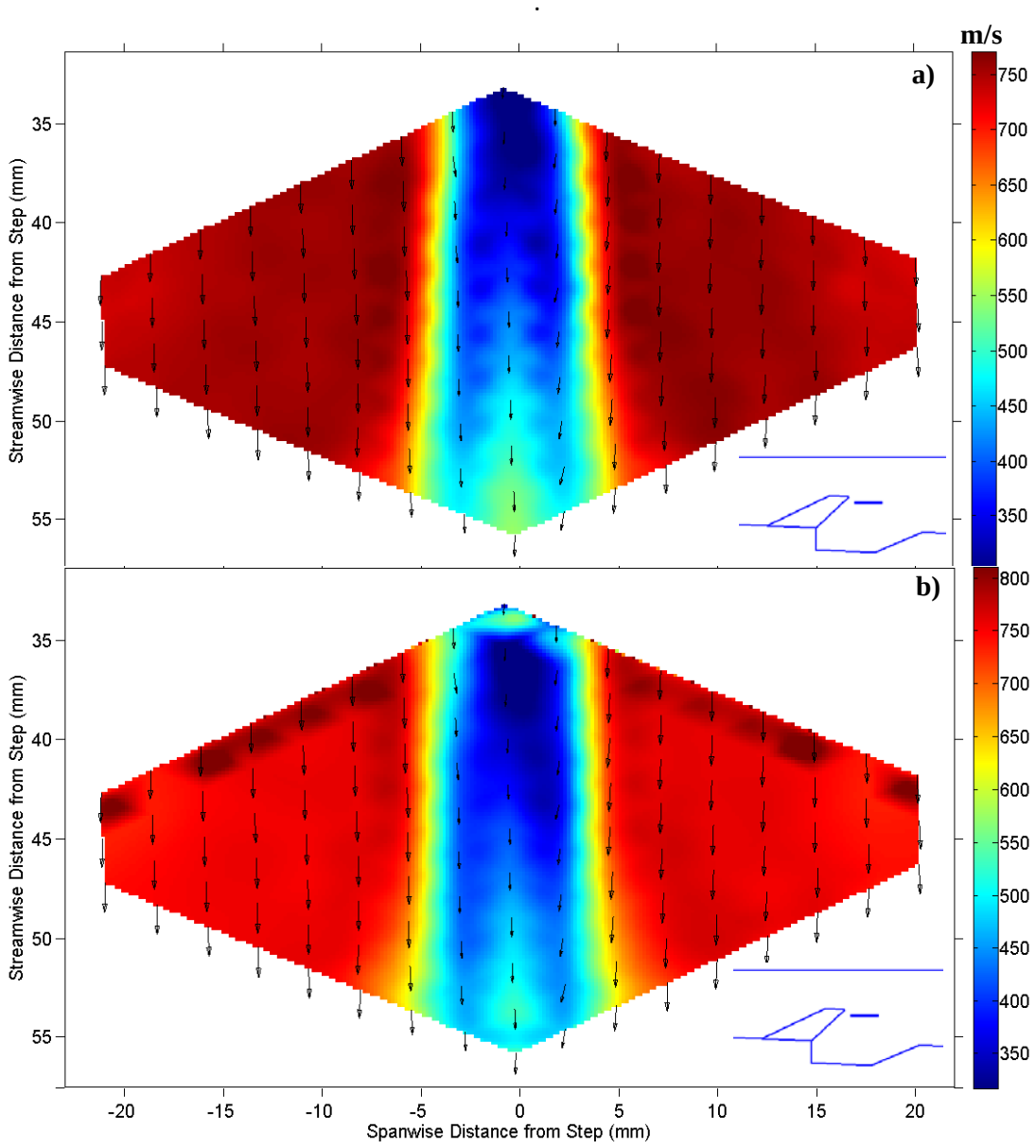


**Figure 4-41: Side-by-side streamwise 300 shot average velocity profile comparison of Powell-Sabin (a) and cubic interpolation (b) in the wake region at y = 20.3 mm. Location shown in inserts for clarity.**

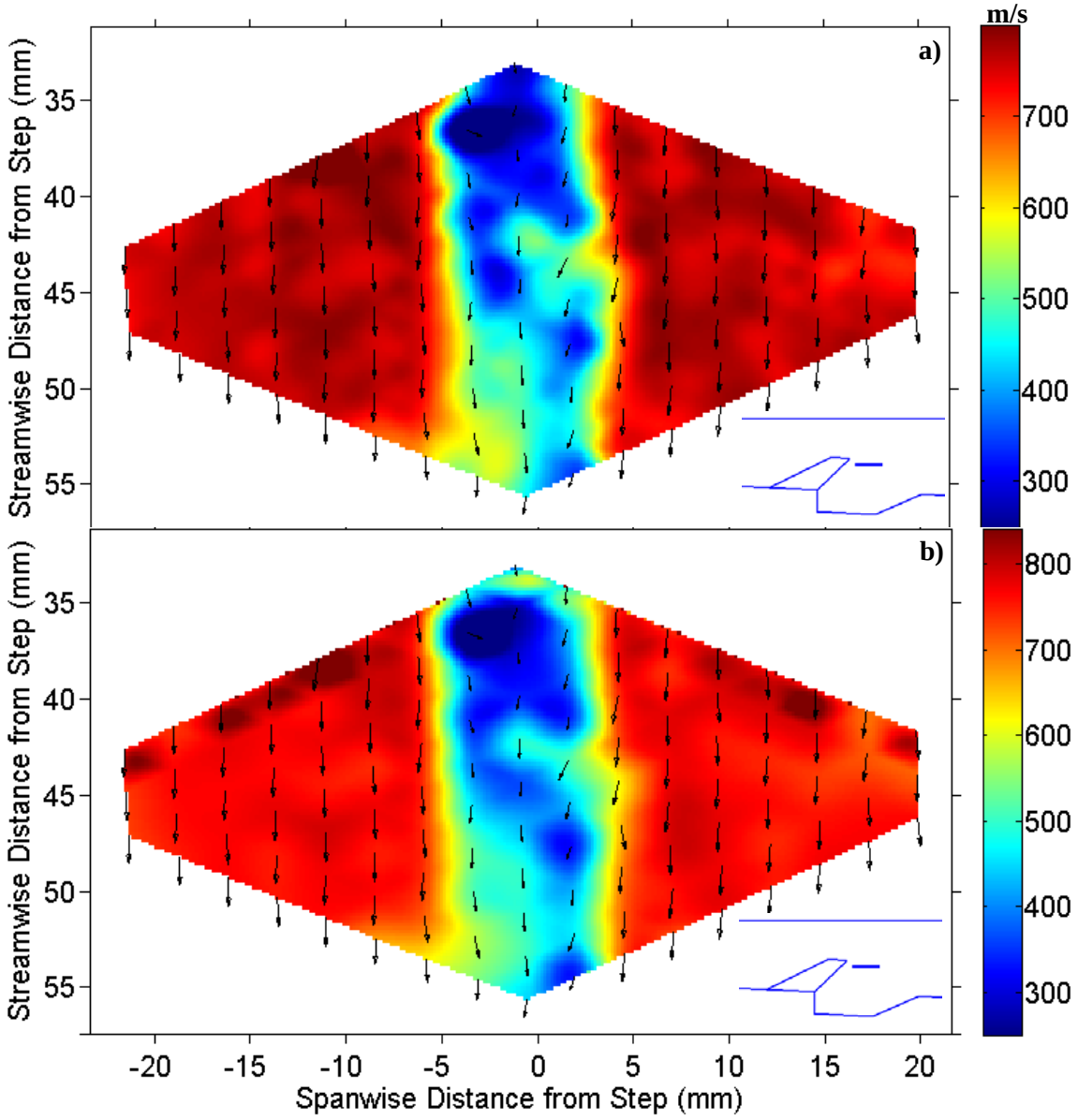


**Figure 4-42: Side-by-side streamwise single-shot velocity profile comparison of Powell-Sabin (a) and cubic interpolation (b) in the wake region at y = 20.3 mm. Location shown in inserts for clarity.**

region behind the strut. However, the wavelength of these vortices is the same as the grid spacing, and is therefore believed to be an artifact. Comparison between the 300 shot average profile of Figure 4-41 and the single shot profile of Figure 4-42 indicates that the location of the wake region boundary is fluctuating with respect to time. For reference, a cubic interpolated RMS fluctuation profile is shown in Figure 4-43 at this location and is similar to the profile seen at y =12.7 mm but with higher fluctuations inside the shear layer.

Figures 4-44 and 4-45 show a side-by-side comparison for y-axis 300 shot average and single shot vorticity at y = 20.3 mm, respectively, where vorticity is defined by Equation 4-4:

$$\omega_y = \partial w/\partial x - \partial u/\partial z \qquad (4\text{-}4)$$

The change in velocity over a pixel's two neighboring pixels is used to determine the partial derivatives for each orthogonal direction in Equation 4-4. In both interpolation methods the thickness of the increased vorticity region and the magnitude thereof decreases downstream of the strut. Once again, the size of these vortices is believed to be an artifact of the grid spacing. In both interpolation methods, an average vorticity equal to ~300 1/s and an instantaneous vorticity reaching ~400 1/s are observed. Figure 4-44 also shows that these vortices gradually decrease in strength as they move downstream. Furthermore, in Figure 4-44 (a) the vortices slowly diverge away from the centerline while in Figure 4-44 (b) the high vorticity regions are more-or-less parallel. In Figure 4-41 (a) and (b) and Figure 4-43, the shear layer can be observed to diverge slightly from the centerline. Since these vortices are in the shear layer, they must move with the shear layer (i.e. diverging slightly from center). In the single-shot images shown in Figure 4-45, the vorticity propagates in a similar fashion as seen in Figure 4-44. In the Powell-Sabin interpolation, the high vorticity region was observed to diverge more from the centerline than in the cubic interpolation. However, both interpolations showed that vorticity decreased downstream of the strut.

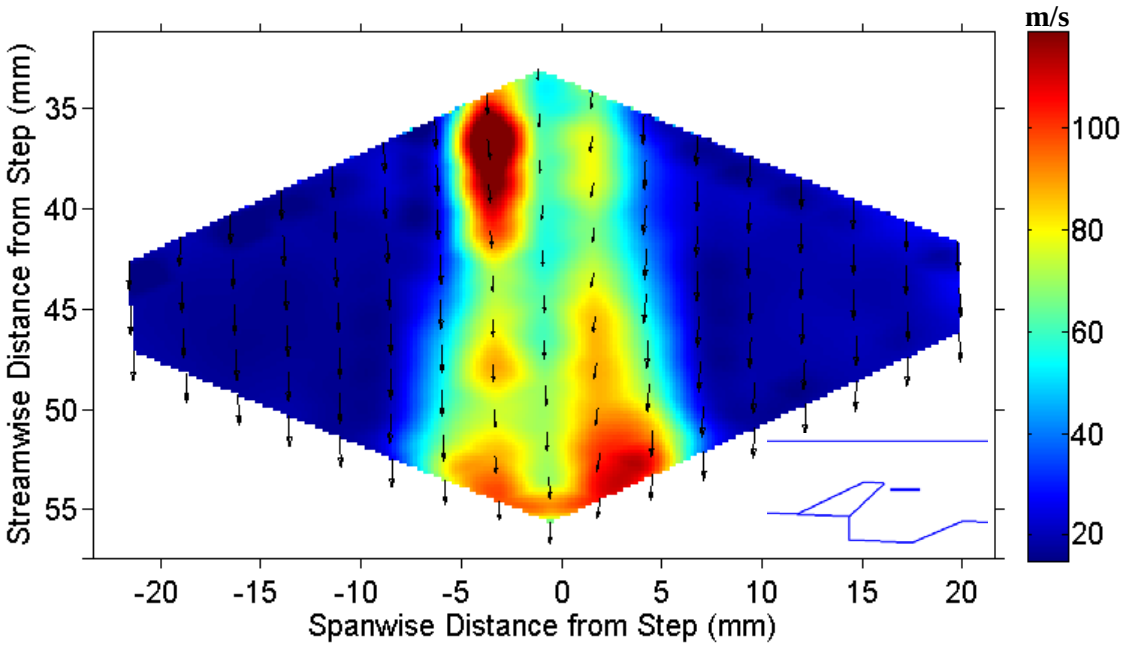


**Figure 4-43: Cubic interpolated streamwise 300 shot RMS fluctuation profile at y= 20.3mm in the strut configuration with arrows showing mean velocity magnitude at the grid intersections. Location shown in insert for clarity.**

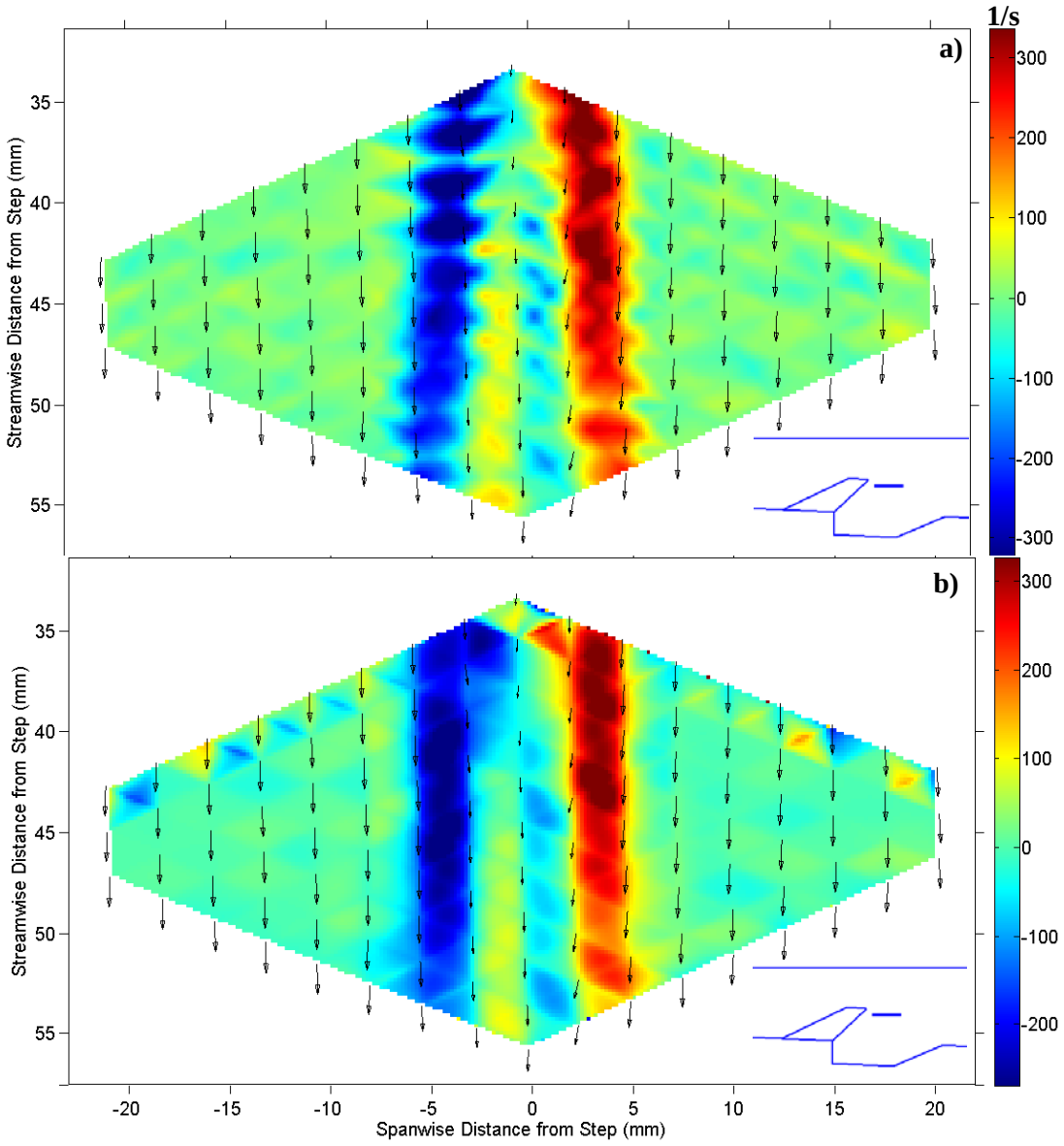


**Figure 4-44: Side-by-side y-component 300 shot average vorticity comparison of Powell-Sabin (a) and cubic interpolation (b) in the wake region at y = 20.3 mm. Location shown in inserts for clarity.**

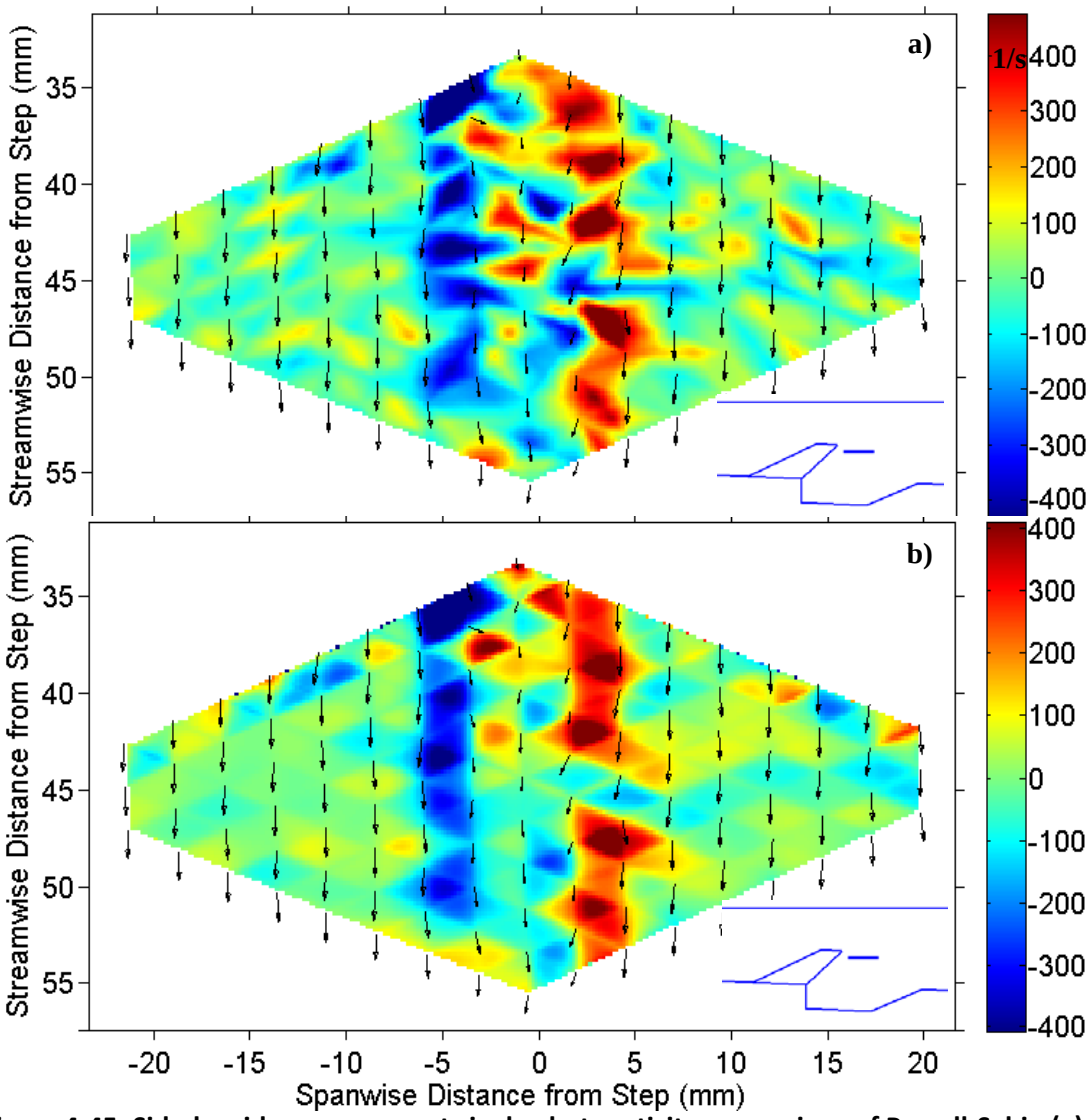


**Figure 4-45: Side-by-side y-component single-shot vorticity comparison of Powell-Sabin (a) and cubic interpolation (b) in the wake region at y = 20.3 mm. Location shown in inserts for clarity.**

It should be noted that in terms of scramjet design, there is nothing of significance about characterizing the shear layer vortices. However, in doing so it has been demonstrated that one can use HTV to determine vorticity and the properties of a given vortex. Therefore, if velocity data were to be collected in a different orthogonal plane in which there were useful vorticity, then the corresponding analysis could have an impact on the design of scramjet combustors by giving insight on potential mixing and mass exchange areas. The streamwise vortices which are shed by the strut [4] are an example of useful vorticity since they augment mass exchange between the cavity-strut flow and the main flow. Furthermore, customized strut geometry has been used [25] to induce streamwise vorticity, and the HTV method can be used to better assay how effectively each strut geometry was at inducing vorticity.

### 4.6 Reacting Data

Previous attempts to obtain velocity profiles in reacting flows were ultimately unsuccessful. The ethylene fuel used for reaction is a strong absorber of the 193 nm write beam [26, 27]. Therefore, an insufficient number of OH tags were created to make HTV measurements. To prevent such fuel absorption, a blended hydrogen-methane mixture was used so that the reactivity of this mixture would be similar to that of ethylene. To determine which concentrations of hydrogen and methane would best suit this purpose, a correlation for the ignition delay of hydrogen-methane fuels developed by Cheng and Oppenheim was used [28] which they validated experimentally in a shock tube. In the current study, a 30% hydrogen 70% methane fuel mixture was used. The ignition-delay correlation described above predicted that this mixture would be about 20% as reactive as ethylene. However, it was expected that this correlation would underestimate the reactivity of this fuel mixture in

a scramjet due to the greater diffusive properties of hydrogen compared to ethylene. No attempt was made to quantify the relative reactivity of this fuel mixture and ethylene, but it appeared that this fuel mixture was at most half as reactive as ethylene.

While this fuel mixture did not absorb the 193 nm write beam, it did produce large quantities of super-equilibrium OH creating a large background OH signal. This background OH signal was greater than the signal produced from the OH tags as seen in Figure 4-46. In an attempt to increase the OH tag signal, an optical system using a single cross and a single line was implemented. However, even with these configurations, the OH tag signal was still on the same scale as the background OH signal as seen in Figure 4-47 (a) and (b) for the no-strut configuration and Figure 4-48 for the strut configuration. Due to the noise from the background OH data reduced in these regions is unreliable, and simply omitting the intersection where there are pockets of super-equilibrium OH would create a bias in the reduced data.

The use of hydrogen diluted with nitrogen to suppress OH production in reacting regions has been proposed. The diluent should reduce the temperature of the reacting region thereby reducing the amount of OH produced. This would partially eliminate the background OH which has proven problematic in the current study. A test study using such a diluted fuel in a diffusion flame is planned for future work.

## 4.7 Out-of-Plane Velocity Component

An attempt was made to estimate the magnitude of the out-of-plane velocity component seen in the strut wake region using the data collected with the original ~150 μm 282 nm sheet (see Figure 4-29 (a)). The general approach to obtaining this estimation was to

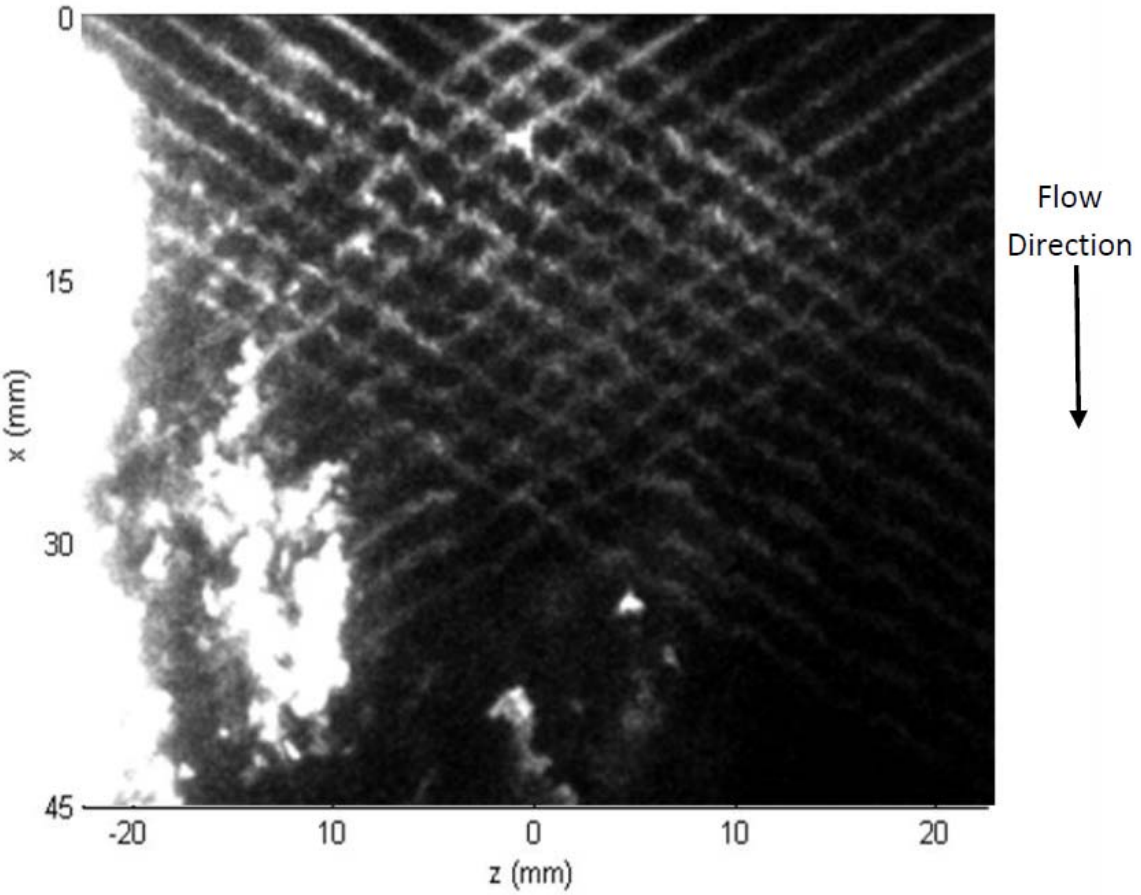


**Figure 4-46: Single-shot HTV image with no strut in a reacting region; delay=2 μs; y = 0 mm; fuel injected at 225 SLPM.**

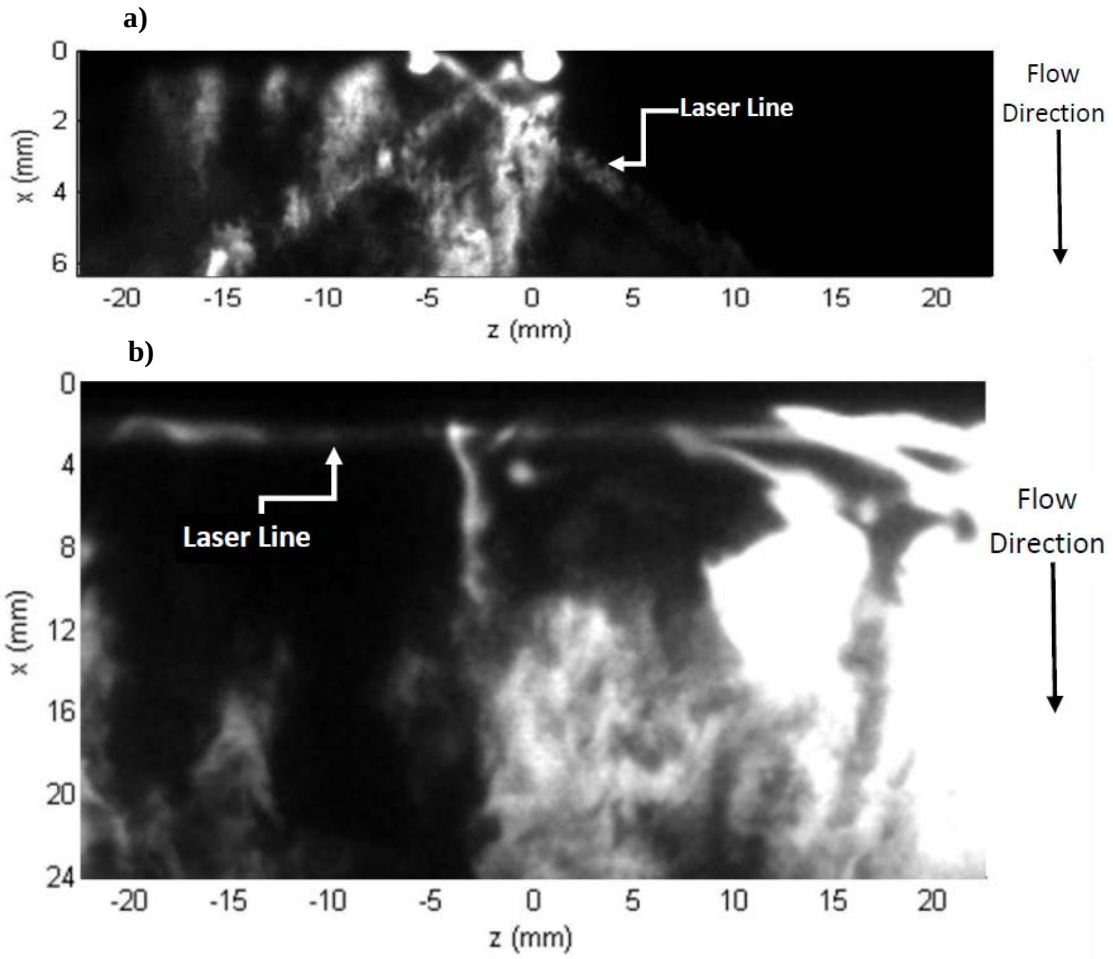


**Figure 4-47: Single-shot HTV images in the reacting region with fuel injected at 225 SLPM. a) single cross made with two 0.3 m fl spherical lenses with no strut in a reacting region; delay=2 µs; y = 0 mm; each 193 nm laser line was ~5 mJ/pulse. b) single-shot HTV image of a single line made with 0.5 m fl spherical lens with no strut in a reacting region; delay=2 µs; y = 0 mm; 193 nm laser line energy was 12 mJ/pulse.**

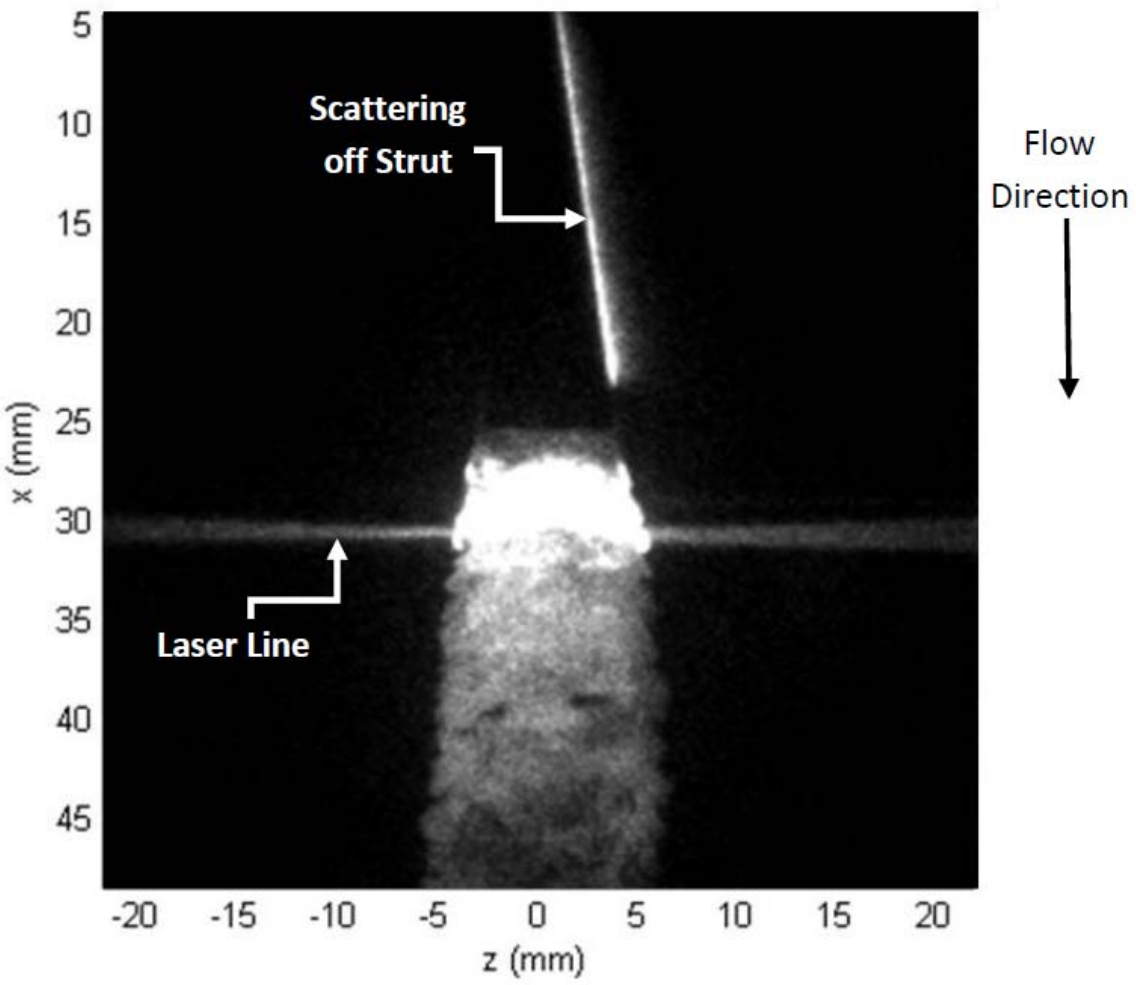


**Figure 4-48: Single-shot HTV image of a single line made with 0.5 m fl spherical lens with a strut in a reacting region; delay=2 µs; y = 25 mm; fuel injected at 270 SLPM; laser line energy was 12 mJ/pulse.**

correlate the signal intensity observed by the camera in an average image at one location to the signal intensity at another location where it was assumed that the out-of-plane velocity component was zero. The reasoning for this approach was that such an out-of-plane velocity would sweep the OH tags created by the 193 nm write beam out of the 282 nm read sheet thereby reducing the LIF signal.

Since the delay times between the read and write phases was 1 μs, diffusion and OH recombination effects were assumed negligible. Another concern for this particular analysis was how well aligned the 193 nm grid and the 282 nm sheet were. In practice, it is difficult to perfectly align the 193 nm write grid and the 282 nm read sheet. Therefore, the alignment of these two aspects was optimized via signal intensity to be the best at the center of the grid. Furthermore, the final 282 nm optic, the 1 m fl spherical lens, was placed so that the sheet would focus on the wind tunnel window 3" away from the center of the tunnel and the grid. This was done so that the thickness of the 193 nm grid and the 282 nm sheet were equivalent as determined by the maximum observed signal intensity. Since the wake region is coincident with the center of the grid where the optical system was optimized, it was assumed that the aforementioned signal correlation technique was reasonable.

The amount of OH tags available for LIF at any particular location is a function of the available water for photodissociation and the energy of each 193 nm grid line. The energy of each grid line can vary due to an uneven excimer beam energy profile, or uneven deposits on the wind tunnel window. Furthermore, no quantitative data was available for the distribution of water molecules in the wake region of the tunnel. Therefore, each averaged delay image was normalized by its corresponding undelayed image to account for these effects. Another problem encountered when applying this technique was the increase in

signal due to a grid intersection. While it might be possible to subtract out the intensity component of the other grid line assuming a Gaussian beam intensity profile, it has not yet been verified if this would introduce any unintended biasing effects. Therefore, data on or near a grid intersection was omitted from consideration.

The governing equations for this technique are given below:

$$w_0 \approx f * div \tag{4-5}$$

$$z_r = \frac{\pi w_0}{\lambda} \tag{4-6}$$

$$w(z) = w_0\sqrt{1 + \left(\frac{z}{z_r}\right)^2} \tag{4-7}$$

$$V_y = \left(1 - \frac{I_i}{\max(I)}\right) * \frac{w(z)*2}{dt} \tag{4-8}$$

The waist of a given focused laser beam, $w_0$, is assumed to be equivalent to the product of the focal length of the lens ,f, and the beam divergence, div, as shown in Equation 4-5. The equation for Rayleigh length, $z_r$, over which beam propagation is roughly Gaussian is given in Equation 4-6 where λ is the wave length of the chosen laser. Equation 4-7 gives the equation for Gaussian beam propagation at an axial location z. This technique calculated the values for Equations 4-5 through 4-7 using the 282 nm read laser with an assumed divergence of 0.3 mrad focused with the 1 m lens. A value of 0.3 mrad was used in this analysis because it yielded a $w(3'')_{282\ nm}$ close to the estimated waist of the 193 nm laser (f=300 mm, divergence ≈ 0.4 mrad for broadband mode).

Equation 4-8 uses the normalized intensities described above, I, at a specific pixel, $I_i$, relative to the maximum pixel intensity along a given grid line. The thickness of the sheet is determined at z=3 with a dt=1 μs. Equation 4-8was implemented strictly in the wake region of the strut, and the vertical velocity was assumed to be zero just inside the shear layer. Preliminary results from this method are given in Figure 4-49. The process for determining

the center for each line has not yet been optimized thus creating the apparent roughness in the vertical velocity profiles seen in Figure 4-49. Despite this, the derived velocities agree well with those predicted with CFD codes for a similar wind tunnel configuration by Freeborn et al. [4].

The effect of all the aforementioned assumptions on the derived results has yet to be determined. Furthermore, the effect of turbulence and directional ambiguity on this method was never modeled. Should the direction of the flow oscillate due to turbulence, this method which uses an averaged image would produce misleading or even errant results. Also, the 282 nm beam does not strictly follow Gaussian beam propagation, so the exact sheet thickness is not known nor is it expected to be completely uniform at a given cross-section either. Therefore, the exact accuracy of the derived velocities has an unknown confidence level.

At the current time, there is no intention to further refine the results presented in Figure 4-49 due to the aforementioned issues, and the results were presented here to illustrate the efforts taken to glean all possible information out of the HTV data.

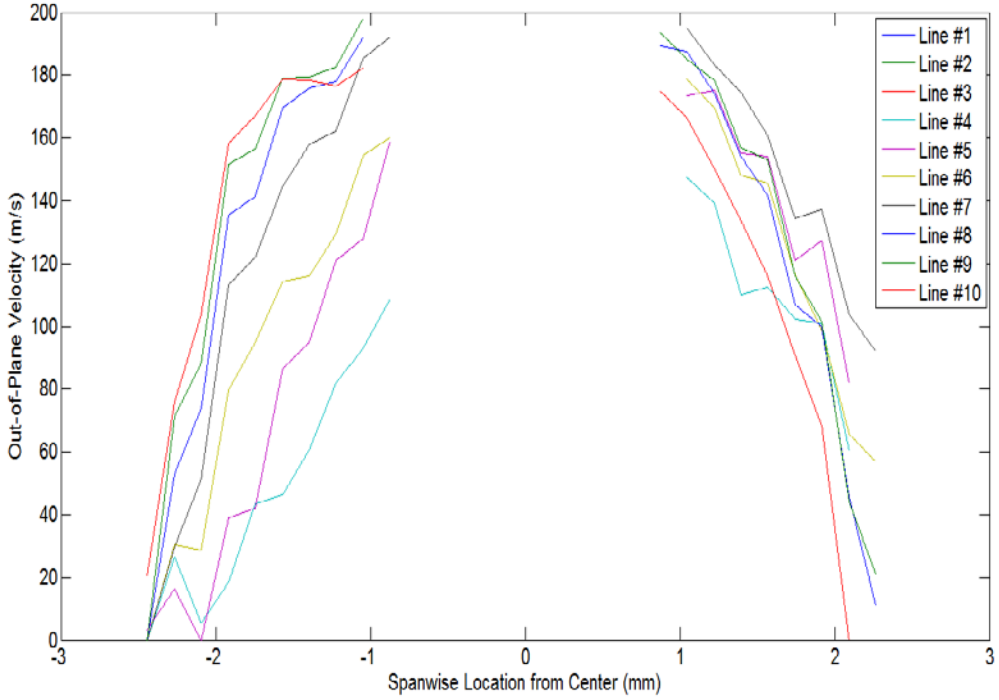


**Figure 4-49: Preliminary results for out-of-plane velocity component at y = 20.3 mm. Line numbers are arranged in ascending order moving downstream.**

# Chapter V

# CONCLUSIONS

## 5.1 Summary

The Mach 2 scramjet test section of Research Cell 19 at Wright Patterson Air Force Base in Dayton, OH was used to obtain non-intrusive velocity measurements in a non-reacting air flow over a ramped cavity flame holder with and without a strut. Instantaneous measurements in the xz plane were taken in the freestream, behind the cavity step, over the cavity ramp, and in the strut wake region to determine velocity mean and RMS Fluctuation profiles. As seen previously, the RMS fluctuation values peaked in the shear layer and were higher in the cavity than in the freestream. Increased turbulence and recirculation values were observed over the ramp of the cavity compared to the step of a rectangular cavity. These increases should aid in fuel-air mixing and ultimately flame stability in a cavity flameholder under reacting conditions (not studied here). It was also observed that the shear layer curled into the cavity and grew slower than the rectangular cavity. Both of these would reduce the flame penetration under reacting conditions demonstrating the need to have some means of increasing the penetration.

An upstream strut proved adequate at increasing the penetration of the cavity flow deep into the main flow of the combustor. Furthermore, in the strut configuration an increase in cavity recirculation along the centerline was observed that extended above the step similar to results shown in the literature. The flow patterns inside the cavity should aid in both flame holding and in fuel penetration into the main flow of a scramjet combustor. These quantitative, non-intrusive measurements of velocity are the first known by the author to have been made in such environments.

Two interpolation schemes were interrogated for their accuracy of interpreting data in rotational flows. It was found that a Powell-Sabin method more accurately predicted the location of the velocity gradients in rotational flows. Additionally, the presence of vorticity in the wake region of the strut was not only detected by analyzed in the current work.

Velocity data in a reacting flow with a 30% hydrogen 70% methane fuel was conducted. It was found that the super-equilibrium OH produced in these flames was on par or greater than the OH created by the HTV method thereby preventing any velocity measurements from being taken. A hydrogen fuel doped with nitrogen is proposed to reduce the flame temperature and OH production to obtain velocity measurements. Furthermore, a means of obtaining an order-of-magnitude approximation of the out-of-plane velocity has been demonstrated.

## 5.1 Conclusions

It has been shown that Hydroxyl Tagging Velocimetry is an effective method for determining and differentiating the cold flow patterns inside various scramjet combustor configurations. Furthermore, HTV can be used to assay the effect any particular component has, and can be a useful tool for the design of a scramjet combustor.

## REFERENCES


[1] Huellmantel, L. W., Ziemer, R. W., and Cambel, A. B., 1957, "Stabilization of premixed propane-air flames in recessed ducts," Jet Propulsion, 27, pp. 31-34, 43.

[2] Ben-Yakar, A., and Hanson, R. K., "Cavity flame-holders for ignition and flame stabilization in scramjets: an overview," Journal of Propulsion and Power, 17(4), pp. 869-877.

[3] Rossiter, J. E., 1964, "Wind-tunnel experiments on the flow over rectangular cavities at subsonic and transonic speeds,"Aeronautical Research Council Reports and Memoranda, pp. 1-32.

[4] Freeborn, A. B., King, P. I., and Gruber, M. R., 2009, "Swept-leading-edge pylon effects on a scramjet pylon-cavity flameholder flowfield," Journal of Propulsion and Power, 25(3), pp. 571-582.

[5] Sato, S., Izumikawa, M., Tomioka, S., and Mitani, T., 1997, "Scramjet engine test at the Mach 6 flight condition," 33rd AIAA Joint Propulsion Conference and Exhibit, Seattle, WA, AIAA 97-3021.

[6] Yu, G., Li, J. G., Zhang, X. Y., Chen, L. H., Han, B., and Sung, C. J., 2002, "Experimental investigation on flameholding mechanism and combustion performance in hydrogen-fueled supersonic combustors," Combustion Science and Technology, 174(3), pp. 1-27.

[7] Gruber, M. R., Carter, C. D., Montes, D. R., Haubelt, L. C., Kings, P. I., and Hsu, K. Y., 2008, "Experimental studies of pylon-aided fuel injection into a supersonic crossflow," Journal of Propulsion and Power, 24(3), pp. 460-470.

[8] Hsu, K.-Y., Carter, C. D., Gruber, M. R., and Barhorst, T., 2007, "Experimental study of cavity-strut combustion in supersonic flow," 43rd AIAA/ASME/SAE/ASEE Joint Propulsion Conference and Exhibit, AIAA, Cincinnati, OH, pp. Paper No. 2007-5394.

[9] Pitz, R. W., Lahr, M. D., Douglas, Z. W., Wehrmeyer, J. A., Hu, S. T., Carter, C. D., Hsu, K. Y., Lum, C., and Koochesfahani, M. M., 2005, "Hydroxyl tagging velocimetry in a supersonic flow over a cavity," Applied Optics, 44(31), pp. 6692-6700.

[10] Lahr, M. D., Pitz, R. W., Douglas, Z. W., and Carter, C. D., 2010, "Hydroxyl-tagging-velocimetry measurements of a supersonic flow over a cavity," Journal of Propulsion and Power, 26(4), pp. 790-797.

[11] Ress, J. M., Laufer, G., and Krauss, R. H., 1995, "Laser ion time-of-flight velocity-measurements using N-2(+) tracers," AIAA Journal, 33(2), pp. 296-301.

[12] Pitz, R. W., Wehrmeyer, J. A., Ribarov, L. A., Oguss, D. A., Batliwala, F., DeBarber, P. A., Deusch, S., and Dimotakis, P. E., 2000, "Unseeded molecular flow tagging in cold and hot flows using ozone and hydroxyl tagging velocimetry," Measurement Science & Technology, 11(9), pp. 1259-1271.

[13] Dam, N., Klein-Douwel, R. J. H., Sijtsema, N. M., and ter Meulen, J. J., 2001, "Nitric oxide flow tagging in unseeded air," Optics Letters, 26(1), pp. 36-38.

[14] Niioka, T., Terada, K., Kobayashi, H., and Hasegawa, S., 1995, "Flame Stabilization characteristics of strut divided into 2 parts in supersonic air-flow," Journal of Propulsion and Power, 11(1), pp. 112-116.

[15] van der Laan, W. P. N., Tolboom, R. A. L., Dam, N. J., and ter Meulen, J. J., 2003, "Molecular tagging velocimetry in the wake of an object in supersonic flow," Experiments in Fluids, 34(4), pp. 531-533.

[16] Noullez, A., Wallace, G., Lempert, W., Miles, R. B., and Frisch, U., 1997, "Transverse velocity increments in turbulent flow using the RELIEF technique," Journal of Fluid Mechanics, 339, pp. 287-307.

[17] Engel, V., Meijer, G., Bath, A., Andresen, P., and Schinke, R., 1987, "The Č-Ã Emission in water - theory and experiment," Journal of Chemical Physics, 87(8), pp. 4310-4314.

[18] Gruber, M. R., and Nejad, A. S., 1995, "New supersonic combustion research facility," Journal of Propulsion and Power, 11(5), pp. 1080-1083.

[19] Gendrich, C. P., and Koochesfahani, M. M., 1996, "A spatial correlation technique for estimating velocity fields using molecular tagging velocimetry (MTV)," Experiments in Fluids, 22(1), pp. 67-77.

[20] Ramsey, M. C., and Pitz, R. W., 2011, "Template matching for improved accuracy in Molecular Tagging Velocimetry,"(Submitted) Experiments in Fluids.

[21] Grady, N. R., Friedlander, T., Pitz, R. W., Carter, C. D., and Hsu, K.-Y., "Hydroxyl tagging velocimetry in a supersonic flow over a piloted cavity," 48th AIAA Aerospace Sciences Meeting, Paper No. AIAA-2010-1405, Orlando, Florida, January 4-7, 2010.

[22] Menon, Suresh. “Personal communication”. 9 August 2010.

[23] Pitz, R. W., and Daily, J. W., 1983, "Combustion in a turbulent mixing layer formed at a rearward-facing step," AIAA Journal, 21(11), pp. 1565-1570.

[24] Hsu, K.-Y., Carter, C. D., Gruber, M. R., and Barhorst, T., 2007, "Experimental study of cavity-strut combustion in supersonic flow," 43rd AIAA/ASME/SAE/ASEE Joint Propulstion Conference and Exhibit, AIAA, Cincinnati, OH, pp. Paper No. AIAA-2007-5394.

[25] Doster, J. C., King, P. I., Gruber, M. R., Carter, C. D., Ryan, M. D., and Hsu, K. Y., 2009, "In-stream hypermixer fueling pylons in supersonic flow," Journal of Propulsion and Power, 25(4), pp. 885-901.

[26] Balko, B. A., Zhang, J., and Lee, Y. T., 1992, "Photodissocation of ethylene at 193 nm," Journal of Chemical Physics, 97(2), pp. 935-942.

[27] Cromwell, E. F., Stolow, A., Vrakking, M. J. J., and Lee, Y. T., 1992, "Dynamics of ethylene photodissociation from rovibrational and translational energy-distribution of H2 products," Journal of Chemical Physics, 97(6), pp. 4029-4040.

[28] Cheng, R. K., and Oppenheim, A. K., 1984, "Autoignition in methane hydrogen mixtures," Combustion and Flame, 58(2), pp. 125-139.